Analysis of Surface Roughness Wake Fields and Longitudinal Phase Space in a Linear Electron Accelerator

Dissertation
zur Erlangung des Doktorgrades
des Fachbereichs Physik
der Universität Hamburg

vorgelegt von

MARKUS HÜNING
aus Borken in Westfalen

Hamburg
2002

Zusammenfassung

Ein Experiment ist in der TESLA Test Anlage (TTF) durchgeführt worden, um Störwellenfelder zu untersuchen, die durch Elektronenpulse mit Picosekunden Länge in engen Strahlrohren mit einer künstlich aufgerauhten Innenoberfläche angeregt werden. In einem magnetischen Spektrometer wurde die durch die Störwellen erzeugte Energiestruktur der Elektronenpakete analysiert. Starke harmonische Energiemodulationen wurden beobachtet. Mit Hilfe einer longitudinalen Phasenraumtomographie wurden die Wakepotentiale direkt vermessen. Dazu war die Implementierung eines neuen Rekonstruktionsalgorithmus basierend auf der Maximum-Entropie-Methode notwendig. Mit einem mm-Wellen Interferometer konnte die zugehörige THz-Strahlung beobachtet werden. Die beobachteten Effekte werden mit Modellrechnungen verglichen.

Abstract

An experiment has been carried out at the TESLA Test Facility (TTF) linac to investigate the wake fields generated by picosecond electron bunches in narrow beam pipes with artificially roughened inner surface. The energy structure imposed on the bunches by the wake fields has been analyzed with a magnetic spectrometer. Strong harmonic wake field effects were observed. By means of longitudinal phase space tomography the wake potentials were studied directly. This required the implementation of a new reconstruction algorithm making use of the maximum entropy method. With a mm-wave interferometer the corresponding THz radiation was observed. The observed effects are compared with model calculations.

To Tina and Jonas

Contents

List of Figures

Chapter 1

Introduction

One of the fundamental principles of modern science is the experiment. By designing sophisticated experimental setups and analyzing the measured data the scientist gains understanding of the principles of nature. The 20th century has experienced an overwhelming progress in terms of extending the measurement techniques to step further and further into fundamental processes.

A very successful tool is the scattering measurement. It is applicable to problems in all fields of physics and many other disciplines. By scattering elementary particles at a target it is possible to uncover hidden properties and reactions of the target material and sometimes the elementary particle itself. Depending on the material under study the projectiles may be electrons, positrons, protons, neutrons, or photons. Owing to the particle-wave duality of quantum theory scattering is basically equivalent to diffraction. The spacial resolution of the scatter experiment is given by the wavelength respectively energy of the projectile. If the energy of the projectile is large enough the nature of interaction with the target may change drastically and new particles be created. In this way the focus of the analysis changes from the initial state of the target to the final state of the reaction, funding a new field of research, the particle physics. Modern elementary particle physics is mainly concerned with the investigation of the basic constituents of matter and their forces and interactions, and the artificially produced second and third generation of leptons and quarks is an essential part of experimental and theoretical particle physics. Almost all experimental data are described with high precision by the standard model of the unified electromagnetic and weak interactions, and the quantum chromodynamics. One essential cornerstone is missing, however, the Higgs particle, which is thought to be responsible for the short range of the weak force and the lepton and quark masses.

To increase the sensitivity and to decrease the statistical errors of the measurements a large particle flux is required. This is especially true in particle physics where interaction cross section usually scales with the inverse square of the center of mass energy. Closely related to the development of scattering techniques is the development of particle accelerators. The development of particle accelerators led to the availability of particle beams of very high particle flux (brightness) and particle energy. The former leads to ever increased sensitivity, whereas the latter leads to improved spatial resolution. In parallel the development also leads to smaller temporal resolution by shortening the beam pulses.

The TESLA (**T**era **E**lectronvolt **S**uperconducting **L**inear **A**ccelerator) collaboration proposes to build a machine that will be at the forefront in two very distinct areas of research. First, it will deliver electron and positron beams for $e^- e^+$ collision experiments at a center of mass energy of 0.5 TeV up to 0.8 TeV at luminosity of 10^{34}cm^{-2}s^{-1}. Secondly, included will be a X-ray free electron laser (FEL) delivering wavelengths around 1 Å with a peak brilliance around 10^{33} photons/(s mrad^2 mm^2 0.1% bandwidth) and pulse length of 100 fs. In this way TESLA will carry on a long-lasting tradition at DESY to use the accelerators built for particle physics for entirely different research fields as well.

At DESY a test accelerator (TESLA Test Facility – TTF) has been built and operated to perform R&D for the superconducting acceleration structures and to do an integrated system test. At the TTF linac also an UV FEL has been operated to prove the viability of the **S**elf **A**mplified **S**pontaneous **E**mission (SASE) mode of free electron lasers. The requirements on the electron beam quality of such a SASE-FEL are very demanding in terms of small transverse and longitudinal emittances. Especially the requirements for the longitudinal phase space with 1 nC of charge concentrated in less than 1 ps and with small energy spread are the subject of intense theoretical and experimental studies. The very short but intense current pulses give rise to strong wake fields and coherent sychrotron radiation effects in the accelerator. These radiation effects in turn influence the energy distribution of the electron bunch.

One main goal of this thesis is the experimental

investigation of the wake fields excited by the residual surface roughness inside the vacuum chamber of the FEL undulator. The gap of this undulator is very small (12 mm) leaving space for a vacuum chamber of 9 mm inner diameter only. Calculations show that the rough surface in the order of 1 μm present in standard 10 mm pipes will lead to strong wake fields by the ultrashort bunches. Together with the resistive wall wake fields this dominates the effects of wake fields on the performance of the FEL. Because of the importance of the effect and some uncertainty in the model predictions an experiment has been conducted at the TTF linac to study the surface roughness wake field effect.

Considering the stochastic nature of the surface structure the model predictions may appear surprising: A resonant excitation at a certain frequency is predicted, with the frequency determined by the radius of the beam pipe and the depth of the surface structures. This harmonic wave could be verified experimentally both from the energy distribution in the bunches as well as by spectral analysis of the emitted radiation. For measuring the energy modulation of the bunches tomographic methods have been applied to reconstruct the longitudinal phase space. The longitudinal phase space tomography in a linear accelerator suffers from the limitation of the angular range which excludes the use of conventional reconstruction algorithms. A maximum entropy method has been utilized to overcome this limitation.

The second chapter of this thesis will give a introduction to wake fields with the focus on different models to describe surface roughness wake fields. In chapter three the fundamentals of FEL physics are described in the one-dimensional theory relevant for the longitudinal phase space. The theory of phase space tomography is explained in chapter four. As an introduction to the discussion of experimental findings the chapter five gives an overview of the TTF linac and the evolution of the longitudinal phase space. The sixth chapter deals with the results of tomographic measurements of the longitudinal phase space done independently of the wake field experiment. The seventh chapter is reserved for a detailed analysis of the data taken in the wake field experiment.

Chapter 2

Wake Fields

A bunch of charged particles moving in an accelerator carries the Coulomb field of its constituents. In the limit of ultrarelativistic motion, i.e. the particle energies are much higher than the rest energies, the field is concentrated in a disk perpendicular to the trajectory of motion. Depending on the structure of the environment the bunch self field is perturbed and can be reflected onto the beam axis and interact with the particles in the bunch itself or with following bunches. The perturbed fields are called wake fields. The radiated energy might impair the proper functioning of the accelerator systems. Wake fields in accelerating structures can be expanded in terms of eigenmodes of the cavities and are then referred to as higher order modes. Depending on whether the wakes act on the bunch itself or on the following bunches they are called short range or long range. The former ones may degrade the longitudinal and transversal emittances of individual bunches, the latter can cause collective instabilities in the accelerator.

The short range wake fields contain wavelengths in the order of the bunch length. In the case of linear colliders (LC) or free electron lasers (FEL) the bunch length is in the range of millimeters and even below. At the same time the bunches contain a large numbers of electrons, e.g. $\sim 10^{10}$ in the TESLA Test Facility linac. Strong peak fields have to be expected.

Devices to analyze the emitted wake field radiation have to use the quasi-optical techniques developed for far infrared radiation.

To create long range wake fields time constants in the order of the bunch spacing are needed. The bunch separation in the TTF linac is 0.4 to 1 μs. Such long fill and decay times may occur in the superconducting cavities. With respect to the long range wake fields for TESLA the major concern are therefore the higher order modes of the acceleration cavities.

In general longitudinal wake fields scale inversely with the distance of the structures from the beam, the transverse wake fields scale with the inverse cube. The synchronous mode wake fields discussed below scale with the inverse square of the radius. Therefore the wakes generated inside the narrow vacuum chambers of the undulator magnets of the FEL are particularly harmful.

2.1 Introduction to wake fields

Consider a point charge q moving in free space at a constant velocity $\boldsymbol{v}$. The electric field in the rest frame of the charged particle is spherically symmetric and drops as $\sim 1/r^2$, with r being the distance from the point charge in cylindrical coordinates (r, φ, z). In an electron accelerator the beams are highly relativistic so that the field has to be Lorentz transformed to the laboratory frame, yielding [21]

$$
\begin{aligned}
\boldsymbol{E}_\parallel(r,t) &= \frac{q}{4\pi\varepsilon_0} \frac{\gamma v t}{[r^2 + (\gamma v t)^2]^{3/2}} \boldsymbol{e}_\parallel, \\
\boldsymbol{E}_\perp(r,t) &= \frac{q}{4\pi\varepsilon_0} \frac{\gamma r}{[r^2 + (\gamma v t)^2]^{3/2}} \boldsymbol{e}_\perp, \quad (2.1) \\
\boldsymbol{B}_\perp(r,t) &= \frac{1}{c^2} \boldsymbol{v} \times \boldsymbol{E}_\perp(r,t), \quad (2.2)
\end{aligned}
$$

where the relativistic factor γ is defined by

$$
\gamma = \frac{1}{\sqrt{1-\beta^2}} \qquad \text{with} \, \beta = \frac{v}{c}. \quad (2.3)
$$

The unit vector $\boldsymbol{e}_\parallel$ is chosen to be parallel to the velocity $\boldsymbol{v}$ of the charge and $\boldsymbol{e}_\perp$ perpendicular to it. Unless specified otherwise, it is assumed in the following that the vacuum chamber is cylinder symmetric and that the beam is moving on its symmetry axis. The peak value of $E_\perp$ is reached at a time $t = 0$ when the particle passes the point of minimum distance to the observer,

$$
\boldsymbol{E}_\perp(r,0) = \frac{q}{4\pi\varepsilon_0} \frac{\gamma}{r^2} \boldsymbol{e}_\perp. \quad (2.4)
$$

The time interval in which the amplitude of the transverse electric field at the radius b exceeds half the peak value is approximately given by

$$
\triangle t \approx \sqrt{2} \frac{b}{\gamma v}. \quad (2.5)
$$

For $\gamma \gg 1$ the electric field is concentrated in a small disk with opening angle $\sim 1/\gamma$. In the ultra-relativistic limit $\gamma \to \infty$ the field reduces to a δ-distribution in the z-direction

$$E_r(r, z, t) = \frac{qZ_0 c}{2\pi r} \delta(z - ct) \qquad B_\varphi = \frac{1}{c} E_r, \quad (2.6)$$

with $\boldsymbol{E}_\perp = E_r \boldsymbol{e}_r$, $\boldsymbol{B}_\perp = B_\varphi \boldsymbol{e}_\varphi$, and $Z_0 = \sqrt{\mu_0/\varepsilon_0}$ the impedance of the vacuum. Because of its appearance the electromagnetic field eq. 2.6 is sometimes referred to as "pan-cake" term.

Here I consider only wake fields with azimuthal symmetry. Then the Helmholtz equations for the electric field in vacuum and non conducting materials can be written as

$$\frac{\mu\varepsilon}{c^2} \partial_t^2 E_z = \frac{1}{r} \partial_r(r\partial_r E_z) + \partial_z^2 E_z \qquad (2.7)$$

$$\frac{\mu\varepsilon}{c^2} \partial_t^2 E_r = \partial_r\left(\frac{1}{r}\partial_r(rE_r)\right) + \partial_z^2 E_r, \quad (2.8)$$

with $\partial_x = \frac{\partial}{\partial x}$ and μ, ε the permeability and the permittivity respectively of the material. For most beam pipe materials it is justified to assume $\mu = 1$, hence this factor will be omitted. The permittivity has to be accounted for in a beam pipe covered with a thin dielectric layer.

Often it is advantageous to use the Fourier transform of the fields

$$E_{z/r}(r, z, t) \qquad (2.9)$$
$$= \frac{1}{2\pi} \int\limits_{-\infty}^{\infty} \int\limits_{-\infty}^{\infty} \tilde{E}_{z/r}(r, k_z, \omega) e^{i(k_z z - \omega t)} d\omega dk_z.$$

Then the wave equation simplifies to

$$\frac{1}{r}\partial_r(r\partial_r \tilde{E}_z) + \left(k^2\varepsilon - k_z^2\right)\tilde{E}_z = 0 \quad (2.10)$$

$$\partial_r\left(\frac{1}{r}\partial_r(r\tilde{E}_r)\right) + \left(k^2\varepsilon - k_z^2\right)\tilde{E}_r = 0,$$

with $k = \omega/c$. The pan-cake term transforms into

$$\tilde{E}_r^\delta = \frac{qZ_0 c}{2\pi r}. \qquad (2.11)$$

When there is no charge the electric field fulfills the Maxwell equation

$$\nabla \cdot \boldsymbol{E} = \frac{1}{r}\partial_r(r\tilde{E}_r) + ik_z\tilde{E}_z = 0. \quad (2.12)$$

This equation relates E_z and E_r. The magnetic field can be derived from

$$-\mu_0 \frac{\partial \boldsymbol{H}}{\partial t} = \mathrm{rot}\,\boldsymbol{E}$$
$$ikZ_0 H_\varphi = ik_z\tilde{E}_r - \partial_r\tilde{E}_z. \qquad (2.13)$$

For the analysis of the influence of the wake fields on the beam the wake potential is calculated. It represents the effective voltage seen by a particle moving within the bunch. The coordinate ζ is the relative longitudinal coordinate moving with the bunch

$$W_\|(\zeta) = \frac{1}{q} \int dz E_z(\zeta, z), \quad \zeta = z - ct, \quad (2.14)$$

The wake potential can be calculated in three steps. First the impedance of the accelerator is calculated from the electric field in the Fourier space. In the ultra relativistic limit it is

$$Z_\|(k) = \frac{1}{qc} \int dz \tilde{E}_z(r = 0, k_z, k) e^{i(k_z - k)z}. \quad (2.15)$$

From the impedance it is possible to calculate the wake function. It is the Green's function, i.e. the wake potential induced by a δ-like charge distribution.

$$W_\|^\delta(\zeta) = \frac{c}{2\pi} \int\limits_{-\infty}^{\infty} dk Z_\|(k) e^{ik\zeta} \qquad (2.16)$$

The wake potential then is the convolution of the wake function with the line charge density $\rho(\xi)$ of the bunch

$$W_\|(\zeta) = \int\limits_{-\infty}^{\infty} d\xi W_\|^\delta(\zeta - \xi)\rho(\xi). \quad (2.17)$$

Certain wake fields are generated continuously along the beam pipe. The wake arising from a dielectric layer discussed in the next section is an example. For quasi infinite beam pipes and continuous wake generation the impedance is usually quoted per unit length and only calculated for the fields synchronous with the bunch

$$Z_\|(k) = \frac{E_z}{qc}. \qquad (2.18)$$

In this case it may be advantageous to use the surface impedance to derive the longitudinal field

$$\mathcal{Z} = \frac{E_z}{H_\varphi}. \qquad (2.19)$$

The contribution of a finite piece of the beam pipe to the total impedance can be calculated via

$$Z_\|(k, L) = \frac{1}{qc} \int\limits_0^L dz \tilde{E}_z(r = 0, k_z, k) e^{i(k_z - k)z}, (2.20)$$

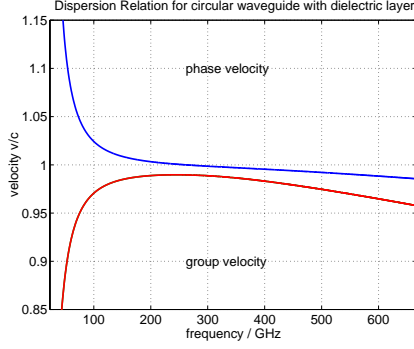with L the length of the considered piece of beam pipe.

4

Figure 2.1: Phase velocity of a waveguide mode in a beam pipe with a dielectric surface layer. The phase velocity ω/k_z and the group velocity $d\omega/dk_z$ are shown. The pipe has a radius of 5 mm and the layer has a thickness of 30 μm.

2.2 Waveguide coated with a dielectric layer

A metallic beam pipe acts as a waveguide. The electromagnetic fields inside this waveguide can be expanded into modes, each individually fulfilling the wave equation 2.10 with appropriate boundary conditions at the metallic walls. The solutions for this equation can be written using Bessel functions of the first kind [8]

$$\tilde{E}_z = \hat{E} \mathrm{J}_0(k_r r), \qquad (2.21)$$

$$\tilde{E}_r = -\frac{ik_z}{k_r} \hat{E} \mathrm{J}_1(k_r r), \qquad (2.22)$$

$$\tilde{H}_\varphi = \frac{k}{k_z Z_0} \tilde{E}_r, \qquad (2.23)$$

with $k_r = \sqrt{k^2 - k_z^2}$. Note that this solution is even valid for $k_r^2 < 0$. The metallic boundary is assumed to be perfectly conducting. Hence the longitudinal electric field vanishes at the surface. This can only be accomplished if $k_r \cdot b$ equals a root of J_0, b being the pipe radius. This yields $k_r^2 > 0$ and hence $k_z < k$. The phase velocity $v_{ph} = c \cdot k/k_z$ is larger than the speed of light for all modes in a perfectly conducting waveguide. The particles are always moving with a speed $v < c$. Even in the ultra-relativistic limit assuming $v = c$ the velocity of any frequency component of the pan-cake term is smaller than the phase velocity of the corresponding waveguide mode. Thus a coupling to the mode is not possible in the time average.

In a waveguide with dielectric coating the situation is fundamentally different. Assume a beam pipe with a thin dielectric layer on its inner surface, with a dielectric constant ε and a thickness $\delta \ll b$. Because the thickness of the dielectric layer is much smaller than the radius of the beam pipe, the variation of r inside the layer is negligible and

equation 2.10 simplifies to

$$\left(\partial_y^2 + \partial_z^2 + \varepsilon k^2\right) \tilde{E}_{z/r} = 0, \qquad (2.24)$$
$$y \equiv b + \delta - r.$$

This approximation is equivalent to assuming the pipe surface being locally flat. The new variable y has the origin at the metallic wall and is pointing inwards. Inside the dielectric layer the solution is found to be

$$\tilde{E}_z^{die} = \hat{E}^{die} \sin(\kappa_r y), \qquad (2.25)$$

$$\tilde{E}_r^{die} = -\frac{ik_z}{\kappa_r} \hat{E}^{die} \cos(\kappa_r y), \qquad (2.26)$$

with $\kappa_r = \sqrt{k^2 \varepsilon - k_z^2}$. The fields have to match at the boundary between the dielectric and the vacuum

$$\tilde{E}_r(b) = \varepsilon \tilde{E}_r^{die}(\delta) \qquad \tilde{E}_z(b) = \tilde{E}_z^{die}(\delta). \quad (2.27)$$

Inserting 2.23 and 2.25 into 2.27 and dividing the two equations yields the surface impedance

$$\mathcal{Z}(k, k_z) = \frac{\tilde{E}_z}{\tilde{H}_\varphi} \qquad (2.28)$$

$$= Z_0 \frac{k_z \tilde{E}_z}{k \tilde{E}_r} = iZ_0 \frac{\kappa_r}{\varepsilon k} \tan(\kappa_r \delta).$$

Without a source current inside the pipe the surface impedance has to match the ratio $\tilde{E}_z/\tilde{H}_\phi$ calculated from (2.21) and (2.23)

$$\frac{\mathcal{Z}}{Z_0} = i \frac{k_r \mathrm{J}_0(k_r b)}{k \mathrm{J}_1(k_r b)}. \qquad (2.29)$$

From this equation it is possible to derive the dispersion relation for the dielectrically coated waveguide.

Trying to calculate $k_z = k_z(k)$ one finds that (2.29) is a transcendental equation. The dispersion can be calculated in closed form when k_r is taken as the independent variable. Additionally one has to assume $\tan \kappa_r \delta \approx \kappa_r \delta$ which is justified due to the small layer thickness, $\kappa_r \delta \ll 1$. Then the equations 2.28 and 2.29 read

$$\frac{\kappa_r^2 \delta}{\varepsilon k} = \frac{k_r \mathrm{J}_0(k_r b)}{k \mathrm{J}_1(k_r b)} \qquad (2.30)$$

$$= \frac{2\mathrm{J}_0(k_r b)}{bk(\mathrm{J}_0(k_r b) + \mathrm{J}_2(k_r b))}.$$

Here the identity $\mathrm{J}_1(x)/x = 1/2 \left(\mathrm{J}_0(x) + \mathrm{J}_2(x)\right)$ is used to continue the function steadily around $k_r^2 = 0$. The factor k on both sides cancels and $\kappa_r^2 = k^2(\varepsilon - 1) + k_r^2$. Then the mode frequency ω_m is given as follows

$$\frac{\omega_m}{c} = k_m(k_r) \qquad (2.31)$$

$$= \sqrt{\frac{2\varepsilon}{(\varepsilon - 1)b\delta} \left(\frac{\mathrm{J}_0(k_r b)}{\mathrm{J}_2(k_r b) + \mathrm{J}_0(k_r b)} - \frac{b\delta}{2\varepsilon} k_r^2\right)},$$

5

$$k_z(k_m, k_r) = \sqrt{k_m^2 - k_r^2}.$$
$$v_{ph} = \frac{k_m}{k_z},$$

An example for the phase velocity is shown in figure 2.1. The phase velocity equals the speed of light when $k_z = k \Leftrightarrow k_r = 0$. A higher phase velocity is found for $k_r^2 > 0$, a smaller phase velocity is found for $k_r^2 < 0$. Obviously the variable k_r switches from real to imaginary values. For the calculation of derivatives it is therefore necessary to use the variable $\xi = k_r^2$ instead.

The group velocity can be derived from

$$\frac{v_{gr}}{c} = \frac{\mathrm{d}k_m}{\mathrm{d}k_z}. \tag{2.32}$$

The differentials can be calculated by

$$dk_m = \frac{\mathrm{d}k_m}{\mathrm{d}k_r}\frac{\mathrm{d}k_r}{\mathrm{d}\xi}d\xi \tag{2.33}$$

$$dk_z = \left(\frac{\partial k_z}{\partial k_r} + \frac{\partial k_z}{\partial k_m}\frac{\mathrm{d}k_m}{\mathrm{d}k_r}\right)\frac{\mathrm{d}k_r}{\mathrm{d}\xi}d\xi$$

Dividing the differentials yields

$$\frac{v_{gr}}{c} = \frac{\frac{\mathrm{d}k_m}{\mathrm{d}k_r}}{\frac{\partial k_z}{\partial k_r} + \frac{\partial k_z}{\partial k_m}\frac{\mathrm{d}k_m}{\mathrm{d}k_r}}, \tag{2.34}$$

where the different terms are given as follows (see appendix A).

$$\frac{\mathrm{d}k_m}{\mathrm{d}k_r} = \frac{\varepsilon k_r b}{2 k_m (\varepsilon - 1)\delta}\left(\frac{\mathrm{J}_2(k_r b)\mathrm{J}_0(k_r b)}{\mathrm{J}_1^2(k_r b)} - \frac{2\delta}{b\varepsilon} - 1\right)$$

$$\frac{\partial k_z}{\partial k_r} = -\frac{k_r}{k_z} \tag{2.35}$$

$$\frac{\partial k_z}{\partial k_m} = \frac{k_m}{k_z}$$

The terms $\frac{\mathrm{d}\xi}{\mathrm{d}k_r}$ cancel and have been dropped. At $k_r^2 = 0$ there is a solvable discontinuity in this formula. The equation 2.47 shows the series expansion around this point.

With a dielectric surface layer the electromagnetic waves are slowed down so that there is a certain frequency at which the phase velocity of the wave equals the speed of light. At this frequency there is the possibility for a continuous energy transfer from a ultra-relativistic beam to the waveguide mode. In the following this will be called the synchronous mode wake field.

The frequency of the synchronous mode can be found by calculating k for $k_r = 0$. The right hand side of equation 2.29 becomes $b/2$ in the limit $k_r \rightarrow 0$. Using again the approximation $\tan(x) \approx x$, one finds

$$k_{res} = \sqrt{\frac{2\varepsilon}{(\varepsilon - 1)b\delta}}. \tag{2.36}$$

This the wavenumber of the synchronous mode. To obtain the excitation strength and pulse form of the mode one has to calculate the longitudinal impedance $Z_\parallel(k_z, \triangle k)$.
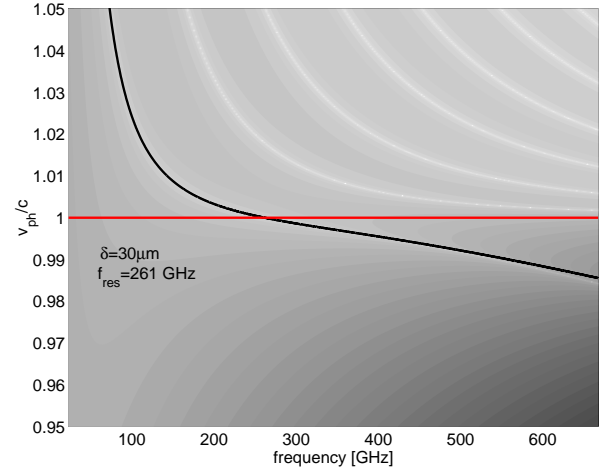

Figure 2.2: Absolute value of the impedance of a dielectrically coated beam pipe in the frequency-phase velocity plane (eq 2.40). The value of the impedance is coded into the gray scale of the picture, the coding is logarithmic to account for the diverging behaviour when matching the waveguide modes. The bright lines in the map correspond to the divergence of the impedance at a certain waveguide mode. The phase velocity of the lowest mode is plotted as black curve according to eq. 2.31. Note that the impedance was calculated exactly whereas eq. 2.31 is based on an approximation of the tangent. The two calculations deviate slightly at very high frequencies.

The longitudinal impedance is found by evaluating the quotient $\tilde{E}_z(0, k_z, k)/q$. To do so the surface impedance can be utilized

$$\tilde{E}_z(b, k_z, k) = \mathcal{Z}\tilde{H}_{\varphi, total} \tag{2.37}$$
$$= \mathcal{Z}\cdot\left(\frac{qc}{2\pi b} + \tilde{H}_\varphi(b, k_z, k)\right).$$

Inserting the general solution of the wave equation in vacuum, eq. 2.21 the longitudinal beam impedance (per unit length) is found

$$\frac{qcZ_0}{2\pi b} = \hat{E}\left(\frac{ik}{k_r}\mathrm{J}_1(k_r b) + \frac{Z_0}{\mathcal{Z}}\mathrm{J}_0(k_r b)\right) \tag{2.38}$$

$$\Leftrightarrow Z_\parallel = \frac{\tilde{E}_z}{qc}$$

$$= \frac{Z_0}{2\pi b}\cdot\frac{1}{\frac{ik}{k_r}\mathrm{J}_1(k_r b) + \frac{Z_0}{\mathcal{Z}}\mathrm{J}_0(k_r b)}. \tag{2.39}$$

Inserting the surface impedance from equation 2.28 yields

$$Z_\parallel = \frac{Z_0}{2\pi b}\cdot\frac{1}{\frac{ik}{k_r}\mathrm{J}_1(k_r b) - \frac{ik\varepsilon}{\kappa_r}\mathrm{J}_0(k_r b)\cot(\kappa_r\delta)}. \tag{2.40}$$

Figure 2.2 shows the impedance map for a beam pipe of 4 mm radius and 30 μm dielectric surface

layer. In the case of an infinitely long beam pipe only the impedance along the line $v_{ph} = c$ has to be taken into account. This is equivalent to taking $k_r = 0$

$$Z_{\parallel} = -\frac{1}{2\pi b} \cdot \frac{\mathcal{Z}}{1 + i\frac{kb\mathcal{Z}}{2Z_0}} \qquad (2.41)$$

$$\Leftrightarrow Z_{\parallel} = i\frac{Z_0}{\pi b^2} \cdot \frac{k}{k_{res}^2 - k^2}. \qquad (2.42)$$

The longitudinal wake function can be calculated via Fourier transform

$$
\begin{aligned}
w_{\parallel}^{\delta}(\zeta) &= \frac{c}{2\pi} \int_{-\infty}^{\infty} dk\, Z_{\parallel}(k) e^{-ik\zeta} \\
&= -\frac{Z_0 c}{\pi b^2} \cos(k_{res}\zeta)\Theta(\zeta), \quad (2.43)
\end{aligned}
$$

with $\zeta = z - ct$ the relative coordinate behind the source charge and Θ the Heaviside step function. Note that this wake function contains a cosine term even though the impedance is purely imaginary.

To evaluate the wake function for a finite beam pipe one has to take into account the impedance in the whole (k_z, k)-plane. To ease the calculation of the residua one can try to write the impedance as a product of polynomial quotients

$$
\begin{aligned}
Z_{\parallel} &= \frac{Z_0}{\pi b^2} \cdot \frac{ik}{k_r \varepsilon \frac{J_0(k_r b)}{J_1(k_r b)} - (k^2\varepsilon - k_z^2)\delta} \\
&\quad \cdot \frac{k_r b}{2 J_1(k_r b)} \cdot \frac{(k^2\varepsilon - k_z^2)\delta}{k^2} \\
&= \frac{Z_0}{\pi b^2} \cdot \frac{ik}{k_r \varepsilon \frac{J_0(k_r b)}{J_1(k_r b)} - k_r^2\delta - k^2(\varepsilon-1)\delta} \\
&\quad \cdot \frac{k_r b}{2 J_1(k_r b)} \cdot \frac{(k^2\varepsilon - k_z^2)\delta}{k^2} \\
&= \frac{Z_0}{\pi b^2} \cdot \frac{ik}{\frac{\varepsilon}{(\varepsilon-1)b\delta}\left[k_r b\frac{J_0(k_r b)}{J_1(k_r b)} - \frac{b\delta}{\varepsilon}k_r^2\right] - k^2} \\
&\quad \cdot \frac{k_r b}{2 J_1(k_r b)} \cdot \frac{k^2\varepsilon - k_z^2}{k^2\varepsilon - k^2}
\end{aligned}
$$

Using equation 2.31

$$Z_{\parallel} = i\frac{Z_0}{\pi b^2} \cdot \frac{k}{k_m^2 - k^2} \cdot \frac{1}{J_0(k_r b) + J_2(k_r b)} \cdot \frac{k^2\varepsilon - k_z^2}{k^2\varepsilon - k^2}. \qquad (2.44)$$

To evaluate the Fourier integral it is preferable to write k as function of k_z, which is achieved by using the Taylor series expansion up to the 3rd order. First one finds the series expansion of k and k_z from equation 2.31 with $\xi = k_r^2$ (See appendix A)

$$
\begin{aligned}
\frac{k_m}{k_{res}} &= 1 - \frac{1}{2}a_m\xi - \left(\frac{a_m^2}{8} + \frac{b^4}{384}\right)\xi^2 \qquad (2.45) \\
&\quad - \left(\frac{a_m^3}{16} + \frac{a_m b^4}{768} + \frac{b^6}{9216}\right)\xi^3 + \cdots
\end{aligned}
$$

$$
\begin{aligned}
\frac{k_z}{k_{res}} &= 1 - \frac{1}{2}a_r\xi - \left(\frac{a_r^2}{8} + \frac{b^4}{384}\right)\xi^2 \\
&\quad - \left(\frac{a_r^3}{16} + \frac{a_r b^4}{768} + \frac{b^6}{9216}\right)\xi^3 + \cdots
\end{aligned}
$$

with

$$a_m = \frac{b^2}{8} + \frac{b\delta}{2\varepsilon} \qquad a_r = \frac{b^2}{8} + \frac{b\delta}{2} \qquad (2.46)$$

The Taylor series then reads

$$
\begin{aligned}
k_m &= k_{res} + \frac{a_m}{a_r}(k_z - k_{res}) \qquad (2.47) \\
&\quad + \frac{b^4 - 48\,a_m a_r}{48\,a_r^3 k_{res}^2} \cdot \frac{(k_z - k_{res})^2}{2k_{res}}
\end{aligned}
$$

$$+ \left(\frac{a_m a_r b^4 - 48a_m^2 a_r^2}{16\,a_r^5 k_{res}^2} - \frac{48a_r^2 b^4 - 4a_r b^6 + b^8}{768\,a_r^5 k_{res}^2}\right)\frac{(k_z - k_{res})^3}{6k_{res}^2}$$

For small values of k_z the influence of the dielectric vanishes. Then a better approximation is given by the well known formula $k_m = \sqrt{k_z^2 + \alpha_1^2/b^2}$, with α_1 being the first zero of the Bessel function J_0. The coefficient of the first order is the group velocity close to the synchronous mode frequency

$$v_g = a_m/a_r. \qquad (2.48)$$

Given these functions it is possible to construct the Fourier transform of equation 2.44 in two dimensions

$$
\begin{aligned}
w_{\parallel}^{\delta}(z,t) &= \frac{Z_0 c}{\pi b^2} \int_{-\infty}^{\infty}\int_{-\infty}^{\infty} \frac{dk}{\sqrt{2\pi}}\frac{dk_z}{\sqrt{2\pi}}\frac{ik}{k_m^2 - k^2} \qquad (2.49) \\
&\quad \cdot \frac{k^2\varepsilon - k_z^2}{(\varepsilon-1)kk_z} \cdot \frac{k_r b}{2 J_1(k_r b)} \cdot e^{i(k_z z - kct)}
\end{aligned}
$$

The integration along k can be performed analytically using the residue theorem, if the zeros of the Bessel function in the third factor are neglected. They belong to distinct modes of higher order (see the bright lines in figure 2.2) which can be analyzed separately. Due to their high phase velocity, a coupling to the beam is not to be expected. Then,

$$w_{\parallel}^{\delta}(\zeta,l) = \qquad (2.50)$$

$$\frac{Z_0 c}{\pi b^2} \int_0^{\infty} dk_z \frac{k_m^2\varepsilon - k_z^2}{(\varepsilon-1)k_m k_z} \cdot \frac{k_r b}{2 J_1(k_r b)} \cdot \frac{\sin(\Delta_k l)}{\Delta_k} \cdot \cos(k_z\zeta),$$

where l is the position of the bunch in the beam pipe ($0 \le l \le L$, $\Delta_k = k_z - k_m$). The sine term originates from the finite duration of excitation. The integrand gives the wavelength spectrum of the radiation pulse depending on the position l of the bunch. The pulse can then be calculated numerically from
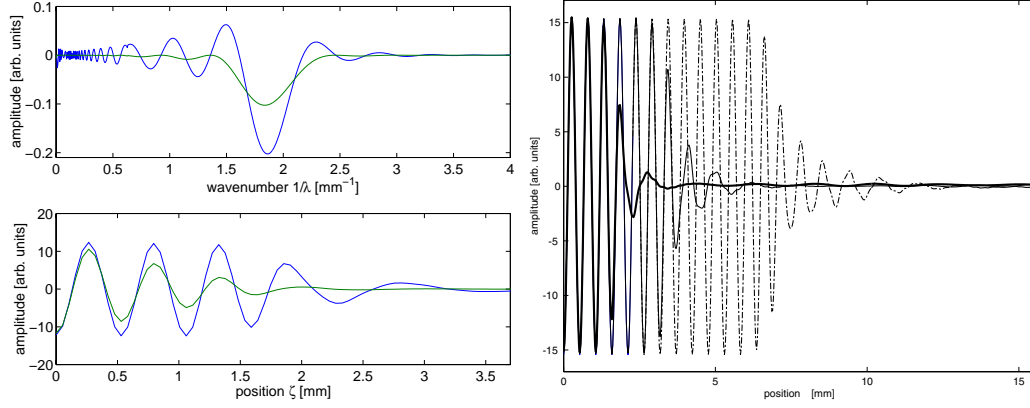
Figure 2.3: Spectrum and wake field pulse of a dielectric layer wake. The spectrum has been calculated with eq. 2.50, the pulse via fast Fourier transform (FFT) from the spectrum. The left hand picture shows the spectrum in the upper part and the pulse in the lower part. $W_\parallel^\delta$ and $w_\parallel^\delta$ are shown. The momentary pulse $w_\parallel^\delta$ is approximately rectangular. The integrated wake function $W_\parallel^\delta$ then drops linearly from the source charge to a distance $v_g L$ behind the source. The right hand picture shows the wake calculated after 50 cm, 1 m, and 2 m of beam pipe

the spectrum. The overall effect is obtained by integration along the path of the beam,

$$W_\parallel^\delta(\zeta, L) = \frac{Z_0 c}{\pi b^2} \int_0^L dl\, w_\parallel^\delta(\zeta, l). \quad (2.51)$$

The only quantity in the equation 2.50 that depends on l is the term $\sin(\Delta_k l)/\Delta_k$ which is easily integrated. Hence the overall wake function is

$$W_\parallel^\delta(\zeta, L) = \frac{Z_0 c}{\pi b^2} \int_0^\infty dk_z \frac{k_m^2 \varepsilon - k_z^2}{(\varepsilon - 1)k_m k_z} \cdot \frac{k_r b}{2 \mathrm{J}_1(k_r b)}$$
$$\cdot \frac{1 - \cos(\Delta_k L)}{\Delta_k^2} \cdot \cos(k_z \zeta). \quad (2.52)$$

The momentary wake field pulse described by equation 2.50 has a roughly rectangular shape. The integrated wake function then drops linearly from the source charge to a distance $v_g L$ behind the source (see figure 2.3 left).

For a given longitudinal bunch profile the wake potential is found by convolution of the wake function and the charge distribution. In figure 2.4 this is shown for a gaussian charge distribution and several different ratios of the wavelength and the σ of the Gauss function. The resulting corrections to the average and peak energy loss of the electrons in the bunch are shown in figure 2.5.

2.3 Surface Roughness

In the previous section it has been shown that wakes synchronous to the beam are excited if the phase velocity of the waveguide modes is slowed down to the speed of the beam. Such a wave can exist if there is
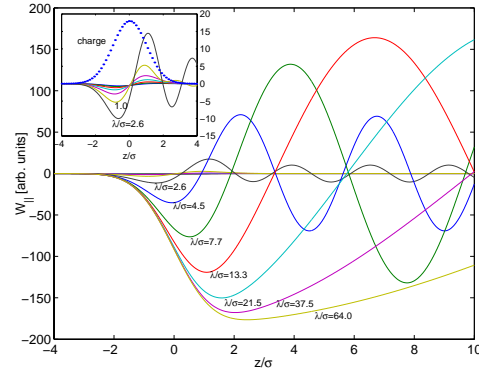
Figure 2.4: Wake potentials for different wavelengths λ of the synchronous mode. The inset shows a zoom into the area around the bunch and smaller amplitudes. The dotted plot gives the charge distribution, which is a gaussian $\sim \exp(-z^2/(2\sigma^2))$.

Figure 2.5: Maximum and average energy loss as function of the ratio of the wavelength λ of the synchronous mode and the rms spread σ of the bunch charge distribution. At $\lambda \approx \sigma$ there is the transition to a differentiating wake potential. The final value is obtained by multiplying with $qZ_0c/(\pi b^2)$.

8

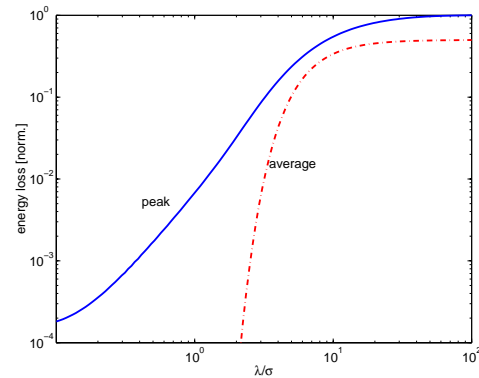a non-vanishing surface impedance, i.e. a longitudinal electric field at the surface is present. Surface roughness at the boundary surface will also produce a longitudinal electric field. The consequences are discussed in the following.
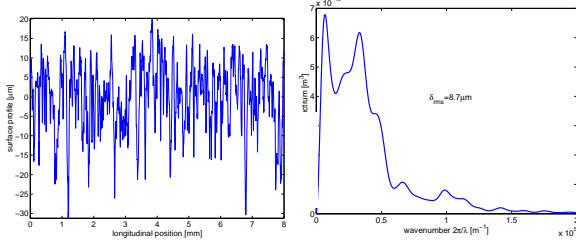

Figure 2.6: Surface profile of a sandblasted beam pipe. The right picture shows the corresponding spectrum $S(k)$. The normalization is such that $\int S dk = \delta_{rms}^2$, the rms height of the surface structures.

The figure 2.6 shows the surface profile of a beam pipe used in the wake field experiment.

2.3.1 Surface structure with a rectangular shape

A first attempt to model the surface roughness may be by means of periodic rectangular grooves. Since the height of the surface structures is much smaller than the radius of the beam pipe the surface is modelled as a plane. The electric and magnetic field components, however, are still labelled with the subscripts r, z, φ. The fields of the mode at the surface are written as

$$\tilde{E}_z = \mathcal{Z}\hat{H} \qquad \tilde{H}_\varphi = \hat{H} \qquad \tilde{E}_r = Z_0\hat{H}. \quad (2.53)$$

Let the periodicity of the gaps be d, g the width of the gaps, and δ the depth (see figure (2.7)). The fields inside the gaps can be expanded into eigenmodes

$$E_z^{(n)}(y,z) = a_n \sin(\sqrt{k^2 - \alpha_n^2}\,y)\cos(\alpha_n z) \quad (2.54)$$
$$E_r^{(n)}(y,z) = -\frac{\alpha_n a_n}{\sqrt{k^2 - \alpha_n^2}}\cos(\sqrt{k^2 - \alpha_n^2}\,y)\sin(\alpha_n z)$$
$$H_\varphi^{(n)}(y,z) = \frac{ika_n}{Z_0\sqrt{k^2 - \alpha_n^2}}\cos(\sqrt{k^2 - \alpha_n^2}\,y)\cos(\alpha_n z)$$
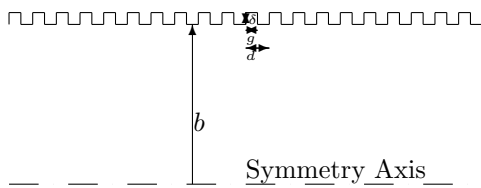$$\alpha_n = \frac{n\pi}{g}.$$

Figure 2.7: Sketch of the rectangular surface structure. The structures are axially symmetric.

Assuming that the wavelength of the mode inside the beam pipe is much larger than the gap width, one finds that the longitudinal electrical field is the average of the field in the gaps and that it is sufficient to calculate the lowest order mode inside the gap

$$\hat{E} = \mathcal{Z}\hat{H} \quad = \quad \frac{g}{d}a_0\sin(k\delta). \quad (2.55)$$

Under this assumption it is clear that no periodicity is required any more. The coefficient a_0 can be calculated from the boundary conditions at the gap entrance

$$H_\varphi^{(0)} \quad = \quad \tilde{H}_\varphi, \quad (2.56)$$
$$E_z^{(0)} \quad = \quad iZ_0 H_\varphi^{(0)} \quad (2.57)$$
$$\Leftrightarrow \mathcal{Z}_{rec} \quad = \quad iZ_0\frac{g}{d}\tan(k\delta) \approx iZ_0\frac{g}{d}k\delta. \quad (2.58)$$

Comparison with eq. 2.29 reveals some similarity with the surface impedance due to the dielectric layer when setting $k_z \approx k$. The effective dielectric constant is

$$\varepsilon_{eff} \quad = \quad \frac{d}{d-g}. \quad (2.59)$$

Hence wakes induced by this kind of surface roughness are equivalent to the wakes due to a thin dielectric layer. On page 76 of ref [52] the result of the above calculation has been compared to numerical calculations. Good agreement has been found for symmetric gaps $g \approx d/2$. Deviations are found when moving away from this situation, higher order modes have to be taken into account in this case.

Detailed numerical calculations have been performed at the Technical University Darmstadt to study the surface roughness wake fields for different geometrical structures [33, 52, 34]. The layer thickness δ is calculated from the rms height of the surface structure. In many cases a permittivity $\varepsilon \approx 2$ was found.

2.3.2 Smooth and shallow corrugations

In [12] Dohlus derives the surface impedance due to random corrugations. An analytical approach is developed using different approximations for the boundary conditions. Axial symmetry and longitudinal periodicity is assumed but no restrictions on the period length Λ. The boundary condition at the surface of the beam pipe is given by

$$\nabla H_\varphi \cdot \vec{n} + (i\omega\varepsilon_0 Z_b + (\vec{e}_r \cdot \vec{n})/b)\,H_\varphi \quad = \quad 0, \quad (2.60)$$

with $\vec{n}$ the normal to the surface and

$$Z_b(\omega) \quad = \quad \sqrt{i\frac{\omega Z_0}{c\sigma}} = \frac{1+i}{\sigma\delta_s}, \quad (2.61)$$

σ the conductivity and δ_s the skin depth. The electromagnetic field is expanded into eigenmodes up to order N

$$H_\varphi = H_\varphi^\delta + \sum_n C_n H_{\varphi n} \qquad (2.62)$$

$$E_r = E_r^\delta + \sum_n C_n E_{rn} \qquad (2.63)$$

$$E_z = \sum_n C_n E_{zn}, \qquad (2.64)$$

with $n = -N \ldots N$, $k_{zn} = k + nk_1$, $k_1 = 2\pi/\Lambda$,

$$H_\varphi^\delta = \tilde{H}_\varphi^\delta e^{ikz} \qquad H_{\varphi n} = -\frac{ik}{Z_0 k_{rn}} \mathrm{J}_1(k_{rn}r) e^{ik_{zn}z} \quad (2.65)$$

$$E_r^\delta = \tilde{E}_r^\delta e^{ikz} \qquad E_{rn} = -\frac{ik_{zn}}{k_{rn}} \mathrm{J}_1(k_{rn}r) e^{ik_{zn}z} \quad (2.66)$$

$$E_{zn} = \mathrm{J}_0(k_{rn}r) e^{ik_{zn}z} \qquad (2.67)$$

and $k_{rn} = \sqrt{k^2 - k_{zn}^2}$. In this notation the beam impedance is

$$Z_{beam} = \frac{C_0}{qc}. \qquad (2.68)$$

The left hand side of equation 2.60 can be evaluated for each eigenmode

$$h_\delta(z) = \left\{ \nabla H_\varphi^\delta \cdot \vec{n} + \left(ik\frac{Z_b}{Z_0} + \frac{\vec{e}_r \cdot \vec{n}}{R} \right) H_\varphi^\delta \right\}_{R=b(z)} \quad (2.69)$$

$$h_n(z) = \left\{ \nabla H_{\varphi n} \cdot \vec{n} + \left(ik\frac{Z_b}{Z_0} + \frac{\vec{e}_r \cdot \vec{n}}{R} \right) H_{\varphi n} \right\}_{R=b(z)} \quad (2.70)$$

The expansion coefficients C_n have to be chosen such that the boundary condition is fulfilled. In general there will be a deviation d which has to be minimized

$$d(z) := h_\delta(z) + \sum_n C_n h_n(z) \to 0, \quad (2.71)$$

There are several ways to approximate this problem which is continuous in z. The method chosen here is to fulfill the condition (2.71) exactly for the Fourier coefficients $F_m\{d(z)\}$ with $m = -N \ldots N$, and

$$F_m\{f\} = \frac{1}{\Lambda} \int_0^\Lambda f(z) e^{-imk_1 z} dz. \quad (2.72)$$

This yields the matrix equation

$$\tilde{M}c + \tilde{v} = 0, \qquad (2.73)$$

with

$$(\tilde{M})_{\hat{m},\hat{n}} = F_m\{h_n\}, \qquad (c)_{\hat{n}} = C_n$$
$$(\tilde{v})_{\hat{m}} = F_m\{h_\delta\}, \qquad (2.74)$$

where $\hat{n} = n + N + 1$ so that the numbering of the matrix elements starts at 1. It is advantageous to calculate the effective surface impedance first

$$\mathcal{Z}(\omega) = \frac{\langle E_z(b,z) e^{-ikz} \rangle_z}{\langle H_\varphi(b,z) e^{-ikz} \rangle_z}. \qquad (2.75)$$

This is accomplished by calculating

$$(\hat{M})_{\hat{m},\hat{n}} = \begin{cases} (\tilde{M})_{\hat{m},\hat{n}} + \frac{ik\pi b^2}{qcZ_0}(\tilde{v})_{\hat{m}} & \text{if } n=0, \\ (\tilde{M})_{\hat{m},\hat{n}} & \text{otherwise} \end{cases} \quad (2.76)$$

$$\hat{c} = -2\pi b \hat{M}^{-1}\tilde{v}, \qquad (2.77)$$

and then

$$\mathcal{Z}\omega = -\frac{\hat{C}_0}{q}, \qquad \hat{C}_n = (\hat{c})_{\hat{n}}. \qquad (2.78)$$

The terms $h^\delta(z)$ and $h_n(z)$ in the boundary condition can be linearized with respect to the surface profile $\delta_r(z)$

$$h_\delta(z) = \frac{qc}{2\pi b}\left(-ik_{z,0}\delta_r' + (1 - \delta_r/b)ik\frac{Z_b}{Z_0}\right)e^{ik_{z,0}z} \quad (2.79)$$

$$h_n(z) = -\left[\mathrm{J}_0(k_{rn}b)\left(1 + ik\delta_r\frac{Z_b}{Z_0}\right)\right. \qquad (2.80)$$

$$\left. + \mathrm{J}_1(k_{rn}b)\left(-i\frac{k_{zn}}{k_{rn}}\delta_r' - k_{rn}\delta_r + ik\frac{Z_b}{Z_0}\frac{1 - \delta_r/b}{k_{rn}}\right)\right]e^{ik_{zn}z}.$$

This approximation is valid if $\delta_r \ll b$, $\delta_r' \ll 1$, and $|k_{rn}\delta_r| \ll 1$. A first order approximation for the inverse matrix $\hat{M}^{-1}$ is applied. This then yields a second order approximation for the surface impedance

$$\mathcal{Z}(k) = Z_b + iZ_0 k \sum_{n=-N}^{N} \mathcal{A}_n\left(nk_1 - i\frac{1}{b}\frac{Z_b}{Z_0}\right)|F_n\{\delta_r\}|^2,$$

$$\mathcal{A}_n = \frac{\left[i\mathrm{J}_1'(k_{r,n}b)\frac{Z_b}{Z_0} + \mathrm{J}_1(k_{r,n}b)nk_1/k_{r,n}\right]}{\mathrm{J}_0(k_{r,n}b) + ik\mathrm{J}_1(k_{r,n}b)/k_{r,n}\frac{Z_b}{Z_0}} \qquad (2.81)$$

The influence of the surface resistivity can be further approximated

$$\mathcal{Z}(k) = Z_b + i\omega\frac{Z_0}{c}\sum_{n=-N}^{N}\frac{\mathrm{J}_1(k_{r,n}b)(nk_1)^2}{k_{r,n}\mathrm{J}_0(k_{r,n}b)}|F_n\{\delta_r\}|^2$$

$$+ \mathcal{O}(\|\delta_r\|^2 Z_b), \qquad (2.82)$$

In [12] this last approximation has only been derived for a sinusodial surface profile. Due to the similarity to the case of the Fourier series this may be generalized. With a less rigorous treatment Stupakov [48] finds an approximation for the surface impedance without using axial symmetry

$$\mathcal{Z} = i\omega\mathcal{L} \qquad (2.83)$$

$$\mathcal{L} = \frac{Z_0}{c}\int_{-\infty}^{\infty}\int_{-\infty}^{\infty} d\kappa_z d\kappa_x R(\kappa_z, \kappa_x)\frac{\kappa_z^2}{\kappa}, (2.84)$$

with z parallel to the direction of the beam and x perpendicular. $R(\kappa_z, \kappa_x)$ is the Fourier transform of the autocorrelation of the surface profile function $\delta_r(z, x)$. The integral $\mathcal{L}$ is regarded as surface inductance, similar to the second term in equation 2.82.

Figure 2.8: Beam impedance due to surface roughness. The beam impedance is calculated using the equation 2.82. The parameters of the pipe are radius $b = 5$ mm and a surface profile as depicted in figure 2.6. The visual impression of the spectrum is dominated by the many narrow resonances due to the resonances of the surface impedance. Calculating the average contribution to the power integral (right picture) results in a single resonance at 620 GHz.
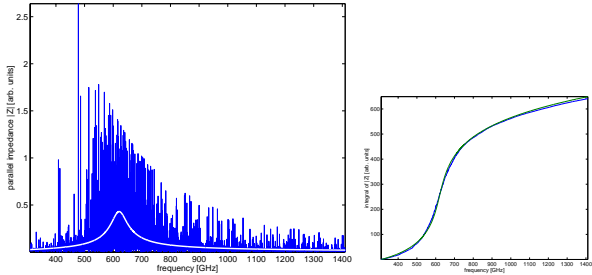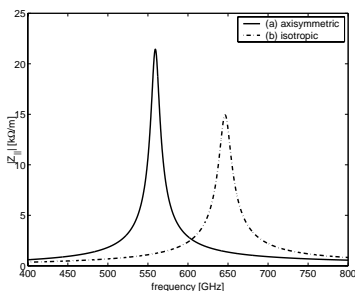

Figure 2.9: Beam impedance due to surface roughness. The beam impedance is calculated using the equation 2.83. The parameters of the pipe are radius $b = 5$ mm and a surface profile as depicted in figure 2.11. The beam impedance plotted with a solid line results if one assumes that the roughness is axially symmetric. The dashed-dotted line shows the impedance assuming that the roughness is isotropic on the surface.

Setting $R = R(\kappa_z)\delta(\kappa_x)$ resulting in an axisymmetric surface, the two models can be compared. The first and most striking difference is the dependence on the pipe radius. In this sense the interpretation of the surface impedance as a property of the surface only is no longer correct. This difference becomes important for frequencies $\omega > 2k_1 c$, when there are modes above cutoff, which are no longer localized on the surface. In these cases there are resonances in the surface impedance and due to their oscillatory behaviour also in the beam impedance.

Note: One of the major advantages of using the surface impedances for analyzing the wake fields is the fact that the surface impedance is finite where there is a singularity in the beam impedance and vice versa (see eq. 2.39). Therefore the numerical study of the resonances is much more precise in this way.

The figure 2.8 shows the beam impedance due to the surface roughness measured in a pipe used for the wake field experiment. The impedance has been calculated using 2.82. For low frequencies $k_0 \ll k_1$ the term $J_1(k_r b)/(k_r J_0(k_r b)) \approx 1/k_r \approx 1/k_1$. In this case the equation 2.82 and 2.83 deliver similar results. The additional resonances lead to additional energy losses. Therefore the resonance in figure 2.8 is approximately 4 times wider than it would be according to surface resistance and inductivity alone.

The figure 2.9 shows the beam impedance calculated using equation 2.83. The impedance has been calculated assuming axial symmetry and for an isotropic roughness distribution on the surface. For isotropic surface structures the autocorrelation function only depends on $\xi = \sqrt{(x - x')^2 + (z - z')^2}$

$$K(\xi) = <\delta_r(x)\delta_r(x + \xi)> . \qquad (2.85)$$

The Fourier transform of K

$$R(\kappa_z, \kappa_x) = \frac{1}{4\pi^2} \int\limits_{-\infty}^{\infty}\int\limits_{-\infty}^{\infty} dz dx K(\xi) e^{-i(\kappa_z z + \kappa_x x)} \quad (2.86)$$

turns into a Hankel transform

$$R(\kappa) = \frac{1}{2\pi} \int\limits_{0}^{\infty} \xi d\xi K(\xi) J_0(\kappa\xi). \qquad (2.87)$$

The figures 2.10 resp. 2.11 show the functions K and R for the sandblasted beam pipes. The autocorrelation function (figure 2.10) has been obtained averaging 18 sets of 1-dimensional data only. This leads to rather poor results for large offsets, where the mean values are smaller than the rms. These have been suppressed in the calculation by multiplying a gaussian function with a suitable σ. In figure 2.11 the spectra R have been plotted for comparison. They are given such that one directly can obtain

$$\mathcal{L} = \frac{Z_0}{c} \int\limits_{0}^{\infty} \kappa d\kappa \hat{R}(\kappa). \qquad (2.88)$$

In the isotropic case this requires a multiplication with κ. The integrals for the two cases differ by a factor 0.7450, for a gaussian distribution one finds a factor $\pi/4 \approx 0.785$. This results in a surface inductance according to Stupakov et. al. [48]

$$\mathcal{L}_{symm} \approx 3.6 \text{ pH} \qquad \mathcal{L}_{iso} \approx 2.7 \text{ pH}. \quad (2.89)$$

Taking the rms value of the surface profile $\delta_{rms} \approx 10\,\mu m$ as the layer thickness, this results in effective dielectric constants

$$\varepsilon_{symm} \approx 1.4 \qquad \varepsilon_{iso} \approx 1.27 \quad . \qquad (2.90)$$
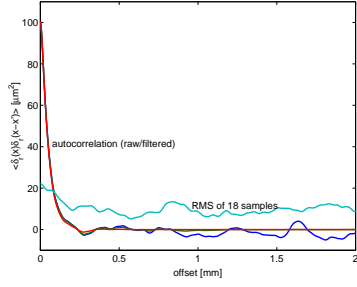
Figure 2.10: Autocorrelation function of the surface rough-
ness averaged over 18 sample measurements. A Gauss func-
tion has been multiplied to the averaged function in order
to suppress random noise at large offsets. The sigma of the
gaussian is chosen such that it becomes efficient at the point
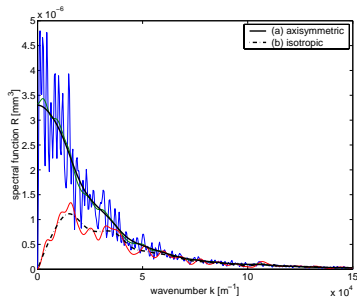when the signal is as large as the RMS value of the fluctua-
tions.

Figure 2.11: Spectral functions of the surface roughness.
The spectral functions have been calculated (a) by a Fourier
transform (axial symmetric structures) and (b) using the
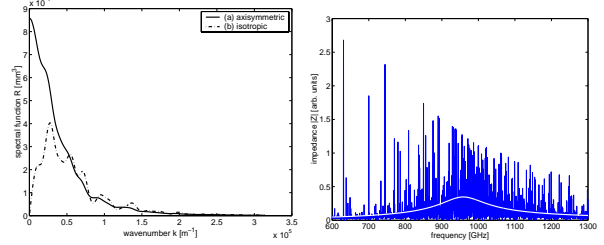Hankel transform (isotropic structures).

Figure 2.12: Spectral functions of the surface roughness and
the corresponding impedance of the collimator. The spectral
functions have been calculated (a) by a Fourier transform
and (b) using the Hankel transform. The beam impedance
of the spoiler has been calculated assuming a constant radius
of 3 mm.

Assuming that the same spectrum can be used in
the model 2.82 as well, the curve in figure 2.8 was
calculated. The corresponding inductances accord-
ing to the Dohlus model are

$$\mathcal{L}_{symm} \approx 3.6 \text{ pH} \qquad \mathcal{L}_{iso} \approx 3.0 \text{ pH}, \quad (2.91)$$

and the corresponding dielectric constants are

$$\varepsilon_{symm} \approx 1.4 \qquad \varepsilon_{iso} \approx 1.31 \quad . \quad (2.92)$$

The Dohlus model (eq. 2.82) fits better with the
experimental data than the Stupakov model (eq.
2.83). See chapter 7 for reference. In the fig-
ures 2.12 and 2.13 the impedances of the surface
roughness wake in the collimator and undulator are
shown. In the undulator the surface roughness wake
adds little to the wake field due to surface resistiv-
ity.

Figure 2.13: Spectral functions of the surface roughness and
corresponding impedance of the undulator vacuum cham-
ber. The spectral functions have been calculated (a) by a
Fourier transform and (b) using the Hankel transform. The
beam impedance of the undulator has been calculated for
the radius of 4.5 mm. The surface roughness wake is a small
correction to the resistive wall wake.

2.3.3 Time Constants

The dielectric layer model can be applied to calcu-
late the group velocity of the roughness wake and

hence its pulse length. The surface inductance can be translated into an effective dielectric constant

$$\varepsilon = \frac{1}{1 - \mathcal{L}c/(\delta Z_0)}. \qquad (2.93)$$

The pulse length $L_p = L(c - v_g)/c$ can be calculated by

$$
\begin{aligned}
L_p &= L\left(1 - \frac{a_m}{a_r}\right) \\
&= L\left(1 - \frac{b^2/8 + b\delta/(2\varepsilon)}{b^2/8 + b\delta/2}\right) \\
&= L\frac{\varepsilon - 1}{\varepsilon} \cdot \frac{\delta/2}{b/8 + \delta/2} \\
&\approx L\frac{\varepsilon - 1}{\varepsilon} \cdot \frac{4\delta}{b} \qquad (2.94) \\
&= 4L\frac{\mathcal{L}c}{Z_0 b}. \qquad (2.95)
\end{aligned}
$$

Losses in the system are accounted for by multiplication with the corresponding exponentially decaying function with a characteristic decay length ζ_0. For the wake function this may result in a change of the decay constant

$$
\begin{aligned}
W_\parallel^\delta &= \frac{Z_0 c}{\pi b^2}\cos(k_{res}\zeta)\cdot(1 - \zeta/L_p)\cdot\exp(-\zeta/\zeta_0), \\
&\approx \frac{Z_0 c}{\pi b^2}\cos(k_{res}\zeta)\cdot\exp(-\zeta/\zeta_1), \qquad (2.96) \\
\zeta_1 &= \left(\frac{1}{L_p} + \frac{1}{\zeta_0}\right)^{-1}, \qquad 0 \le \zeta \le L_p. \qquad (2.97)
\end{aligned}
$$

Taking into account only the surface resistance below 1 THz the damping leads to a small correction to the lossless pulse length. The large number of resonances in the Dohlus model causes additional losses for the harmonic wake. This results in a broadening of the average resonance which can be translated into a shorter damping constant. This shorter decay constant dominates (see figure 7.15).

2.3.4 Further Reading

In recent years the topic of surface roughness wake fields has received considerable attention in many – mainly theoretical – publications and contributions to conferences. Besides the publications already cited in the previous sections [33, 52, 34, 12, 48] other papers are mentioned at this point. The treatment in [48] is based on [47], but it should be noted that in the latter the existence of a synchronous mode is denied. Closely related are the publications [4, 6, 7, 49, 50]. In connection with the dielectric layer model [32, 5] should be mentioned. In [38] the dielectric layer model is tested for its physical meaning. The report [13] applies several models on the case of the TESLA X-FEL.
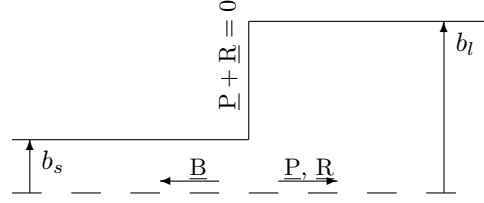

Figure 2.14: Jump in the radius of a beam pipe.

In [1] some doubt is cast on the concept of a beam impedance per unit length. The calculations presented there result in a slowly oscillating energy transfer between beam and radiation field. The center frequencies are predicted to be linearly growing with the beam energy

$$k_n = \pm\frac{\alpha_n \gamma}{b}, \qquad (2.98)$$

with α_n the zeros of the Bessel function J_0 and b the radius of the beam pipe. In the wake field experiment with beam energy $\gamma \approx 460$ and pipe radius $b = 5$ mm the lowest frequency would have to be expected at 10 THz.

In [2] the surface roughness is treated as being regular with a rectangular shape resulting in a resonance at

$$k_{res} = \frac{\alpha_n}{\sqrt{b\delta}}, \qquad (2.99)$$

independent from the roughness structure in contrast to the treatment in section 2.3.1. In [27] the change of phase velocity of the waveguide modes is calculated depending on a statistical surface roughness. The conclusion drawn is that no resonant mode exists which is in contradiction to the experimental results described in chapter 7.

2.4 Stepchange in the Cross Section

When a sudden change of the cross section of the beam pipe occurs, wake field radiation is to be expected. In the wake field experiment jumps occur at the entrance and exit of the test pipes. At a reduction of the pipe radius (step in) the pan-cake field of the bunch is reflected at the aperture. At an expansion of the radius the pan-cake field has to be recreated. To fulfill the boundary conditions a radiation field is needed. In the first case no energy is lost, in the latter case twice the field energy of the self-field will be extracted from the beam. These effects have been treated in [23] and [24].

The radiated fields in the beam pipe are

$$\tilde{E}_z = \sum_n E_n \mathrm{J}_0\left(\nu_n \frac{r}{b}\right) \qquad (2.100)$$

$$\tilde{E}_r = i\,\mathrm{sign}(k)\sum_n E_n\sqrt{k^2 b^2/\nu_n^2 - 1}\,\mathrm{J}_1\left(\nu_n \frac{r}{b}\right) \quad (2.101)$$
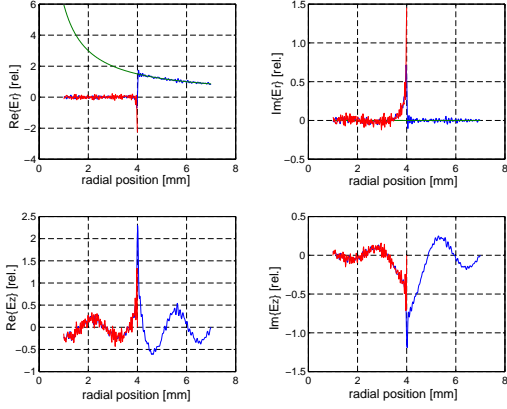
13

Figure 2.15: Fulfilling the boundary conditions at a 'step-out' transition. In this case a step from $r=4$ mm to 7 mm was assumed. In the upper left picture the self-field of the bunch has been drawn with the opposite sign to illustrate the matching of the fields, at the metal boundary they cancel to zero. The step in the real part of E_r causes a singularity in the real part of E_z.

with b the radius of the beam pipe and $\text{sign}(k) = \pm 1$ for fields radiated antiparallel respectively parallel with the beam. The radius of the smaller beam pipe is called b_s, that of the larger one b_l. The constants ν_n are the nth zeros of the Bessel function J_0.

The functions $J_0(\nu_n r/b)$, $J_1(\nu_n r/b)$ can be treated as orthogonal bases of a vector space of infinite dimension. A scalar product can be defined by

$$[f,g] = \int_0^b r\,dr\,f(r)\cdot g(r) \qquad (2.102)$$

The orthogonality of the bases can be verified easily

$$\left[J_0\left(\frac{\nu_n r}{b}\right), J_0\left(\frac{\nu_m r}{b}\right)\right] = \delta_{nm}\frac{b^2 J_1^2(\nu_n)}{2} \quad (2.103)$$

$$\left[J_1\left(\frac{\nu_n r}{b}\right), J_1\left(\frac{\nu_m r}{b}\right)\right] = \delta_{nm}\frac{b^2 J_1^2(\nu_n)}{2} \quad (2.104)$$

The bases are complete for axially symmetric electric fields. Any field pattern then can be written as a linear combination of the Bessel functions which are

$$f = \sum_n f_n J_{0/1}\left(\frac{\nu_n r}{b}\right) \qquad (2.105)$$

$$f_n = \frac{2}{b^2 J_1^2(\nu_n)}\left[f, J_{0/1}\left(\frac{\nu_n r}{b}\right)\right] \quad (2.106)$$

$$\underline{f}_{0/1} = (f_1, f_2, f_3, \ldots)_{0/1} \qquad (2.107)$$

In this notation the wake field calculation can be written as a system of algebraic equations. Let $\underline{P}$

be vector of the additional pan-cake field after the jump , $\underline{R}$ the field radiated parallel to the beam, and $\underline{B}$ the backward reflection. Since the pan-cake field is radial at the jump it has to be compensated by the radial part of the radiated field. Then the boundary and continuity conditions at a step-out transition are

$$\underline{R}_r = \underline{P} - \underline{B}_r \qquad (2.108)$$

$$\underline{R}_z = \underline{B}_z, \qquad (2.109)$$

The vector $\underline{P}$ is non-zero at the additional width of the larger pipe only ($r \geq b_s$), the vector $\underline{B}$ is non-zero only in the smaller pipe. The components of $\underline{P}$ are found by

$$P_n = \frac{2}{b_l^2 J_1^2(\nu_n)}\left[\frac{1}{r}, J_1\left(\frac{\nu_n}{b_l}r\right)\right]$$

$$= \frac{2}{b_l^2 J_1^2(\nu_n)}\int_{b_s}^{b_l} dr J_1\left(\frac{\nu_n}{b_l}r\right) \quad (2.110)$$

The components of $\underline{B}$ are used in two bases. Two transformation matrices have to be found

$$(BR)_{n,m} = \frac{2}{b_l^2 J_1^2(\nu_n)}\int_0^{b_s} dr J_1\left(\frac{\nu_n}{b_l}r\right) J_1\left(\frac{\nu_m}{b_s}r\right) \quad (2.111)$$

$$= 2\frac{b_s}{b_l^2}\frac{J_0(\nu_n \frac{b_l}{b_s})J_1(\nu_m)}{J_1^2(\nu_m)}\frac{\nu_m}{b_l(\nu_n^2/b_s^2 - \nu_m^2/b_l^2)},$$

$$(RB)_{n,m} = \frac{2}{b_l^2 J_1^2(\nu_n)}\int_0^{b_s} dr J_0\left(\frac{\nu_n}{b_l}r\right) J_0\left(\frac{\nu_m}{b_l}r\right) \quad (2.112)$$

The transformation from the radial to the longitudinal field is

$$(RR)_{n,n} = -\frac{i}{\text{sign}(k)\sqrt{k^2 b_l^2/\nu_n^2 - 1}} \quad (2.113)$$

for the larger pipe and

$$(BB)_{n,n} = \frac{i}{\text{sign}(k)\sqrt{k^2 b_s^2/\nu_n^2 - 1}} \quad (2.114)$$

for the smaller pipe. With these transformations the boundary conditions (2.108), (2.109) can be combined and rewritten

$$\underline{R}_r = \underline{P} - BR \cdot BB \cdot RB \cdot RR \cdot \underline{R}_r \quad (2.115)$$

$$\Leftrightarrow \underline{R}_r = (\mathbf{1} + BR \cdot BB \cdot RB \cdot RR)^{-1}\underline{P} \quad (2.116)$$

The figure 2.15 illustrates the fulfilling of the boundary conditions. Although the agreement is reasonable there is no perfect match at the boundaries. The coefficients of the modes do not converge fast enough. For the calculation of the longitudinal impedance this is no problem because the modes of higher contribute $\sim 1/n$ with an alternating sign.

14

The longitudinal impedance can be calculated from

$$Z = \frac{1}{q} \int_{-\infty}^{\infty} dz E_z(r=0)e^{ikz} \tag{2.117}$$

$$= \frac{1}{q} \sum_n E_n \int_{-\infty}^{\infty} dz e^{i(k-\sqrt{k^2-\nu_n^2/b^2})z} \tag{2.118}$$

For each element of the sum the integrand is non-zero in the intervall $(-\infty, 0]$ or $[0, \infty)$ respectively, depending on the direction of propagation of the corresponding wave. The integral can be performed for the evanescent waves. For the propagating waves the integral yields $\delta(k - k_z)$ which is always zero since they all have a phase velocity larger than c, but assuming an infinitesimal damping the result is finite

$$Z(k) = -\frac{i}{q} \sum_n \frac{E_n}{k - \sqrt{k^2 - \nu_n^2/b^2}}. \tag{2.119}$$

These calculations have to repeated for every frequency (see figure 2.16).

At frequencies far above cut-off the impedance approaches a constant value which can be calculated from the energy stored in the additional self field.

$$\mathcal{E} = 2\pi \int_{b_s}^{b_l} r dr \boldsymbol{E}^\delta \times \boldsymbol{H}^\delta \tag{2.120}$$

With a similar treatment the surface roughness wake field radiation emerging out of the test pipe can be calculated. Only the source terms have to be modified accordingly.
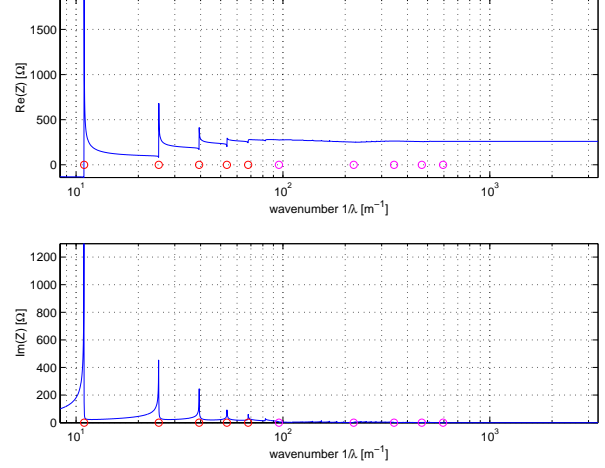

Figure 2.16: Real and imaginary part of the impedance of a step in the cross section. The dimensions are $b_s = 4$ mm for the smaller and $b_l = 35$ mm for the larger beam pipe as it is the case for the experiment. The first five cut-off wavenumbers have been marked for the two pipes.

Chapter 3

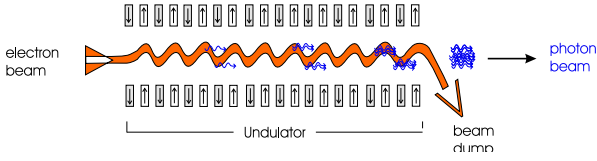# Introduction to Free Electron Lasers

Figure 3.1: Working principle of a SASE FEL [51]. The trajectory of the beam is perpendicular to the magnetic field, to become visible in the drawing it has been turned by 90°.

The description of the Free Electron Laser (FEL) given here is based on [39] and [26][25]. A more detailed description can be found in [41] and [53] and the references therein. The basic elements of an FEL are a bunched beam of highly relativistic electrons and an undulator magnet. A planar undulator produces a periodically oscillating dipole magnet field

$$B_y(z) = B_0 \sin(k_u z). \tag{3.1}$$

A relativistic electron that enters the undulator will be forced onto a sinusoidal trajectory. The undulator is built such that the maximum deflection angle $\vartheta \leq 1/\gamma$ with γ the relativistic factor of the electron. It is therefore justified to assume (for the moment) the forward speed v_z to be constant $\approx \beta c$ and $z = \beta ct$. Then it is easy to calculate the deviation x from the straight orbit

$$x(z) = \frac{eB_0}{\gamma m_0 c k_u^2} \cos(k_u z). \tag{3.2}$$

Introducing the dimensionless undulator parameter

$$K = \frac{eB_0}{m_0 c k_u} \approx 0.934 \cdot B_0[\text{T}] \cdot \lambda_u[\text{cm}] \tag{3.3}$$

the equation 3.2 can be written as

$$x(z) = \frac{K}{\gamma k_u \beta} \cos(k_u z). \tag{3.4}$$

In this notation K/γ characterizes the deflection angle in an undulator. The parameter K often is chosen to be in the order of 1.

Calculating the velocities inside the undulator now it is necessary to drop the assumption of constant speed in z-direction

$$\beta_x = \frac{K}{\gamma} \sin(k_u z), \tag{3.5}$$

$$\beta_x^2 + \beta_z^2 = 1 - \frac{1}{\gamma^2} \tag{3.6}$$

$$\begin{aligned}
\Rightarrow \beta_z &= \sqrt{1 - \frac{1}{\gamma^2} - \frac{K^2}{\gamma^2} \sin^2(k_u z)} \\
&\approx 1 - \frac{1}{2}\left[\frac{1}{\gamma^2} - \frac{K^2}{\gamma^2}\sin^2(k_u z)\right] \\
&= 1 - \frac{1}{2}\left[\frac{1}{\gamma^2} - \frac{K^2}{2\gamma^2}\sin^2(k_u z)\right. \\
&\qquad \left. - \frac{K^2}{2\gamma^2} + \frac{K^2}{2\gamma^2}\cos^2(k_u z)\right] \\
&= 1 - \underbrace{\frac{1 + K^2/2}{2\gamma^2}}_{\bar{\beta}} + \frac{K^2}{4\gamma^2}\cos(2k_u z). \tag{3.7}
\end{aligned}$$

Due to the oscillating motion the mean velocity $\bar{\beta}c$ is slower than βc. Undulator radiation is characterized by the coherent addition of the radiation field produced by a single electron at different positions along the undulator. FEL radiation in turn is characterized by coherent radiation by many electrons.

The electromagnetic wave moves parallel to the undulator axis and is polarized in the horizontal plane

$$\boldsymbol{E} = \boldsymbol{e}_x E_0 \cos(kz - \omega t + \theta_0), \tag{3.8}$$

with $\omega = kc$ and θ_0 the phase offset between the wave and the electron. Since the motion of the electron in the undulator has a component parallel to the electric field of the wave there is an energy transfer between the electron and the wave

$$\begin{aligned}
mc^2\frac{\mathrm{d}\gamma}{\mathrm{d}t} &= \boldsymbol{F} \cdot \boldsymbol{v} \\
&= \frac{eE_0 Kc}{\gamma}\sin(k_u z)\cos(kz - \omega t + \theta_0)
\end{aligned}$$

$$= \frac{eE_0 Kc}{2\gamma} \left[\sin(\underbrace{(k + k_u)z - \omega t + \theta_0}_{\theta}) \right.$$
$$\left. - \sin((k - k_u)z - \omega t + \theta_0) \right]. (3.9)$$

The first sine-term in 3.9 is slowly varying while the second has a fast oscillation and averages to zero [26]. Continuous energy transfer is achieved if the ponderomotive phase θ is constant

$$\theta = (k + k_u)z - \omega t + \theta_0 = const \quad (3.10)$$
$$\frac{d\theta}{dt} = (k + k_u)v_z - kc \overset{!}{=} 0. \quad (3.11)$$

Using the average velocity derived above

$$\frac{d\theta}{dt} = c \left[(k + k_u) \left(1 - \frac{1 + K^2/2}{2\gamma^2} \right) - k \right]. (3.12)$$

The FEL radiation has a wavelength in the order of 100 nm and below while the undulator period is in the order of cm, therefore $k_u/k \ll 1$

$$\frac{d\theta}{dt} = ck \left(\frac{k_u}{k} - \frac{1 + K^2/2}{2\gamma^2} \right) \overset{!}{=} 0. \quad (3.13)$$

This results in the resonant condition

$$\frac{\lambda}{\lambda_u} = \frac{1 + K^2/2}{2\overline{\gamma}^2}. \quad (3.14)$$

This is the formula for the undulator radiation in forward direction. This confirms the close relationship between undulator radiation and FEL radiation which can be compared to the relation between spontaneous and stimulated emission in lasers. The FEL radiation is referred to as stimulated radiation, while the undulator radiation is spontaneous radiation. The resonant gamma is denoted as $\overline{\gamma}$.

3.1 Pendulum Equation

A new variable is introduced

$$\eta = \frac{\gamma - \overline{\gamma}}{\overline{\gamma}} \ll 1, \quad (3.15)$$
$$\overline{\gamma}^2 = \frac{k}{k_u} \frac{1 + K^2/2}{2}. \quad (3.16)$$

Using this variable the time derivative of the phase angle is

$$\dot{\theta} = ck_u \left(1 - \frac{k}{k_u} \frac{1 + K^2/2}{2\gamma^2} \right)$$
$$= ck_u \left(1 - \frac{1}{(1 + \eta)^2} \right)$$
$$= ck_u \frac{2\eta + \eta^2}{1 + 2\eta + \eta^2}$$
$$\approx 2ck_u \eta. \quad (3.17)$$

Performing the 2nd time derivative and inserting equation 3.9 one finds

$$\frac{1}{2ck_u} \ddot{\theta} = 1 \frac{1}{\overline{\gamma}} \dot{\gamma} = \frac{eE_0 Kc}{2\gamma \overline{\gamma} mc^2} \sin \theta. \quad (3.18)$$

Because of its appearance this equation is referred to as the pendulum equation. The proper derivation of the phase dynamics has to take into account the oscillatory trajectory of the electrons instead of using only the average velocity $\overline{\beta}$. This can be done by replacing the undulator parameter K in 3.18 by [39][54]

$$K \to \tilde{K} = K \left[J_0 \left(\frac{K^2}{4 + 2K^2} \right) - J_1 \left(\frac{K^2}{4 + 2K^2} \right) \right] (3.19)$$

The pendulum equation is then changed to

$$\ddot{\theta} = \frac{eE_0 \tilde{K} c^2 k_u}{\gamma \overline{\gamma} mc^2} \sin \theta. \quad (3.20)$$

In an FEL amplifier with a significant growth of the radiated power the value of E_0 in 3.20 cannot be regarded as constant. In this case the inhomogeneous wave equation for the electric field and the FEL equations have to be solved simultaneously,

$$\left(\nabla^2 - \frac{1}{c^2} \frac{\partial^2}{\partial t^2} \right) \vec{E} = \mu_0 \frac{\partial \vec{J}}{\partial t} + \frac{\nabla \rho}{\varepsilon_0}. \quad (3.21)$$

To account for the granularity of the bunches the current and charge density are expressed as sums over the single electrons [39]

$$\vec{J} = -ec \sum_j \vec{\beta}_j(t) \delta(\vec{r} - \vec{r}_j(t)) \quad (3.22)$$

and

$$\rho = -e \sum_j \delta(\vec{r} - \vec{r}_j(t)) \quad (3.23)$$

The electric fields can be divided into two parts: The transverse field of the FEL radiation, and the longitudinal field due to space charge. Because of the short modulation wavelength the space charge forces cannot be neglected even for ultra-relativistic beams [39]. Due to the microbunching the dominating part of the longitudinal field is periodic and can be written as a Fourier series $E_z = \sum_l \hat{E}_l \exp[il\theta]$. Similar expressions hold for the charge and current. The wave equation for the longitudinal field is then

$$\left[\nabla_\perp^2 - (k + k_u)^2 + k^2 \right] \hat{E}_l$$
$$= -\frac{iel}{\varepsilon_0} \sum_j [\hat{\beta}_j k - (k + k_u)] e^{-il\theta_j} \quad (3.24)$$

For the radiation process the small differences in the electron velocities are negligible. Using the approximation $\beta_j \approx \overline{\beta} \approx 1 - k_u/k$ and $(k + k_u)^2 - k^2 \approx 2kk_u$ the equation becomes

$$\left[\nabla_\perp^2 - \frac{l^2 k^2 (1 + K^2)}{\overline{\gamma}^2} \right] \hat{E}_l = i \frac{elk(1 + K^2)}{\varepsilon_0 \overline{\gamma}^2} \sum_j e^{-il\theta_j} (3.25)$$

In a planar undulator the odd harmonics $l = 1, 3, 5, \ldots$ can be amplified. But here only the fundamental mode $l = 1$ is considered. The sum on the right hand side can be abbreviated by the bunching factor

$$< \exp(-i\theta) > \quad = \quad \frac{1}{N_e} \sum_j e^{-i\theta_j}. \quad (3.26)$$

In a planar undulator only horizontally polarized light is produced. Hence only the wave equation for the x-component of the radiation field has to be considered

$$\left[\nabla_\perp^2 + \left(\frac{\partial}{\partial z}\right)^2 - \left(\frac{1}{c}\frac{\partial}{\partial t}\right)^2\right] E_x = \frac{1}{\varepsilon_0 c^2}\left[\frac{\partial}{\partial t}J_x + c^2\frac{\partial\rho}{\partial x}\right]. \quad (3.27)$$

In the 1-dimensional theory the transverse derivative of the charge density on the right hand side can be neglected [26].

$$c^2\frac{\partial\rho}{\partial x} \ll \frac{\partial}{\partial t}J_x \quad (3.28)$$

The transverse current J_x is given by

$$J_x = -ecK\sin(k_u z)\sum_j \frac{1}{\gamma_j}\delta(z - z_j)\delta(\vec{x} - \vec{x}_j). \quad (3.29)$$

The transverse field is written as

$$\begin{aligned} E_x &= E_0\cos(kz - kct + \phi), & \hat{E} &= \frac{E_0}{2}e^{i\phi} \\ &= \hat{E}e^{ik(z-ct)} + \hat{E}^*e^{-ik(z-ct)}, & (3.30) \end{aligned}$$

where $\hat{E}$ is a slowly varying complex number. The derivatives are decomposed using

$$\begin{aligned} D_\pm &= \frac{1}{c}\frac{\partial}{\partial t} \pm \frac{\partial}{\partial z} & (3.31) \\ & D_+ e^{\pm ik(z-ct)} = 0, \\ & D_- e^{\pm ik(z-ct)} = \mp 2ike^{\pm ik(z-ct)}, \end{aligned}$$

$$\left(\frac{1}{c}\frac{\partial}{\partial t}\right)^2 - \left(\frac{\partial}{\partial z}\right)^2 = D_+ D_-. \quad (3.32)$$

Making use of the slowly varying nature of $\hat{E}$, $| D_-\hat{E} | \ll k | \hat{E} |$, one can approximate

$$D_-\left[\hat{E}e^{ik(z-ct)}\right] = -2ik\hat{E}e^{ik(z-ct)}. \quad (3.33)$$

This is called the slowly varying phase and amplitude approximation. Additionally there is the exact equality

$$D_+\left[\hat{E}e^{ik(z-ct)}\right] = e^{ik(z-ct)}D_+\hat{E}. \quad (3.34)$$

Combining the equations (3.28)-(3.34) equation 3.27 becomes

$$e^{ik(z-ct)}\left(-2ikD_+ - \nabla_\perp^2\right)\hat{E} \quad (3.35)$$
$$+e^{-ik(z-ct)}\left(2ikD_+ - \nabla_\perp^2\right)\hat{E}^* = -\frac{1}{\varepsilon_0 c^2}\frac{\partial J_x}{\partial t}$$

$$\Rightarrow \left(-2ikD_+ - \nabla_\perp^2\right)\hat{E} \quad (3.36)$$
$$+e^{-2ik(z-ct)}\left(2ikD_+ - \nabla_\perp^2\right)\hat{E}^* = -\frac{1}{\varepsilon_0 c^2}\frac{\partial J_x}{\partial t}e^{-ik(z-ct)}.$$

Instead of treating single electrons one would like to handle continuous quantities. Therefore equation 3.36 is averaged by means of the following integral

$$\frac{1}{\triangle t}\int_t^{t+\triangle t}[\ldots]dt\bigg|_{z=const},$$

over a time interval larger than one period of the oscillation and smaller than the coherence length $\lambda/c \ll \triangle t \ll N_u\lambda/c$. Over this interval $\hat{E}$ can be regarded as constant. In the integral the second term of the left hand side of eq. 3.36 averages out due to its fast oscillation. The averaged equation then reads

$$\left(2ikD_+ + \nabla_\perp^2\right)\hat{E}$$
$$= -\frac{ike\tilde{K}}{\varepsilon_0 c}\frac{1}{\overline{v}_z\triangle t}\cos(k_u z)\sum_{j=1}^{N_e}\frac{1}{\gamma_j}e^{-ik(z-ct_j)}\delta(\vec{x} - \vec{x}_j)$$
$$= -\frac{ike\tilde{K}}{2\varepsilon_0\gamma}n_e < \exp(-i\theta_j) >, \quad (3.37)$$

with the electron line density $n_e = N_e/(\overline{v}_z\triangle t)< \delta(\vec{x} - \vec{x}_j) >$ and $z_j \approx \overline{\beta}ct_j \approx ct_j$.

3.2 Dimensionless FEL Equations

In the following dimensionless equations are derived. First the independent variables are changed from $(z, t) \rightarrow (z, \theta)$ and $\hat{E}(z, t) \rightarrow \tilde{E}(z, \theta)$.

$$\begin{aligned} d\hat{E} &= \frac{\partial\hat{E}}{\partial z}dz + \frac{\partial\hat{E}}{\partial t}dt \\ &= \frac{\partial\tilde{E}}{\partial z}dz + \frac{\partial\tilde{E}}{\partial\theta}d\theta \\ &= \frac{\partial\tilde{E}}{\partial z}dz + \frac{\partial\tilde{E}}{\partial\theta}(k + k_u)dz - \frac{\partial\tilde{E}}{\partial\theta}\omega dt \quad (3.38) \end{aligned}$$

$$\Leftrightarrow \frac{1}{c}\frac{\partial\hat{E}}{\partial t} = -k\frac{\partial\tilde{E}}{\partial\theta}, \quad (3.39)$$

$$\frac{\partial\hat{E}}{\partial z} = (k + k_u)\frac{\partial\tilde{E}}{\partial\theta} + \frac{\partial\tilde{E}}{\partial z} \quad (3.40)$$

Using these variables the equation 3.37 changes into

$$\left(\frac{\partial}{\partial z} + k_u\frac{\partial}{\partial\theta} + \frac{\nabla_\perp^2}{2ik}\right)\tilde{E} = -\frac{en_e\tilde{K}}{4\varepsilon_0\gamma} < \exp(-i\theta_j) > (3.41)$$

In 1D theory the transverse derivative is neglected

$$\left(\frac{\partial}{\partial z} + k_u\frac{\partial}{\partial\theta}\right)\tilde{E} = -\frac{en_e\tilde{K}}{4\varepsilon_0\gamma} < \exp(-i\theta_j) >. \quad (3.42)$$

The pendulum equations become

$$\frac{\mathrm{d}\theta}{\mathrm{d}z} = 2\eta k_u, \quad \frac{\mathrm{d}\eta}{\mathrm{d}z} = \frac{e\tilde{K}}{2\gamma_0^2 mc^2}\left(\tilde{E}e^{i\theta} + \tilde{E}^* e^{-i\theta}\right). \tag{3.43}$$

A fundamental parameter of the FEL is the Pierce parameter ρ [26]. It is defined as follows[1]

$$\rho = \sqrt[3]{\frac{e^2 \tilde{K}^2 n_e}{32\varepsilon_0 \overline{\gamma}^3 mc^2 k_u^2}}, \tag{3.45}$$

The advantage of using the Pierce parameter will become clear when writing down the main characteristics of the FEL at the end of the calculations. The following new variables are introduced

$$z \rightarrow \tilde{z} = 2k_u \rho z, \tag{3.46}$$

$$\eta \rightarrow \tilde{\eta} = \frac{\eta}{\rho}, \tag{3.47}$$

$$\tilde{E} \rightarrow \tilde{a} = \frac{e\tilde{K}}{4\gamma_0^2 k_u mc^2 \rho^2}\tilde{E}. \tag{3.48}$$

In general there will be a detuning between the radiation field and the resonant $\overline{\omega}$. Then it is reasonable to assume that the normalized field is oscillating

$$\tilde{a} \propto \exp(i\nu\theta), \tag{3.49}$$

corresponding to a frequency detuning of the radiation $\nu = (\omega - \overline{\omega})/\overline{\omega}$. The associated normalized detuning is

$$\tilde{\nu} = \frac{\nu}{2\rho}. \tag{3.50}$$

With this set of variables the 1-dimensional FEL equations can be written

$$\frac{\mathrm{d}\theta_j}{\mathrm{d}\tilde{z}} = \tilde{\eta}_j, \tag{3.51}$$

$$\frac{\mathrm{d}\tilde{\eta}_j}{\mathrm{d}\tilde{z}} = \tilde{a}e^{i\theta_j} + \tilde{a}^* e^{-i\theta_j}, \tag{3.52}$$

$$\left(\frac{\partial}{\partial\tilde{z}} + i\tilde{\nu}\right)\tilde{a} = <\exp(-i\theta_j)>. \tag{3.53}$$

The parameter ρ has been chosen such that the coefficient on the right hand side of 3.53 is one. Two collective variables are defined

$$\tilde{b} = <\exp(-i\theta_j)> \quad \text{bunching parameter} \tag{3.54}$$
$$\tilde{P} = <\tilde{\eta}_j \exp(-i\theta_j)> \quad \text{energy modulation} \tag{3.55}$$

[1]Often an alternative formula is given for

$$\rho = \sqrt[3]{\frac{1}{8\pi}\frac{I}{I_A}\left(\frac{\tilde{K}}{1+K^2/2}\right)^2 \frac{\overline{\gamma}\lambda^2}{\Sigma_A}}, \tag{3.44}$$

with $I_A = 17045$ A the Alfvén current, and $\Sigma_A = 2\pi\sigma_x^2$ the cross sectional area of the electron beam.

to ease the notation in the following. In terms of the collective variables the FEL equations read

$$\frac{\mathrm{d}\tilde{b}}{\mathrm{d}\tilde{z}} = -i\tilde{P}, \tag{3.56}$$

$$\frac{\mathrm{d}\tilde{P}}{\mathrm{d}\tilde{z}} = \tilde{a}, \tag{3.57}$$

$$\frac{\mathrm{d}\tilde{a}}{\mathrm{d}\tilde{z}} = -\tilde{b} - i\tilde{\nu}\tilde{a}. \tag{3.58}$$

Equation 3.56 describes the enhancement of microbunching due to the energy modulation of the bunch. Equation 3.57 shows how the energy modulation is caused by the radiation field. Equation 3.58 describes the growth of the radiation power due to microbunching. The second term on the right hand side of equation 3.57 contains the average $< \exp(-i2\theta_j) >$ and averages out. The three
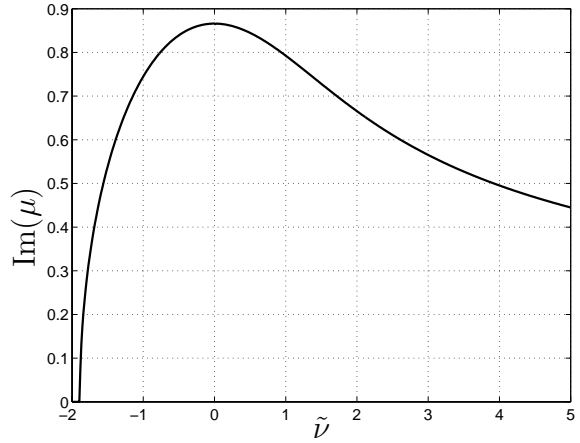

Figure 3.2: Growth rate of the FEL radiation versus normalized detuning $\tilde{\nu} = (\omega - \overline{\omega})/(2\rho\overline{\omega})$.

coupled FEL equations can be solved by the ansatz

$$\tilde{a} = a_0 \exp(i\mu\tilde{z}). \tag{3.59}$$

From equations 3.56-3.58 it follows that

$$\tilde{P} = -\frac{i}{\mu}\tilde{a} \qquad \tilde{b} = \frac{i}{\mu^2}\tilde{a} \qquad i\mu\tilde{a} = -\tilde{b} - i\tilde{\nu}\tilde{a}. \tag{3.60}$$

Therefore the assumed solution (3.59) is only possible if

$$\mu^3 + \tilde{\nu}\mu^2 + 1 = 0. \tag{3.61}$$

There are procedures to solve such a cubic equation [8]. The solution representing the exponential gain of radiation corresponds to $\mathrm{Im}(\mu) < 0$. To find the solution equation 3.61 is transformed into the reduced form

$$\mu \rightarrow \chi = \mu + \tilde{\nu}/3, \tag{3.62}$$

$$\chi^3 \underbrace{-\frac{\tilde{\nu}^2}{3}}_{p}\chi + \underbrace{\frac{2\tilde{\nu}^3}{27} + 1}_{q} = 0. \tag{3.63}$$

19

The required complex solution only exists if $D = (p/3)^3 + (q/2)^2 > 0$

$$\tilde{\nu} > -\frac{3}{\sqrt[3]{4}} \approx -1.89. \qquad (3.64)$$

For zero detuning $\tilde{\nu} = 0$ the solution is

$$\mu_0 = \frac{1}{2} - i\frac{\sqrt{3}}{2}. \qquad (3.65)$$

From numerical calculations (see fig 3.2) it can be seen that this corresponds to the maximum growth rate of FEL radiation. The solution for the exponentially growing part is then

$$\tilde{a}(\tilde{z}) = \frac{1}{3}\left(\tilde{a}(0) + \frac{\tilde{b}(0)}{\mu} - i\tilde{P}(0)\mu\right)e^{-i\mu\tilde{z}}. \quad (3.66)$$

The first term corresponds to coherent amplification, the other two to self amplified spontaneous emission (SASE) generated from random noise on the electron distributions. The above approximations are only valid for $|\tilde{a}| \lesssim 1$. If $|\tilde{a}| \approx 1$ saturation is reached. The radiation power in this case is

$$P = \frac{1}{Z_0}\tilde{E}\tilde{E}^* \approx \frac{1}{2}\rho \underbrace{c\gamma n_e m c^2}_{\text{beam power}}. \quad (3.67)$$

Some conclusions can be drawn [26]:

- The Pierce parameter ρ is a measure for the efficiency of the FEL at saturation.

- From the lower graph of figure 3.3 it can be concluded that the bandwidth of the FEL is $\triangle\omega/\omega \sim \rho$.

- Without detuning the power gain length is approximately $\frac{1}{\text{Im}\mu_0} = \frac{\lambda_u}{4\pi\sqrt{3}\rho}$.

- The saturation length can be estimated to be $L_s \sim \lambda_u/\rho$.

- the coherence length can be estimated from the bandwidth $l_c \sim \lambda\rho$.

An energy loss along the undulator can be simulated by changing the detuning $\tilde{\nu}$ linearly between $\tilde{\nu}_0 \ldots \tilde{\nu}_0 + \tilde{\triangle}$ along the undulator. The effective gain coefficient is then calculated by

$$\mu_{eff} = \frac{1}{\tilde{\triangle}}\int_{\tilde{\nu}_0}^{\tilde{\nu}_0 + \tilde{\triangle}} \mu(\tilde{\nu})d\tilde{\nu}. \qquad (3.68)$$

The figure 3.3 shows the corresponding gain curves for different detuning rates. Note that the detuning is growing positively when the energy is lost.
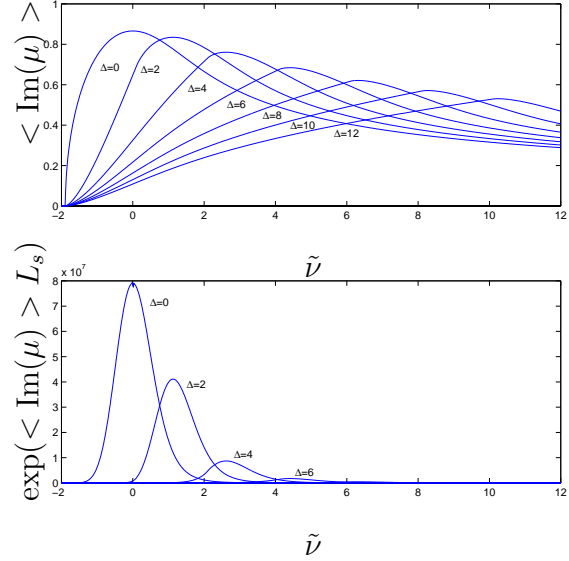

Figure 3.3: Growth rate of the FEL radiation versus normalized detuning assuming a constant energy loss along the undulator. The different curves correspond to a certain change of the detuning along the undulator $\triangle = \tilde{\nu}_{end} - \tilde{\nu}_{in}$. The lower picture shows the corresponding amplification after 21 gain lengths (saturation).

Allowing a maximum detuning of one bandwidth ($\tilde{\triangle} < 1$) results in

$$\frac{d\tilde{\nu}}{dz} \lesssim \frac{1}{L_s} \approx \frac{\rho}{\lambda_u}. \qquad (3.69)$$

Inserting the definition $\tilde{\nu} = \triangle\omega/(2\rho\omega_0)$ and using $\omega \sim \gamma^2$ the condition in absolute coordinates is found

$$\frac{d\gamma}{dz} \lesssim \frac{\rho^2}{\lambda_u}\overline{\gamma}. \qquad (3.70)$$

Similar considerations can be made to calculate the maximum energy gradient on the bunch. During each period of the oscillation the radiation slips ahead by one wavelength. Again along the slippage length the allowed detuning is one bandwidth. The slippage length is $\lambda/\lambda_u \cdot L_s$ and therefore

$$\frac{d\gamma}{d\zeta} \lesssim \frac{\rho^2}{\lambda}\overline{\gamma}, \qquad (3.71)$$

with $\zeta = z - ct$ the distance from the head of the bunch.

3.3 The TTF FEL

In Table 3.1 the main parameters of the TTF-FEL are summarized. From these numbers the Pierce parameter is calculated to be $\rho = 2.5 \cdot 10^{-3}$. From this a power gain length $L_{G,calc} = 50$ cm can be calculated, the measured gain length was

Beam energy	240-250 MeV
Bunch charge	2.7-3.3 nC
Charge in radiative part of bunch	0.1-0.2 nC
Peak current	1.3 ± 0.3 kA
rms energy spread	150 ± 50 keV
rms normalized emittance	$(6 \pm 2)\pi$ mm·mrad
Bunch spacing	0.44/1 μs
Number of bunches in a train	up to 70
rf pulse repetition rate	1 Hz
Undulator period λ_u	2.73 cm
Undulator peak field	0.47 T
Average beta function	1.2 m
Magnetic length of undulator	13.5 m
Radiation wavelength	95-105 nm
Energy in the radiation pulse	30-100 μJ
FWHM radiation pulse duration	50^{+50}_{-20} fs
Radiation peak power level	1 GW
Radiation average power	up to 5 mW
Spectrum width (FWHM)	1%
Spot size at undulator exit (FWHM)	250 μm
Angular divergence (FWHM)	260 μrad

Table 3.1: TABLE I. Main parameters of the TESLA Test Facility for FEL experiments (TTF FEL, phase 1)[3].

$L_{G,meas} = 67 \pm 5cm$. The difference is mainly caused by the energy spread of the bunch. Since many of the FEL parameters are inaccessible to the beam diagnostics, the values in table 3.1 were chosen such that simulation of the FEL is consistent with the measured properties of the radiation pulse
.

Using equation 3.70 the maximum allowable energy loss inside the undulator is $dE/dz < 2.3 \cdot 10^{-4} \cdot E_0 \approx 55$ keV/m. This boundary is also marked in figure 3.4. Note that the surface roughness wake fields are not the only source of energy loss in the undulator. Other sources are resistive wall wake fields [44] and the FEL radiation itself.

In the design phase of the TTF-FEL, beam parameters different from those in table 3.1 were assumed: A bunch length of $\sigma_z = 250$ μm, a normalized emittance $\epsilon_N = 4\pi$mm mrad, and a bunch charge of 1 nC were planned, yielding a peak current I_{peak}=480 A, and the Pierce parameter $\rho = 4 \cdot 10^{-3}$. In this scenario the limit for the energy loss would have been $dE/dz < 160$ keV/m.

The design of the next evolution step of the TTF-FEL (Phase II) foresees a beam energy of 1 GeV, a bunch length $\sigma_z = 50$ μm, a peak current $I_{peak} = 2.4$ kA, and a bunch width $\sigma_x = 67$ μm. The undulator magnets will be the same as for the first phase, only the total length of the undulator will be increased to 30 m. The radiation wavelength will be 6.4 nm. This results in a Pierce parameter $\rho = 1.8 \cdot 10^{-3}$ and a permitted energy loss $dE/dz < 120$ keV/m.

For the TESLA X-FEL several beam lines with different parameters are foreseen [51]. As an example here only a fixed gap undulator with electron beam energy of 25 GeV is treated. The radiation wavelength is 0.85 Å, the undulator period 45 mm. The Pierce parameter is $\rho = 3 \cdot 10^{-4}$, resulting in a permitted energy loss of $dE/dz < 50$ keV/m.
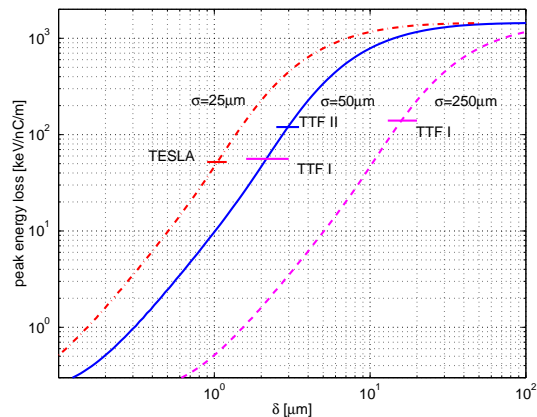

Figure 3.4: Expected peak energy loss due to surface roughness wake fields and permitted energy loss of different FELs. The peak energy loss due to surface roughness wakes is calculated according to the Dohlus model scaling the spectrum of the surface roughness in the wake field experiment.

Chapter 4

Longitudinal Phase Space Tomography

In general the task of computer tomography is to reconstruct a distribution in a space of higher dimension from a set of projections measured in a lower dimensional subspace. In most cases the set of projections is generated by rotation of the object under study. Phase space tomography is an application of this technique to particle beams in accelerators. In the transverse case the phase space is the coordinate system of transverse offset and divergence. The x and y profiles are measurable with observation screens or wire scanners. Therefore the profiles are the natural choice for the projections. The rotation of the phase space can be achieved with a quadrupole doublet. The profiles can be measured via optical transition radiation (OTR) from a metallic screen (see [15]).

The longitudinal phase space is spanned by the energy offset $\mathcal{E}$ and time offset $\mathcal{T}$ with respect to a reference particle. With a magnetic spectrometer the energy profile of the bunches can be measured. Therefore the projections onto the energy axis are the inputs for the reconstruction. By accelerating the bunches at different phases φ of the accelerating rf field it is possible to obtain a distortion of the phase space but not a rotation. In the linear approximation the transformation is a shearing

$$
\begin{pmatrix} \mathcal{E} \\ \mathcal{T} \end{pmatrix}' = \begin{pmatrix} 1 & E_0 \omega \sin \varphi \\ 0 & 1 \end{pmatrix} \begin{pmatrix} \mathcal{E} \\ \mathcal{T} \end{pmatrix}. \tag{4.1}
$$

In this thesis the longitudinal phase space of the bunches in the TTF is considered when they enter the spectrometer at the end of the linac. There is no possibility to project the time profile onto the energy axis and hence no possibility to obtain a full rotation of 180°. This has severe implications for the tomographic reconstruction as will be seen later. In a synchrotron or with a magnetic chicane there are however transformations that allow for a full rotation. See for example [40] or [17] for these cases.
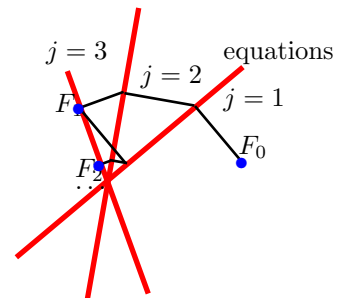

Figure 4.1: Illustration of Kaczmarz's method. By successively performing the projection onto each equation the solution is approached. One iteration is reached when all equations have been considered.

4.1 Algebraic Reconstruction

There are a number of algorithms available to reconstruct the original 2-dimensional distribution from a set of projections. In this context only the ART (algebraic reconstruction technique) algorithm will be explained as an example for a standard reconstruction technique [31]. For the ART algorithm the space is divided into a cartesian grid. The content of each bin in the grid is an element of a single row vector F. The projections are written into a row vector G. The vectors are related by a matrix $\underline{\underline{A}}$

$$
\underline{G} = \underline{\underline{A}} \cdot \underline{F}. \tag{4.2}
$$

In most cases $\underline{\underline{A}}$ will not be a square matrix. Even if the measurement is done such that $\underline{\underline{A}}$ is a square matrix, it will be ill posed. This means that with ideal data from simulation the reconstruction will then yield the original distribution, but already noise in the order of 10^{-3} will cause unacceptable errors in the reconstruction. Therefore an approximation method is used to perform the inversion. The method chosen for the ART algorithm is called Kaczmarz's method. The basic idea of this method is sketched in figure 4.1. Each linear equa-
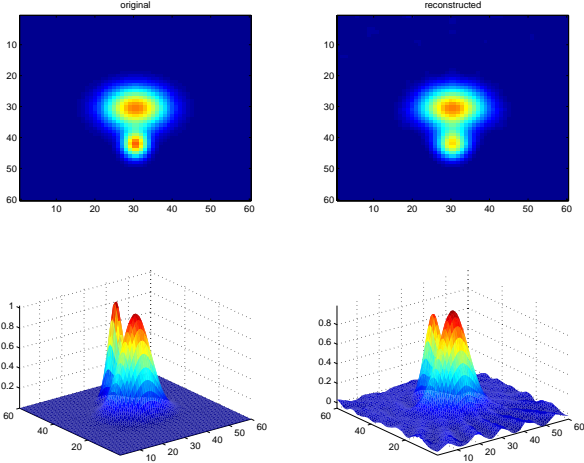
Figure 4.2: Example for the ART algorithm. The left pictures show the assumed distribution. From this distribution the projections are calculated and input into the reconstruction algorithm. The right pictures show the result of the reconstruction. The main features of the distribution are reproduced with good quality. There are some small artefacts with small amplitude. These are due to the small number of 9 projections.

tion can be represented by a straight line in a multidimensional vector space. The solution of the equation system is found at the intersection point of all lines. Starting from an arbitrary point in the vector space the solution can be approximated by successively performing the projection onto the lines.

$$\underline{F}_j = \underline{F}_{j-1} + \frac{\omega}{|\underline{a}_j|^2}\left(g_j - \underline{a}_j^T \underline{F}_{j-1}\right)\underline{a}_j \quad (4.3)$$

$$j = 1 \ldots N$$

with $\underline{a}_j$ being the jth row of $\underline{\underline{A}}$, g_j the jth entry of $\underline{G}$, $\underline{F}_j$ is the jth corrected version of $\underline{F}$ after the jth projection. The parameter ω can be adjusted to control the convergence of the iterations. In general this method can be used to solve a system of linear equations. Here it delivers a good approximation for the projections of the two dimensional distribution (see fig. 4.2).

A common requirement of all standard algorithms is the need for a set of projections covering a full rotation of 180°. The ART algorithm is no exception. Figure 4.3 shows a reconstruction based on a limited set of projection angles. Two main problems are identified. The resolution of the measurement is reduced, i.e. the two peaks which could be separated before now appear as one, and the artefacts are enhanced: Especially streaks at the maximum angles are produced. This problem becomes even more serious for distributions which already have a pronounced structure along this direction. In the longitudinal phase space this has to be expected.
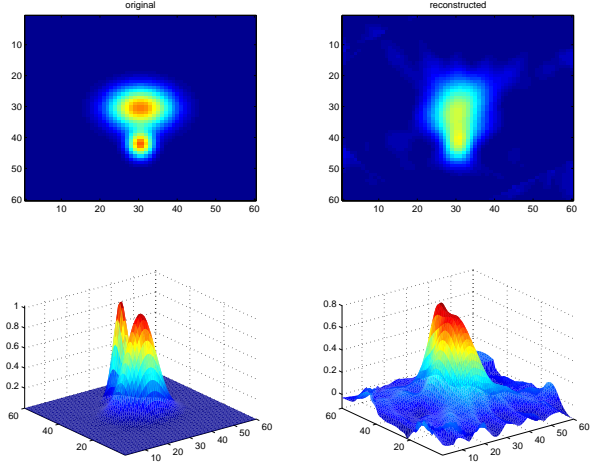

Figure 4.3: The result of the ART algorithm with a reduced set of projections. In comparison to the previous example the angle of rotation has been reduced to 90°. The reconstruction washes out features of the distribution and the artefacts are enhanced.

The analysis of the projections in figure 4.4 shows why all standard algorithms fail to reconstruct the original distribution in the "reduced angle" problem. Although artefacts appear in the two dimensional reconstruction the projections are reproduced very well in terms of a least square fit and no further improvement can be expected. By taking the projections alone the reconstruction algorithm very likely only finds a relative minimum of the error minimization resulting in severe artefacts.

There are some possible directions in which one might look for a cure. The artefacts in the reconstruction seem to be predictable. The number of wiggles in the distribution is given by the number of projections and the strongest artefacts are in the direction of the maximum projection angle. Therefore a spatial filter might improve the reconstruction by deconvoluting the predicted pattern from the distribution.

The main contribution of the artefacts appear at low amplitudes of the projection signal. A nonlinear weight of the deviations might improve the reconstruction, the logarithmic function seems to be a good candidate for that. The third idea is the maximum entropy method explained in the next section. The ART algorithm will not be used any further in this work.

4.2   Maximum Entropy Algorithm

The maximum entropy method is a general technique for data analysis. It provides procedures based on the least possible prejudice on the mea-
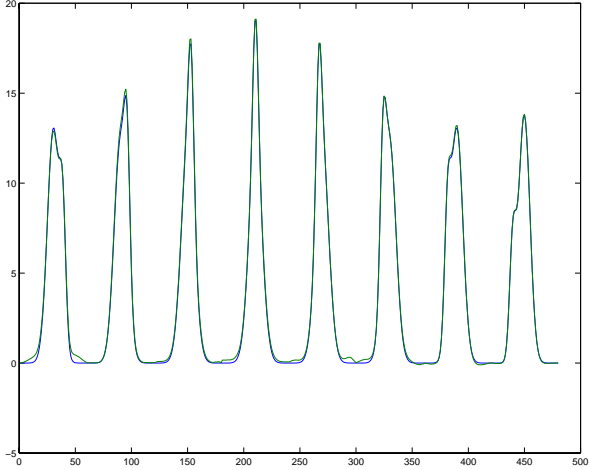
Figure 4.4: Input data for the ART algorithm. The original and the reconstructed projections are shown. They are put on top of each other and hardly any difference can be seen. Only small deviations can be seen just above the baseline.
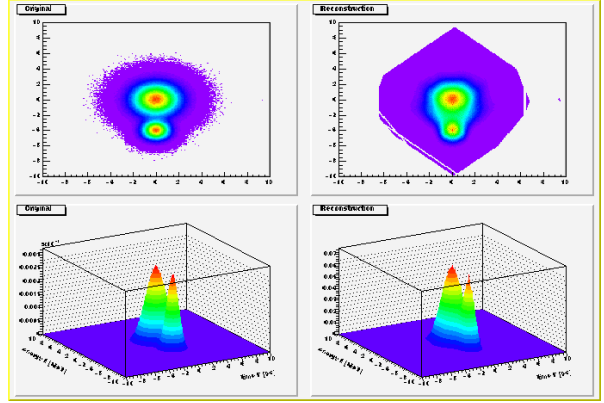

Figure 4.5: Simulated reconstruction with the MENT (maximum entropy) algorithm. On the left an assumed distribution is shown. From this distribution the projections are calculated and fed into the algorithm. On the right the corresponding reconstruction is shown. No severe artefacts are observed, the resolution is as good as can be expected from purely geometrical arguments (see section 4.2.2). For this example 7 projections with a maximum angle of $\pm 45°$ were used.

surement errors.

In the case of phase space tomography, the maximum entropy method can be utilized to reduce artefacts in the reconstructed distribution. The entropy can be interpreted as a measure for the amount of substructures in the distribution. The entropy is maximum for the distribution with the least structure. If there are no constraints this would result in a uniform distribution.

Interpreting the distribution as a collection of particles the entropy has a second interpretation. If there is no further knowledge about the system each arrangement of particles in phase space will be assigned the same probability (least prejudice). The density function f is a global description of the distribution and does not distinguish the microscopic details of the arrangement of particles. Therefore it is possible to calculate for each density function f the number of particle arrangements to reproduce it. A measure for this number is the entropy of this density function. Then it is immediately clear that the density function with the largest entropy has the largest probability to be realized.

For the phase space tomography the task is to maximize the entropy while at the same time the projections are reproduced. These are the constraints for the optimization problem. The procedure is first described for the general case of a rotational transformation of the phase space. Later it can be generalized for non-linear transformations. The algorithm described here was developed by G. Minerbo [30]. A description is also found in [11]. See figure 4.5 for an example of this algorithm. A comparison with figure 4.3 shows that the maximum entropy method is far superior to the al-

gebraic reconstruction technique if only a limited angular range is accessible to the measurement.

Let the original distribution $\mathcal{F}$ be defined in the (x, y)-plane. A number of J projections is taken, the projection number j consisting of $M(j)$ bins with the content G_{jm}. For each projection let s be the axis in the projection plane and t the axis perpendicular to it. The projection data are written as

$$G_{jm} = \int_{s_{jm}}^{s_{jm+1}} ds \int_{-\infty}^{\infty} dt \mathcal{F}(s\cos\theta_j - t\sin\theta_j, s\sin\theta_j + t\cos\theta_j),$$

$$m = 1, \dots, M(j), \qquad j = 1, \dots, J, \qquad (4.4)$$

where $\theta_1, \dots \theta_j, \dots, \theta_J$ are the projection angles, and

$$s_{j1} < s_{j2} < \dots < s_{jM(j)} \qquad (4.5)$$

are a set of abscissas for the jth view. They neither have to be equally spaced nor have they to be the same for all projections. It is assumed that the distribution is confined in a limited area $\mathcal{D}$ and that the s_j cover the whole range of the distribution.

The integral 4.4 can be rewritten by introducing the characteristic function χ_{jm} of the interval $[s_{jm}, s_{jm+1})$

$$\chi_{jm}(s) = \begin{cases} 1, & s_{jm} \leq s < s_{jm+1}, \\ 0, & \text{otherwise.} \end{cases} \qquad (4.6)$$

In this way the integration can be extended across the whole area $\mathcal{D}$

$$G_{jm} = \iint_{\mathcal{D}} dx\, dy\, \mathcal{F}(x, y)\chi_{jm}(x\cos\theta_j + y\sin\theta_j).$$

The original distribution $\mathcal{F}$ is of course unknown. Therefore in the calculations it is replaced by the reconstructed distribution f which is iteratively improved starting from a uniform distribution

$$G_{jm} = \iint_{\mathcal{D}} dx\,dy\, f(x,y)\chi_{jm}(x\cos\theta_j + y\sin\theta_j). \quad (4.7)$$

The distribution f can be treated as a probability distribution. The entropy is defined as

$$\eta(f) = -\iint_{\mathcal{D}} dx\,dy f(x,y)\ln[f(x,y)A], \quad (4.8)$$

where A is the area of the domain $\mathcal{D}$. It can be shown that η is proportional to the logarithm of the probability of the distribution f [14, 22]. The task is now to find the maximum of η subject to the constraints in eq. 4.7.

This is a variational problem. To find the solution Lagrange multipliers Λ_{jm} are introduced, one for each constraint 4.4. Then the Lagrangian is formed [8]

$$\Psi(f,\Lambda) = f(x,y)\ln[f(x,y)A] \quad (4.9)$$
$$+ \sum_j \sum_m \Lambda_{jm}\left[G_{jm} - f(x,y)\chi_{jm}(x\cos\theta_j + y\sin\theta_j)\right].$$

The functional derivative of Ψ with respect to f is set equal to zero,

$$\frac{\partial\Psi}{\partial f} = 0 \quad (4.10)$$
$$= \ln[f(x,y)A] + 1 - \sum_j \sum_m \Lambda_{jm}\chi_{jm}(x\cos\theta_j + y\sin\theta_j).$$

This is the Euler-Lagrange equation for this problem.

$$\Leftrightarrow f(x,y) = \frac{1}{Ae}\prod_j\prod_m \exp[\Lambda_{jm}\chi_{jm}(x\cos\theta_j + y\sin\theta_j)]$$
$$\Leftrightarrow f(x,y) = \frac{1}{A}\prod_j\prod_m H_{jm}^{\chi_{jm}(x\cos\theta_j + y\sin\theta_j)}, \quad (4.11)$$

with $H_{jm} = \exp(\Lambda_{jm} - 1/J)$. The χ_{jm} can be zero or one. Therefore the H_{jm} contribute to the product as H_{jm}^0 or H_{jm}^1. For given (x,y) only one H_{jm} contributes. Therefore the product can be replaced by a sum

$$f(x,y) = \frac{1}{A}\prod_j\sum_m H_{jm}\chi_{jm}(x\cos\theta_j + y\sin\theta_j). \quad (4.12)$$

The optimization problem is solved by finding the Λ_{jm} respectively the H_{jm}.

The coefficients H_{jm} are determined by substituting eq. 4.12 into eq. 4.4

$$G_{jm} = \frac{1}{A}\iint_{\mathcal{D}} dx\,dy \prod_k \sum_n H_{kn}\chi_{kn}(x\cos\theta_{jk} - y\sin\theta_{jk}), \quad (4.13)$$

where $\theta_{jk} = \theta_j - \theta_k$. The non-linear Gauss-Seidel method is used to solve this system of equations.

The H_{jm}^0 are initialized with 1. If $G_{jm} = 0$, the corresponding H_{jm} are set equal zero and eliminated as an active variable. The solution is found by recursively applying

$$H_{jm}^{i+1} = \frac{AG_{jm}H_{jm}^i}{\iint_{\mathcal{D}} dx\,dy \prod_k \sum_n H_{kn}^i\chi_{kn}(x\cos\theta_{jk} - y\sin\theta_{jk})}. \quad (4.14)$$

The integrand is piecewise constant over polygons. Thus the double integral can be performed exactly in a finite number of steps. Due to the introduction of the characteristic function it is not necessary to calculate any logarithm or exponential function.

4.2.1 The Implementation

As mentioned above the integrand is constant over polygons. So the task for the implementation is to find the correct polygons. Every polygon can be made from a set of triangles. The initial division of the space is made up by the bins of the respective projection. These rectangles are divided into a set of triangles. If only linear transformations have to be expected, two triangles are sufficient. This is the case for the transverse phase space. In the longitudinal phase space the curvature of the rf has to be accounted for. The easiest way to do so is dividing the bins into smaller rectangles over which the transformation can be regarded as linear. The rectangles are then cut into two halves to obtain again triangles.

The triangles are then fed into a recursive function which maps the corner points of the triangle to the initial grid in front of the transformation and maps it again to a new projection. In this way non-linear transformations can be perfomed as well. In the transformed grid the intersections with the new bins are calculated and the triangles are divided accordingly. This function calls itself recursively until either all projections have been processed or the triangle leaves the valid space. The area of the final triangle is multiplied with the corresponding H_{jm} and the added to the total sum.

4.2.2 Limits of Applicability

The off-crest acceleration induces a distortion of the longitudinal phase space, which in first order can be described as a shearing

$$\triangle\mathcal{E} = a \cdot \triangle\mathcal{T}, \quad (4.15)$$
$$a = E_0\omega_0\sin\varphi_{off}.$$

Assuming a phase shift $\varphi_{off} = \pm 45°$ and a energy gain $E_0 = 110$ MeV,

$$a = \frac{\triangle E}{\triangle t} \approx 570 \text{ keV/ps} \quad (4.16)$$
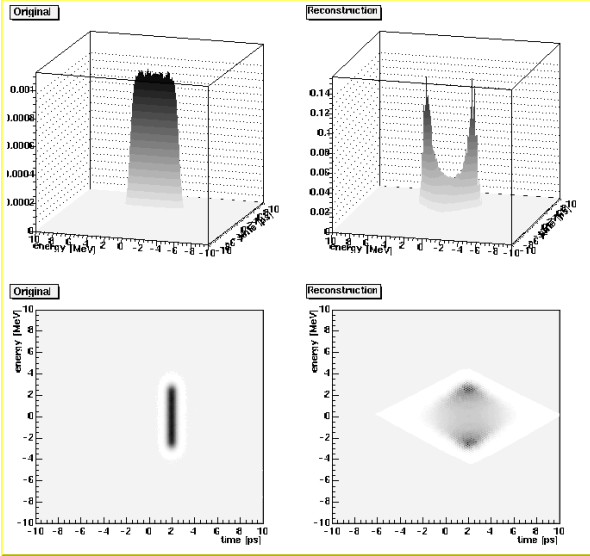
Figure 4.6: The resolution that can be achieved by a tomography performed with a set of limited angles. The left pictures show an assumed distribution which is very narrow in time while the right picture shows a reconstructed distribution. The best time resolution is achieved at the edges of the distribution. Towards the center of the distribution $\triangle\mathcal{E}$ increases and so does $\triangle\mathcal{T}$. Here it may be deduced from the inverse of the height of the maximum. Note: If the bin size would have been adapted to the time resolution the reconstructed distribution would show the same rectangular shape as the original.

Two peaks in the phase space separated by $\triangle\mathcal{T}$ are shifted by $a \cdot \triangle\mathcal{T}$ against each other in energy. At the same time the peaks are widened. For gaussian peaks with $\sigma_\mathcal{E}$ and $\sigma_\mathcal{T}$ this can be expressed as

$$\sigma'_\mathcal{E} = \sqrt{\sigma_\mathcal{E}^2 + a^2 \sigma_\mathcal{T}^2}. \qquad (4.17)$$

This results in a degradation of the time resolution because in the projection it is impossible to achieve the same separation of the peaks in the energy projection as it would be possible in the time projection (this can be seen in figure 4.6). The energy resolution of the spectrometer depends on the transverse emittance of the beam, the β-function, and the dispersion at the location of the diagnostic screen. The β-function at the OTR screen in the spectrometer is smaller than $0.5\,m$, the dispersion is $1\,m$. At 200 MeV and a normalized emittance $\epsilon_N = 3\,\pi$ mm mrad (slice) one expects

$$\sigma_x = \sqrt{\beta\varepsilon} \approx 62\,\mu m \Rightarrow \sigma_\mathcal{E} \approx 12\,\text{keV} \qquad (4.18)$$

In the experiment a resolution of

$$\sigma_\mathcal{E} \approx 25\,\text{keV} \qquad (4.19)$$

could be verified, probably dominated by the energy spread of the beam itself. Two δ-peaks can be distinguished when they are separated by 2σ

$$\triangle\mathcal{T} = 2\frac{\sigma_\mathcal{E}}{a} \approx 85 \text{ fs.} \qquad (4.20)$$

For extended structures a degradation of the time resolution is expected. Two gaussian peaks with width $\sigma_\mathcal{T}$ can be separated if

$$\triangle\mathcal{T} = 2\sqrt{\frac{\sigma_\mathcal{E}^2}{a^2} + \sigma_\mathcal{T}^2} \qquad (4.21)$$

In general the achievable resolution depends on the structure of the distribution under study. Structures in time can be resolved if there is at least one projection that delivers sufficient separation in energy. Thus the resolution depends on the mean gradient of the distribution along the energy coordinate. It should be stressed that this limitation is derived from geometric arguments only, there is little additional influence from the MENT algorithm. The real distribution may be narrower than the reconstructed one but from the available energy projections it is not justified to assume any narrower distribution unless there is some additional information.
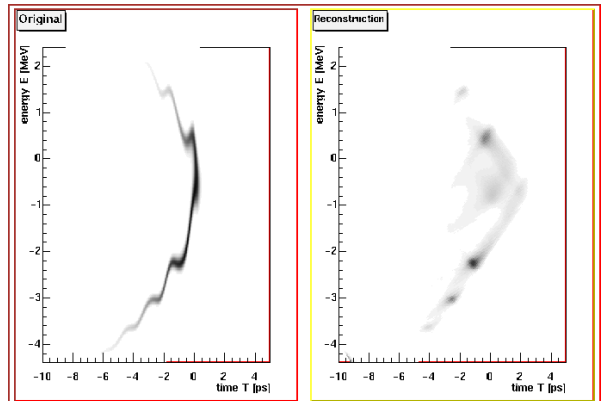

Figure 4.7: Reconstruction of a bunch as expected during the wake field experiment. On the left the simulated bunch is depicted, on the right the tomographic reconstrution is shown. The horizontal axis is the time in ps, the vertical axis the energy in MeV. The head of the bunch is to the right. The projections used in this example are plotted in figure 4.8, the corresponding projection angles can be found in figure 4.12.

The limitations of the tomography can be seen also in the reconstruction of the longitudinal phase space distribution that is expected in the TTF (see also chapter 5). Figure 4.7 shows a simulated distribution with a bunch at maximum compression and synchronous mode wake fields imposed on it. The structures parallel to the energy axis are much better resolved than the structures orthogonal to it. This results in an ensemble of separated peaks in the reconstruction although the original distribution is continuous. The projection data and the
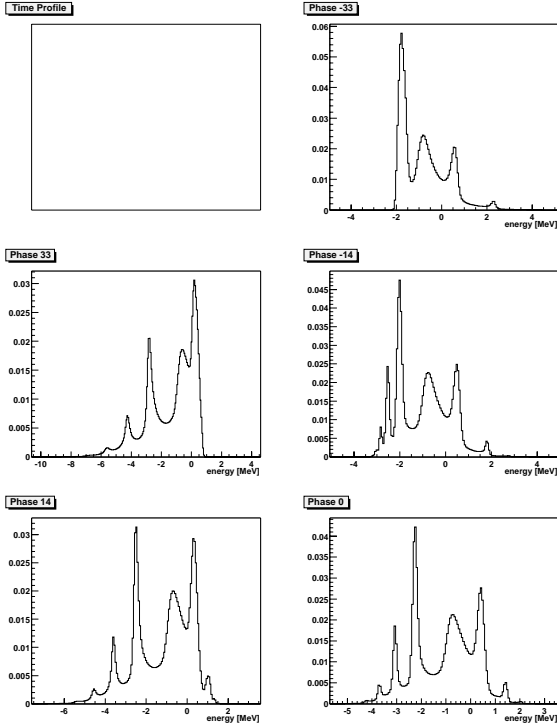
Figure 4.8: Projections used for the reconstruction in figure 4.7. The top left graph without content is a place holder for the missing time profile. The other graphs are marked with the corresponding off-crest rf phase. The corresponding projection angles can be found in fig. 4.12. The profiles are produced by both the original and reconstructed phase space distribution.

corresponding projection angles can be found in the figures 4.8 resp. 4.12.

4.2.3 Combining Independent Sources of Information

To overcome the problems explained in the last section it may be useful to combine data from different sources. Here it is appropriate to supplement the energy spectra with a time spectrum derived from an independent interferometric measurement. A difficulty is that the relative time offset of the measured distributions is usually unknown. Therefore the directly measured time profile may be shifted with respect to the time profile reconstructed from the energy distributions. Figure 4.9 shows the result of a combination of simulated projections. The procedure of reconstruction is such that first a tomography is performed without the time profile yielding the distribution in figure 4.7. The reconstructed time profile and the directly measured time profile are then matched such that the points of maximum weight coincide in time. In the case of the distribution in figure 4.9 the offset was only ≈200 fs.

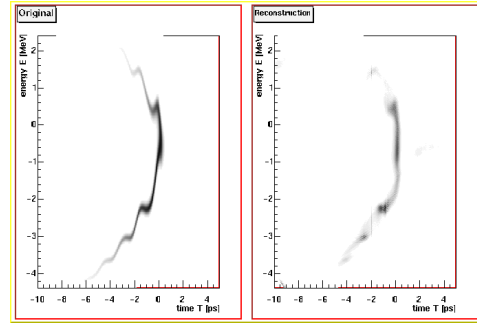The complete set of projections is shown in figure 4.11.

Figure 4.9: Reconstruction of the bunch from figure 4.7. In this case the longitudinal profile of the bunch has been added to the projection data. The origin of the coordinates has been aligned by matching the points of maximum weight of the longitudinal profile and the reconstruction without. See the projections in figure 4.11.
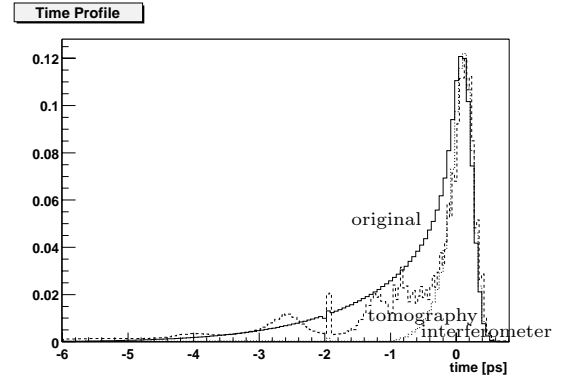

Figure 4.10: Reconstruction of the bunch from figure 4.7. The bunch is moving to the right. The reconstructed profile (dashed line) closer follows the original profile (solid line) than the interferometer data (dotted line).

The frequency response of the time measurement is generally different than that of the energy measurement. Especially when using interferometric data this may be the case, since the interferometer suffers from low frequency cut-offs. In the simulation this is modelled by a low frequency cut-off filter. Afterwards the low frequency amplitudes are enhanced to ensure positive values in the bunch shape. This is necessary because the tomography algorithm requires non-negative projection data. Additionally there is some uncertainty about the real profile since the phase information of the form factor cannot be measured directly but has to be deduced with the aid of the Kramers-Kronig-relation.

The figure 4.10 shows the results for the time profile. The simulated interferometer data produce a very narrow bunch profile. Even with this narrow profile the combined tomography is able to reproduce the original profile which is considerably longer. This is due to the fortunate situation that

As can be seen from figure 4.9 as well as from figure 4.10 the reconstruction of the phase space still does not fit the original completely. This can be traced back to the fact that there is still a gap in the set of projection angles.
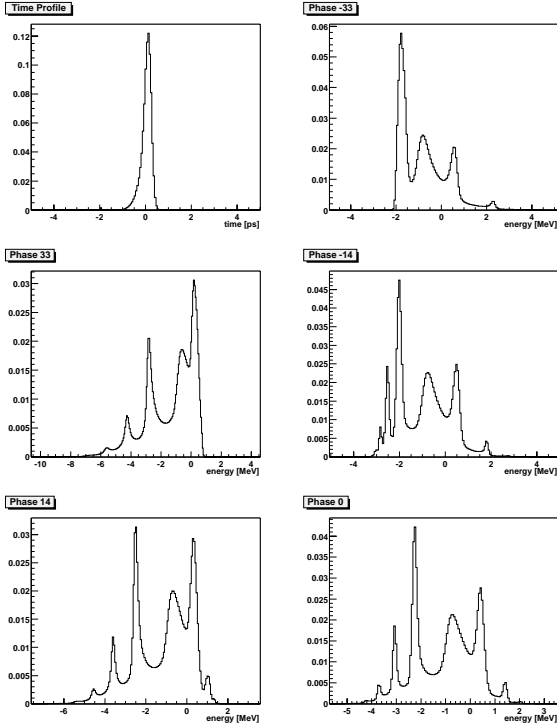

Figure 4.11: Projections used for the reconstruction in figure 4.9. The top left graph shows the time profile, which is distorted by a low frequency cut-off in the interferometer. The other graphs are marked with the corresponding off-crest rf phase, see figure 4.12 for the corresponding projection angles.
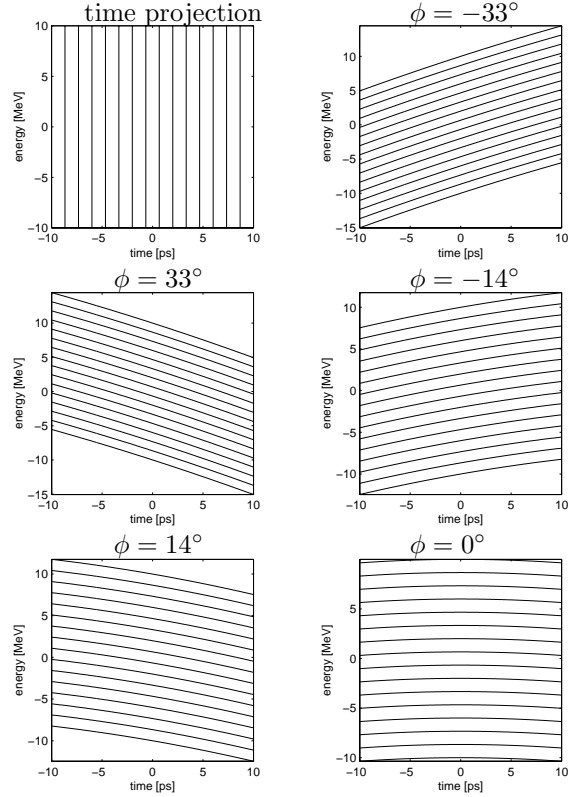
Figure 4.12: Sketch of the projection angles used in figure 4.7 and 4.9. The lines in the phase space are parallel to the paths of integration. The projection angles are plotted in the same order as the profiles in the figures 4.8 and 4.11.

the energy measurements and the interferometer are complementary to each other. The short bunch head is resolved by the interferometric measurement while the long tail of the bunch is well reproduced in the energy profiles. This situation holds as long as none of the projections explicitly excludes parts of the distribution by delivering zero or negative values.

Chapter 5

The TESLA Test Facility Linac

The TESLA Test Facility Linac is a superconducting linear accelerator for electrons. The radio frequency (rf) of the nine-cell cavities is 1.3 GHz. Since the machine serves as a test facility for the TESLA collider its setup is subject to changes. Here the setup will be described as it was used during the wake field experiment.

While a maximum electron energy of approximately 340 MeV can be reached, the nominal working point is about 235 MeV. The electron bunches are produced by photoemission from a Cs_2Te photocathode. Ultraviolet light pulses are required for the photoemission. They are produced by frequency quadrupling the light from a mode-locked Nd:YLF laser. The light pulses have an approximately gaussian shape with $\sigma_t \approx 8.5$ ps. The photocathode is mounted inside a normal conducting rf cavity operating with a peak field of 35 MV/m. This provides immediate acceleration of the electrons and thus a quick compensation of the repulsive Coulomb forces by attractive magnetic forces. Additional focusing is provided by a solenoid field inside the cavity. The strength of the solenoid coils and the acceleration phase of the rf gun are adjusted to optimize the longitudinal and transverse emittances. For optimum conditions the normalized emittance is $\epsilon_N = 3.0 \pm 0.2$ mm mrad [37] and the rms bunch length is $\sigma_z = 3.2 \pm 0.2$ mm (10.7 ± 0.7 ps) [18, 46].

Approximately 1 m behind the gun the first superconducting acceleration cavity boosts the electron energy to 16.7 MeV. A beam line follows with several quadrupoles and diagnostic screens used to measure the transverse emittance, and a spectrometer dipole to analyse the energy distribution. Due to the nonlinear curvature of the accelerating field in the gun and the booster cavity the bunches acquire an energy modulation of 500 keV (rms). The residual energy spread is measured to be 25 keV (rms). That is the energy width of each temporal slice in the longitudinal phase space which cannot be compensated by any time dependent energy modulation. It is dominated by dynamic effects during the acceleration in the gun, presumably the initial energy spread of the electrons leaving the cathode is much smaller (in the order of eV). The measured value is close to the resolution of the spectrometer in the first section[1]. The beam dynamics in the gun have been simulated with comparable results [45]. Other simulations, however, yield considerably smaller values [36].

The beam passes then a first module consisting of eight superconducting cavities, followed by a magnetic chicane for bunch compression. The acceleration voltage of the module is approximately 110 MV. By adjusting the rf phase in the first module a time to energy correlation is imposed on the bunch. The path length in the bunch compressor depends linearly on the particle momentum, $\triangle z/l = -\alpha_c \triangle p/p$, $l\alpha_c = 0.227$ m (see figure 5.2). In combination with the off crest acceleration this

---

[1]In the meantime the resolution of the measurement system has been improved. Newer measurements of the energy spread yield numbers below 5 keV (rms). These results could not be included in this work. The main results, however, are not affected.
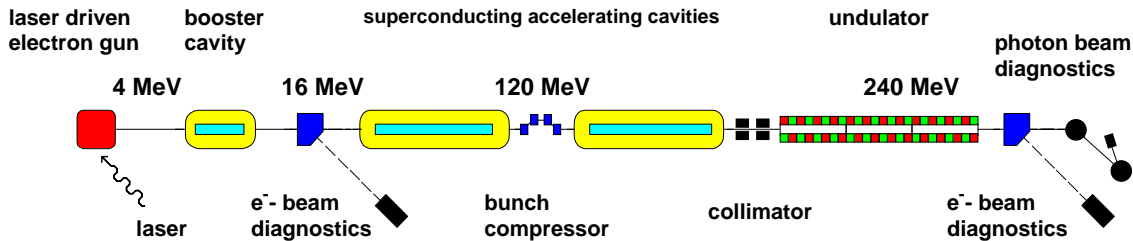

Figure 5.1: Schematic layout of the TESLA Test Facility (TTF). Although separated by the bunch compressor the two modules with superconducting accelerating cavities are driven by a single klystron.
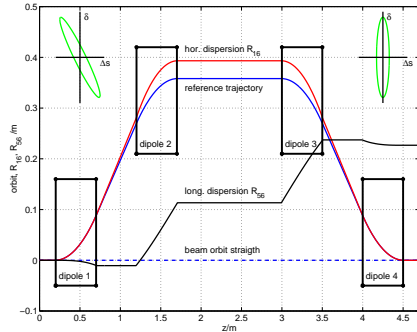
Figure 5.2: Schematic of the bunch compressor [45]. The longitudinal and transverse dispersion functions are plotted as function of the position in the bunch compressor. The momentum compaction is $\alpha_c = R_{56}/l$.

can be used for bunch compression. The optimum longitudinal compression by about a factor of 5 is achieved with an off-crest phase of $\phi = 12°$. Choosing different phases the bunches can be shaped to be more suitable for the wake field experiment. At a later point this will be explained in more detail.

In the bunch compressor and in the spectrometer dipole synchrotron radiation is produced. The radiated spectrum ranges from the cut-off of the beam pipes in the cm-wave regime up to ultraviolet light. Wavelengths comparable to the bunch length or longer are radiated coherently (coherent synchrotron radiation, CSR). By shortening the bunches the coherent part of the spectrum is expanded towards higher frequencies and the total power is increased dramatically. Due to the curved trajectory of the beam in the magnetic chicane the radiation emitted at one point can interact with the beam at another point. Similar to wake fields this will lead to a modulation of the energy distribution of the bunch. But unlike wake fields CSR acts ahead of the source particle. The energy shift of the electrons due to CSR is proportional to the differentiated charge distribution, therefore it is most effective at the head of the bunch where the steepest charge density gradients can occur.

Behind the bunch compressor the second acceleration module raises the electron energy to the final value. During the experiment the maximum energy was 235 MeV. Owing to a shortage of equipment the two acceleration modules are driven by only one klystron. To maintain the stability of the beam parameters at the entrance of the bunch compressor the rf control only stabilizes the first module. The second module receives the same input rf power as the first. The accelerating field depends on the dynamic response of the cavity resonators to the rf input, which in turn depends on the detuning and quality factor of the resonators. The cavity input couplers and the waveguide tuners have been ad-

justed to obtain the same quality factors for all 16 cavities within a range of 5%. The frequencies of the cavities are adjusted with an accuracy of ± 50 Hz. The field stability in the second module can only be maintained within 1% while it is better than 10^{-3} in the first module. The reason for these rather large variations may be cavity detuning due to mechanical vibrations (microphonics).
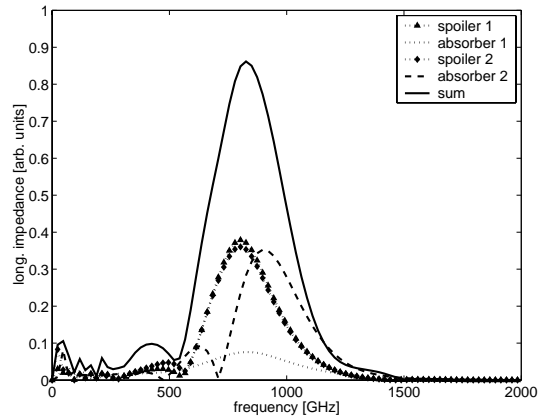

Figure 5.3: Frequency dependence of the impedance of the collimation system. The varying radii of the collimator elements have been considered. The sum of all components yields one resonant frequency at 830 GHz. The assumed effective dielectric constant is $\varepsilon = 1.55$.

The main components of the free electron laser are three undulator modules with an upstream collimation system. The task of the collimator is to protect the permanent magnets of the undulator from radiation damage caused by beam halo. Two stages of collimation with 90° betatron phase advance in between are used. Each stage consists of a so called spoiler with narrow aperture (minimum diameter 6 mm, see figure 5.4) and an absorber of wider aperture which removes secondary particles created in the spoilers. The production of geometrical wakes at these structures has been reduced by tapering the structures. The holes were made by electro-erosion, the surface roughness is considerably larger than in extruded tubes. In the spoilers a roughness of 5 μm (rms) was measured, on the absorbers 3 μm (rms) [43]. Therefore it is expected that surface roughness wake fields are excited. For the calculation of the wake frequencies the tapered structures of the collimators have to be taken into account. The longitudinal impedance can be determined by integrating the wake functions excited by each part of the collimator with the correct phase

$$\phi(z) = \int_z^L (k_z(z') - k)dz'$$

$$Z_\parallel^{tot}(k) = \int_0^L dz \frac{Z_0}{\pi[b(z)]^2} \exp(-i\phi(z)). \quad (5.1)$$

The figure 5.3 shows the resulting impedance of the collimator assuming an effective dielectric constant $\varepsilon = 1.55$ to model the surface roughness wake fields. This value has been chosen to reproduce the measured resonant frequency of 830 GHz (see chapter 7).
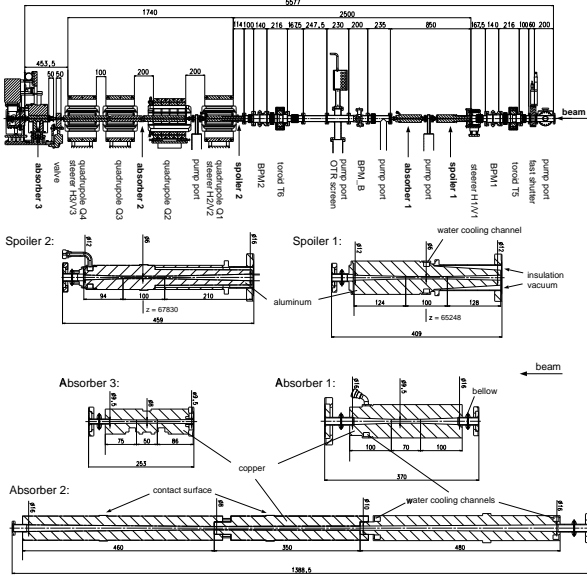

Figure 5.4: Side view of the collimator and cross sections of the spoilers and absorbers [45].

The aluminum undulator vacuum chamber was made by extrusion. The inner diameter of the beam pipe is 9.5 mm. There are some wake fields to be expected from this structure as well. Especially the integrated effect may be strong given a total length of 15 m. The main contributions to the expected wake fields are caused by the resistivity and the roughness of the vacuum chamber. The surface roughness in the undulator is measured to be 600 nm (rms) [16], so the harmonic wake occurs at a frequencies between $1.6 - 5$ THz, depending on the model. Therefore the roughness wake from the undulator like the resistive wall wake influences mainly the head of the bunch. In the wake field experiment these wakes are disregarded by measuring only in the tail of the bunch.

The setup for the wake field experiment is mounted behind the undulator. It consists of a set of test pipes with varying surface treatment and radius. By means of a linear drive the different beam pipes can be introduced into the beam axis. The length of the beam pipes is 855 mm. The radii vary from 3 mm to 5 mm. One meter downstream the test pipe chamber there is a movable screen made of two polished silicon wafers with an aluminum coating acting as a mirror. A special holder allows the use as a closed mirror or with a central slit of up to 10 mm width. This screen can be utilized to

deflect radiation out of the vacuum chamber into a far infrared interferometer. At the end of the linac there is a spectrometer dipole to analyze the energy distribution of the bunches. A screen behind the dipole is used to take images of the energy distribution. Observing the 25 keV energy spread already known from the injector it could be verified that the resolution obtained in this spectrometer is better than 10^{-4}. This spectrometer is used to measure the wake field induced energy modulation of the bunches.

5.1 Simulation of the Longitudinal Phase Space

A computer code has been developed to simulate the longitudinal phase space starting from the entrance of the first accelerating module to the spectrometer. The effects of various accelerator components on the phase space are analyzed by analytical expressions. To ease the calculation of projections the phase space at the end of the linac is represented on a cartesian grid. A matrix is prepared which contains the entries for the charge density. A second matrix contains the corresponding coordinates of the bins. Instead of shifting the contents of the density matrix according to the transformations along the linac, the coordinate matrix is transformed. The components of the linac are treated in backward direction, i.e. the physically last component is treated first. The density matrix then is filled with values calculated by an analytical expression for the charge density calculated as a function of the transformed coordinates $\mathcal{E}$ and t.

The method works if it can be guaranteed that the area of the bins is not changed during the transformations. For linear operations such as rotation and shearing this is immediately clear. For nonlinear operations such as cosine modulations this could be verified as well (see figure 5.5). Note that the transformations required in the simulation act only on one coordinate at a time.

The initial phase space distribution is assumed to be slightly non-gaussian. The following distribution agrees within the errors with the measured bunch
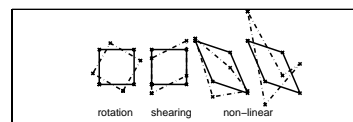

Figure 5.5: A few examples for the transformations of bins. The nonlinear transformations are exaggerated. In all cases the area of the bins is invariant.

length and energy profiles

$$\rho = \rho_0 \exp\left(-\frac{\mathcal{E}^2}{2\sigma_e^2}\right) \cdot \exp\left(-\frac{|t|^{2.5}}{2\sigma_t^{2.5}}\right). \quad (5.2)$$

Here $\mathcal{E}$ and t are the energy resp. time offsets from the reference point in the phase space, $\sigma_e =$25 keV, and $\sigma_t =$10.7 ps [45, 46]. Due to their large length the bunches acquire an energy modulation from the rf curvature of the accelerating field (see figure 5.6)

$$\triangle\mathcal{E} \quad = \quad E_0\left(\cos(\omega_{rf}t - \phi_0) - \cos(\phi_0)\right). \ (5.3)$$

In the bunch compressor the particles travel on different trajectories depending on their energy. This induces a longitudinal dispersion

$$\triangle t \quad = \quad \frac{l\alpha_c}{c}\mathcal{E}, \qquad (5.4)$$

which, in combination with the off-crest acceleration in the first module, leads to a shortening of the bunches (see figure 5.7).

With shorter bunch length the effects of coherent synchrotron radiation have to be taken into account. Due to the curved trajectory in the dipole magnets the synchrotron radiation moves ahead of the source particle. The influence of CSR on the beam energy can be expressed by [42]

$$\frac{d\mathcal{E}}{dz} = -\frac{qe}{2\pi\varepsilon_0(3c)^{1/3}\rho^{2/3}} \int_{-\infty}^{t} \frac{dt'}{(t-t')^{1/3}} \frac{\partial\lambda(t')}{\partial t'}, \quad (5.5)$$

with λ the normalized line charge density of the bunch charge. The main contribution to the CSR effects has to be expected from the third and fourth dipole of the bunch compressor and the spectrometer dipole. The bunches have been treated as if they were already fully compressed when entering the third dipole of the bunch compressor. The effect of CSR in the spectrometer dipole cannot fully be seen in the spectrometer because the electrons have already passed a certain distance in the dipole before they change their energy. The effective length has been approximated by half of the real length. The corresponding simulation results are shown in figure 5.8.

In the second module the bunches are normally accelerated on crest. During the wake field experiment the rf phase of the second module was changed in two ways. For the energy profile measurements the phase was adjusted for maximum contrast of the peak structure, see chapter 7 for more details. A phase of 14° turned out to be the most suitable value. During the tomography measurements the phase was shifted in sequences between $-35°\ldots35°$. The phase shifter would have allowed $\pm45°$ but the beam transport becomes less efficient towards larger off crest phases.

The surface roughness of the collimator beam pipes is of the same order of magnitude as the roughness in the test pipes of the wake field experiment (5 μm on the spoilers, 10 μm in the test pipes). In both cases a harmonic wake is expected

$$\triangle x_e \quad = \quad W_0\cos(\omega_0 x_t)\exp(-x_t/\tau). \quad (5.6)$$

Because the resonant frequency of the wake is a priori unknown it has been derived from the experimental data for both the collimator and the wake field experiment. Similarly the time constants of the wakes have been adjusted to reproduce the experimental data. The figure 5.9 shows the simulated phase space after passage of the 4 mm reference pipe resp. the 4 mm sandblasted pipe. The summary of parameters can be found at the end of chapter 7.
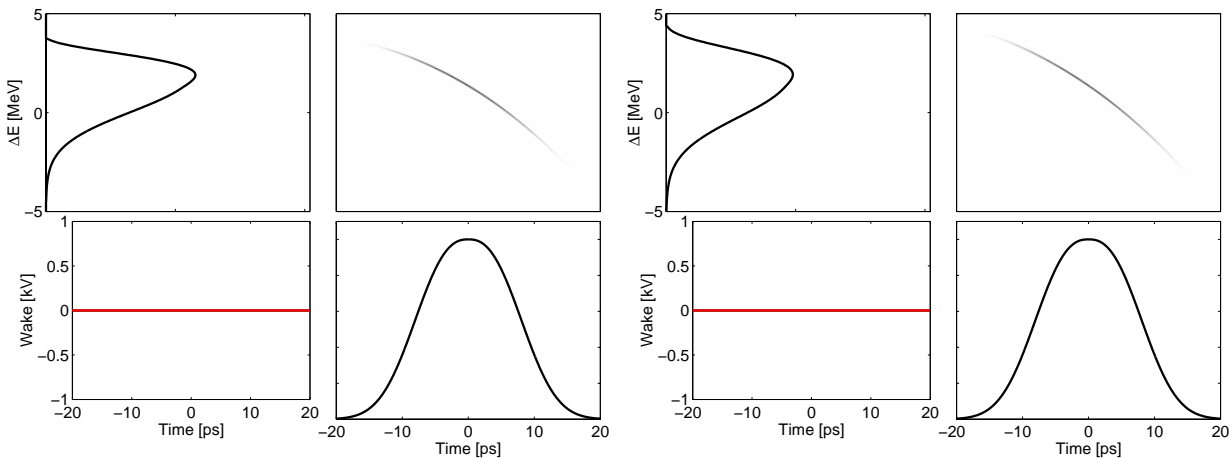

Figure 5.6: Simulated phase space at the entrance of the bunch compressor. In the figures 5.6-5.9 the left picture corresponds to a bunch at maximum compression and the right picture to a more moderate compression used in the wake field experiment. At the entrance of the bunch compressor only the energy profiles differ, the time profiles are equal.
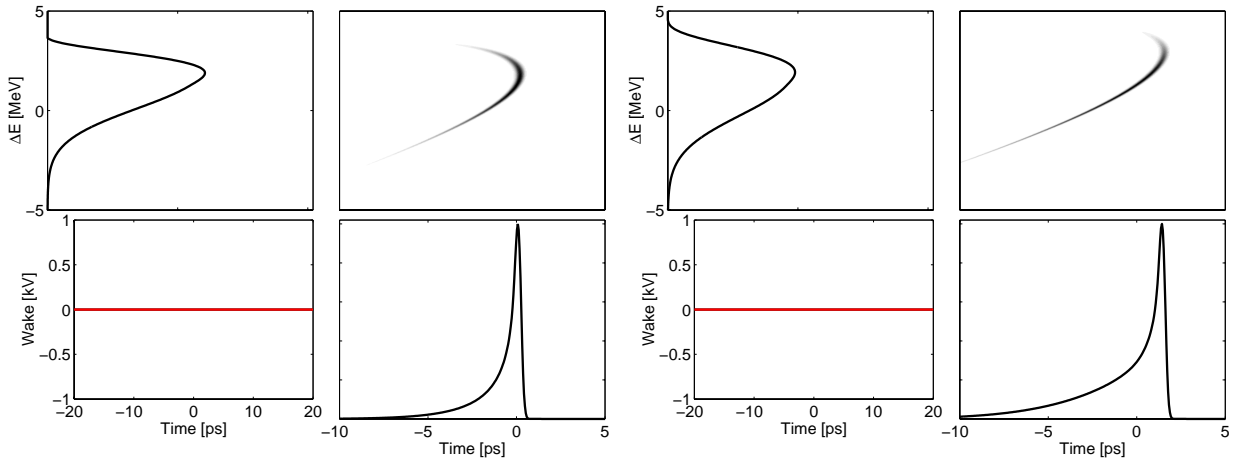
Figure 5.7: Simulated phase space at the exit of the bunch compressor. No wake or coherent synchrotron radiation has been taken into account.
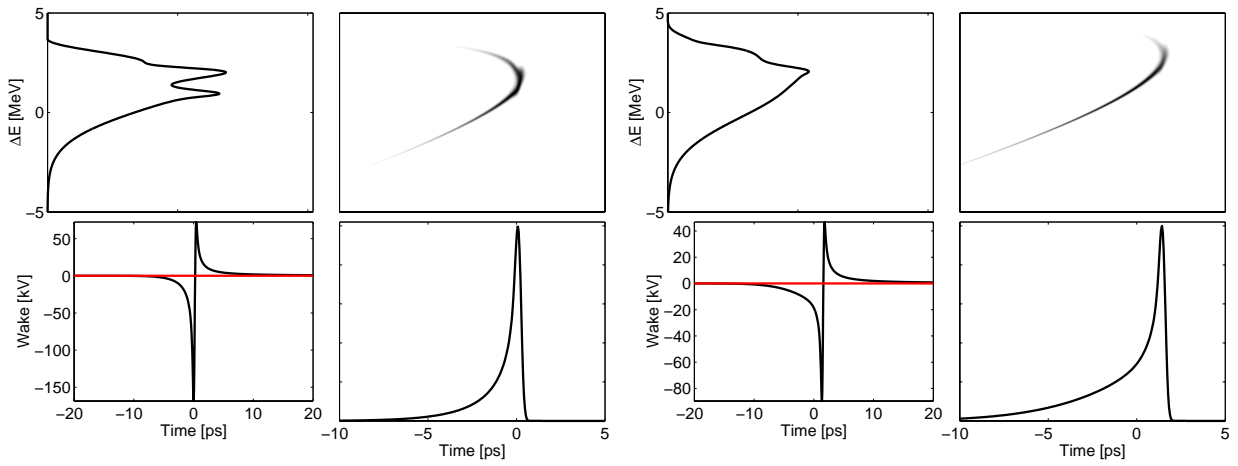

Figure 5.8: Simulated phase space at the exit of the bunch compressor with coherent synchrotron radiation taken into account.
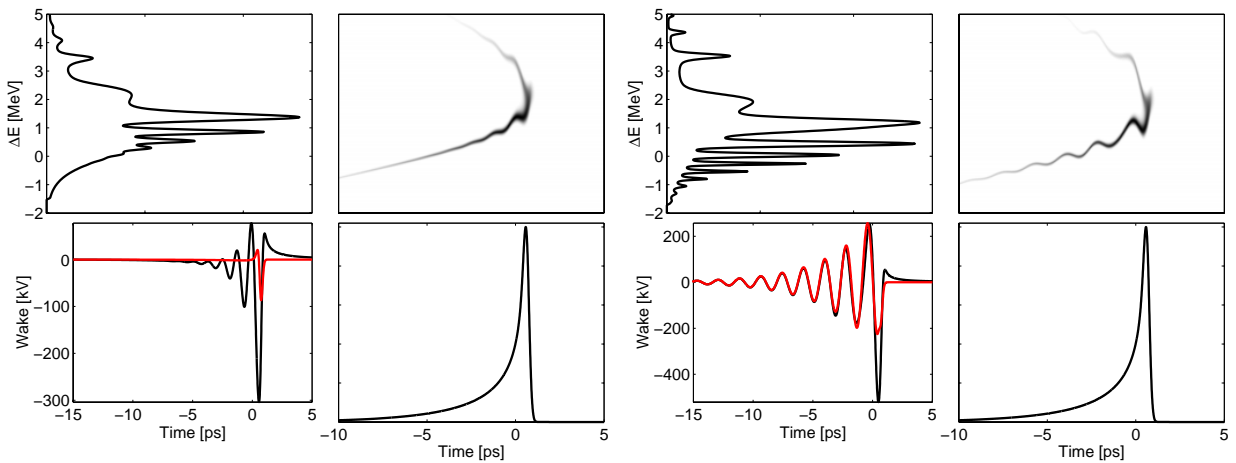

Figure 5.9: Simulated phase space of a bunch passing the 4 mm reference pipe of the wake field experiment (top) and passing the 4 mm sandblasted pipe (bottom).

Chapter 6

Experimental Tomography

6.1 Setup

The main accelerator components for the longitudinal phase space tomography are an acceleration module and the energy spectrometer with a straight section in between. By changing the rf phase in the module the longitudinal phase space of the bunches is deformed, and using the spectrometer the resulting energy profiles can be measured. Provided that there are no energy dependent effects on the bunches along this section, the phase space distribution in front of the spectrometer can be reconstructed.

Besides nonlinear corrections in this setup only a shearing of the phase space can be achieved. For maximum resolution the shearing has to be maximized. In the TTF the phase offset is limited by the fact that the two acceleration modules are driven by a single klystron. The phase and amplitude of the rf in the first module are kept constant while the phase of the second module can be shifted by a phaseshifter in the waveguide. The adjustment range of this phase shifter is 90°. When the rf phase is shifted by φ_{off} from the crest the energy is in first order modulated according to

$$d\mathcal{E} \quad = \quad E_0 \omega_0 \sin(\varphi_{off}) dt. \qquad (6.1)$$

The maximum energy shift of two points in the phase space against each other is then

$$
\begin{aligned}
\triangle\mathcal{E} \quad &= \quad E_0 \omega_0 \left[\sin(\varphi_{min} + 90°) - \sin(\varphi_{min})\right] \triangle t, \\
&= \quad \sqrt{2} E_0 \omega_0 \sin(45° - \varphi_{min}) \triangle t, \qquad (6.2)
\end{aligned}
$$

with φ_{min} the lowest phase of the rf and $\triangle t$ the separation of the two points in time. This is optimum for a range of the phase between $\pm 45°$ with a total energy shift of $\triangle\mathcal{E}/\triangle t = E_0 \omega_0 \sqrt{2} \approx 570$ keV/ps.

A second constraint is the beam transport along the accelerator. Due to the phase shift the energy of the beam changes. At $\phi_{off} = 45°$ the accelerating voltage in the second module changes by 30% and the total electron energy changes by 15%. Without an independent klystron for the second acceleration
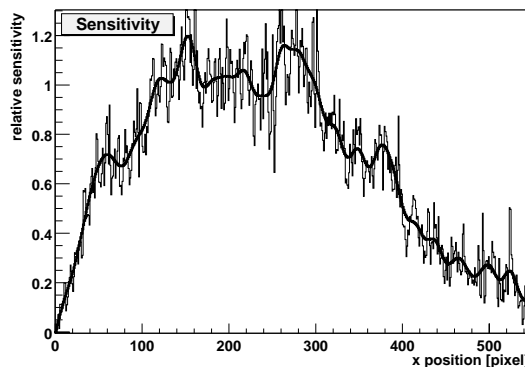

Figure 6.1: Sensitivity of the diagnostic screen in the energy spectrometer versus position on the screen. The parameters of the lens system have to be deduced from the observed signals because a zoom lens was used. The focal length was approximately 90 mm, the visible width of the screen was 37 mm. The aperture diameter was 16 mm corresponding to an f-number of 5.6.

module this cannot be compensated by changing the amplitude of the rf-field. The focusing onto the diagnostic screen has to be adjusted for the different energies to achieve the optimum spectrometer resolution. With additional adaption of the optics the beam transport can be optimized, but during the measurements this turned out unnecessary.

Behind the bunch compressor the energy distribution of the bunches has a total width of approximately 10 MeV. With a total bunch length of ≈ 10 ps and an additional modulation of 570 keV/ps for the tomography the full acceptance of the measurement system has to be at least 15 MeV. The dispersion at the position of the screen was 1 m, the total beam energy is 235 MeV.

To allow for a range of 15 MeV the OTR screen would have to cover 65 mm, whereas the installed screen is only 40 mm wide. At the same time the focusing of the beam would vary considerably across the screen yielding a poor energy resolution of the spectrometer. To overcome these difficulties the measurement was performed such that a number of images was taken for each projection. Therefore two quadrupoles in front of the dipole and the

34

dipole were scanned simultaneously in a predefined sequence.

A schematic of the spectrometer section is found in figure 6.7. The focusing is adapted with the quadrupoles Q2 and Q3, while Q4 and Q5 are adjusted for zero field. The beam position monitors BPM1 and BPM2 are used to find a reproducible orbit as input to the spectrometer.

During the operation of the TTF some jitter of the beam energy has been observed due to the missing rf control of module 2. Therefore the horizontal offsets between the images have to be adjusted individually. To ease this operation an overlap between subsequent images is desirable. Thus a large active area of the diagnostic screen is required. The active area of the screen is determined by the adjustment and acceptance of the optical system.

The screen is observed by a camera equipped with a zoom lens. To protect the camera from high energy photons and electrons it was necessary to shield it with lead. Therefore the direct view on the accelerator was blocked, and the light was deflected by a mirror onto the camera. The mirror had a diameter of 75 mm in order not to restrict the acceptance of the system. The distance of the camera lens from the screen was 450 mm, its focal length approximately 90 mm.

The detected optical transition radiation is very directional. The maximum intensity is found at an opening angle $1/\gamma$. Due to the narrow opening angle of the transition radiation the active area of the screen equals the effective aperture of the lens system. The optical system has to be adjusted such that the active area is centered on the screen. In absence of an alignment system the adjustment only could be verified using OTR itself. The camera could be moved horizontally via remote control. The vertical adjustment was done manually.

In the spectrometer dipole synchrotron radiation is produced. The OTR screen acts as a mirror for the synchrotron radiation and deflects it into the camera. Since its origin is far out of the focal plane it is not focused but appears as a brightening of the background. Since the origin of the synchrotron radiation is distributed along the orbit of the electrons the radiation cannot be subtracted directly. To suppress it the camera was equipped with a polarizing filter transmitting the vertical polarization only and hence suppressing the synchrotron radiation which is polarized horizontally.

Figure 6.1 shows the experimentally determined relative sensitivity of the screen. The relative sensitivity is measured by shifting the beam in small steps across the screen. With this the spectrometer was calibrated at the same time. The active width of the screen corresponds to 370 pixels on the CCD. The calibration of the spectrometer was 171 pixels per 1% energy shift. Thus the energy acceptance was approximately 2%. From the sensitivity measurement it was deduced that the aperture of the camera lens was 16 mm corresponding to an f-number of 5.6 at a focal length of 90 mm. Meanwhile a high-resolution macro lens was obtained with an f-number of 2.8. It was used to measure the energy profiles shown in figure 7.4. The correct horizontal shift of the images while scanning the spectrometer can be found by calculating the cross-correlation of two subsequent images. The maximum of the correlation function is found at the correct offset. It is sufficient to apply the cross-correlation to the projection of the image. After finding the correct offset the images were scaled to correct for intensity fluctuations.

The signal to noise ratio in figure 6.1 is poor. A substantial contribution to the noise in the energy profiles comes from x-rays hitting single pixels of the CCD. Obviously the shielding of the camera was insufficient. By eliminating isolated pixels from the image the noise was drastically reduced. The elimination of isolated pixels was done parallel to the direction of projection. In this way no degradation of the resolution is expected.

6.2 Measurements

The measurements were done with the bunch compressor and acceleration module 1 adjusted for maximum compression of the bunches. This is achieved by setting the phase of the rf field to $-12°$. The correct setting is verified with a far infrared detector measuring coherent transition radiation from the bunches.

In the TTF an unexpected phenomenon is observed: When the accelerator is adjusted for very short bunch lengths the energy spectrum of the bunches is split into several peaks. The investigation of this effect was the first motivation to perform the longitudinal tomography. Figure 6.2 shows the result of the first tomography to study this effect. Note that this measurement was done before the camera alignment was optimized and without scanning the spectrometer. Therefore the acceptance and resolution was lower than in later measurements.

Simultaneously with the tomography the longitudinal profile was measured by interferometry of the coherent transition radiation. The interferometer has been described in [15]. Since then the setup has been considerably improved by replacing the pyroelectric detectors with Golay-cell detectors. In this way a smooth response of the interferometer is achieved. In the interferometer the autocorrelation function of the CTR is obtained. The Fourier trans-
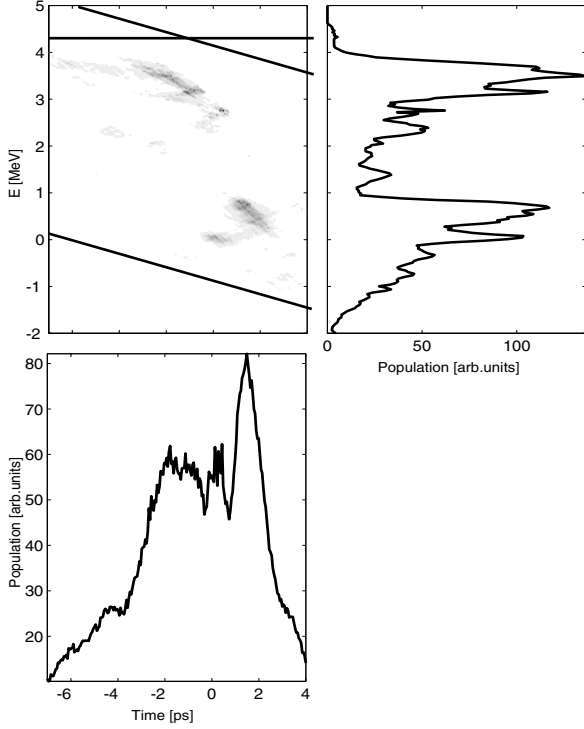
Figure 6.2: Longitudinal phase space of a TTF bunch at maximum compression [19]. The lines indicate the sensitive area. By better aligning the camera and scanning the spectrometer the sensitive area could be enlarged substantially (compare chapter 7).
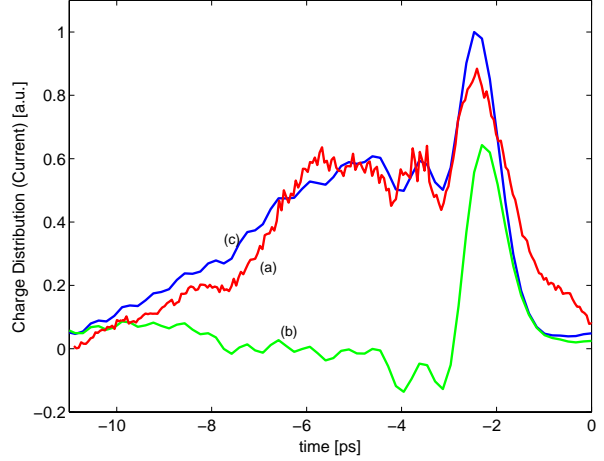

Figure 6.3: Longitudinal profile of bunches in the TTF measured with tomography (a) and interferometry (b) [51]. The data for the two methods was taken in the same week in April 2000. The fully reconstructed phase space is shown in figure 6.2. The interferometer data suffer from a low frequency cut-off which cuts away the tail of the bunch as can be seen on the lowest curve. For a better comparison low frequency components have been extrapolated (c).

form of the autocorrelation function is the square of the form factor of the bunch (see figure 6.4). Therefore the interferometer is principally unable to determine the phase of the bunch form factor. To reconstruct the longitudinal profile from the far infrared spectrum of the CTR the Kramers-Kronig relation is used to compute the phase as a function of frequency. Due to the symmetry of the autocorrelation function it is impossible to decide which is the head or the tail of the reconstructed bunch profile. This has to be deduced from additional information (simulation or measurement). Below approximately 60 GHz the interferometer shows a cut-off of the intensities, this has to be taken into account when comparing the result of the interferometry and the tomography (figure 6.3). An considerable enhancement of the low frequency intensities is required as can be seen in figure 6.4.

Meanwhile a streak camera with a temporal resolution of 200 fs is available. It has been used to measure the duration of the synchrotron radiation pulse created in the spectrometer dipole. The results are shown in figure 6.5. The tomography yields a shorter tail than the streak camera. In part this may be explained by different beam conditions in the two measurements, which were done

with a delay of two years. More important may be the limited acceptance discussed above. Note that this is a problem which has been fixed by the measures described above (see figure 6.6). Unfortunately since then no measurement has been done at maximum compression of the bunches, therefore a bunch profile at medium compression measured during the wake field experiment is shown.
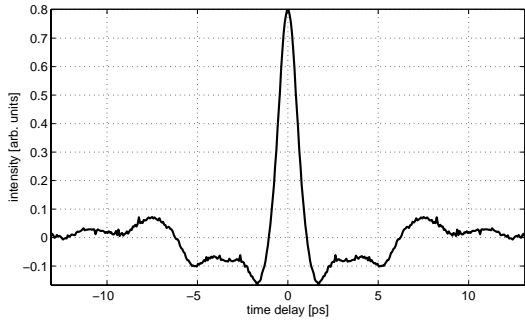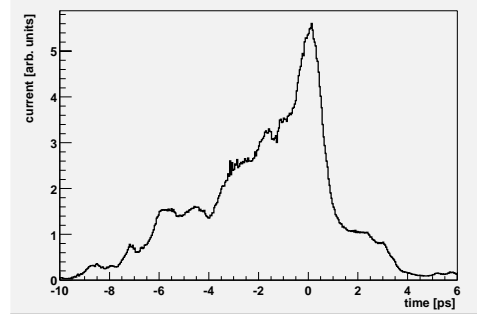
Figure 6.6: Longitudinal profile of bunches in the TTF during the wake field experiment, measured with tomography. The corresponding two dimensional phase space can be found in figure 7.6. The pedestal between approximately $t = 2 \ldots 4$ ps can be explained by the poor time resolution for structures parallel to the energy axis (see figure 4.7 for reference).

Figure 6.4: Autocorrelation function and power spectrum of the coherent transition radiation produced by a bunch at maximum compression. To obtain the reconstructed bunch shape shown in figure 6.3 low frequency components were enhanced (dashed-dotted line).
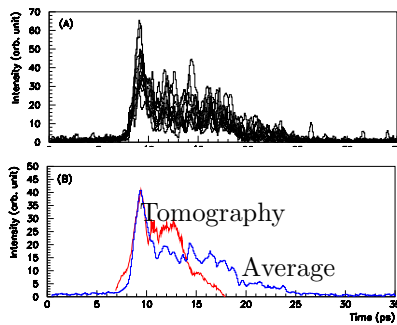
Figure 6.5: Longitudinal profile of bunches in the TTF measured with a streak camera [46] in March 2002. In these plots the head of the bunch is on the left side. The upper plot (A) shows single shot profiles, the lower plot (B) shows the average and the result from tomography. The shorter tail measured by tomography may in part be due to different beam conditions or due to reduced acceptance.
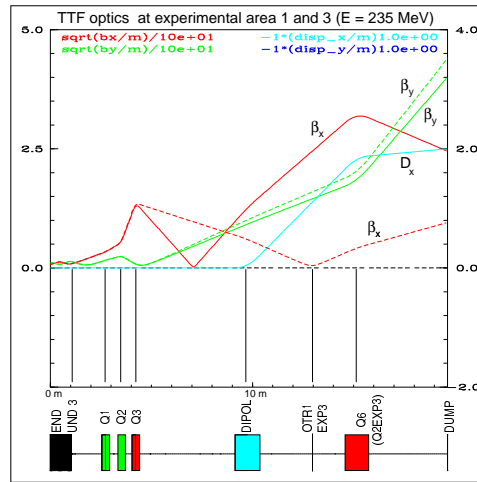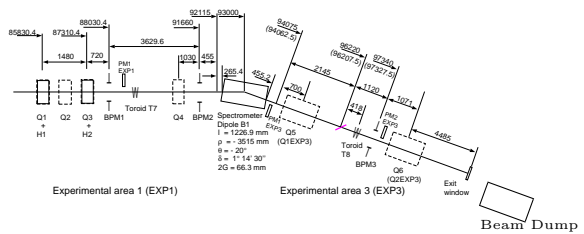
Figure 6.7: Beam line close to the spectrometer dipole and the optical functions [45]. The solid lines show the horizontal and vertical beta functions and dispersion during standard operation of the linac, when the beam cross section was made especially large at the exit window. For spectrometer operation the optics shown by dashed lines can be used. The gradient of quadrupole Q3 has to be changed by 20% to switch the optics. During the tomography measurements the quadrupoles Q2 and Q3 are used to adapt for different energies.

Chapter 7

The Wake Field Experiment

For the surface roughness wake field experiment test beam pipes with a known roughness of the inner surface have been prepared. The wakes excited by the test pipes have been analyzed using two different observables, the energy modulation of the beam and the radiated electromagnetic fields. For a clear separation of the surface roughness wakes from other effects such as coherent synchrotron radiation in the bunch compressor and undulator or wake field effects in other elements of the accelerator a difference measurement was performed.

A special ultra-high vacuum chamber [29] was constructed to house an ensemble of beam pipes with radii between 3 and 5 mm and with different surface preparations (smooth, sandblasted, grooved, see table 7.1). The chamber was mounted behind the undulator. Via a linear movement each beam pipe could be positioned on the beam axis. Due to the limited space in the accelerator the length of the beam pipes was limited to 855 mm. To increase the effects the test pipes were prepared with an enhanced surface roughness in comparison with the standard undulator vacuum chambers. The pipes were composed of two half cylinders machined into two flat aluminum plates. In this way a controlled surface preparation by sand-blasting or grooving was possible. The surface roughness has been measured with a tracer type measuring device featuring a resolution of 0.02 μm. The wake fields created by the two narrow longitudinal gaps are known to be negligible [10].

Seven beam pipes were prepared. One beam pipe with inner radius 8 mm was foreseen for the nominal linac operation. Its aperture was large enough to allow for transmission of beam pulses with the maximum possible average power. Three beam pipes with an inner radius of 4 mm have been prepared. The first of these has a smooth surface and served as a reference for all measurements. After machining the respective half pipes their inner surface were cleaned with NaOH. Their surface profile was measured to have an rms height of 1.6 μm. The second pair of half pipes has been sandblasted after ma-

chining and finally cleaned with NaOH. Their surface profile was measured to have an rms height of 10 μm. The third pair of half pipes was treated by sparking erosion to achieve regular grooves on the surface with a period of 150 μm and a depth of 60 μm. There were two additional beam pipes treated by sand-blasting with radii of 3 mm and 5 mm, and one beam pipe with grooves on the surface had a radius of 5 mm.

7.1 Energy profiles

Figure 7.1 shows the energy profiles as obtained when the beam passes the reference pipe and a sandblasted pipe, respectively. The accelerator was adjusted for a moderate compression of the bunches, 6.5° off-crest in module one instead of 12° as required for optimal compression. In this way the bunches were shaped such that they had a steep rising edge ($\sim$ 100 fs) and a long, slowly decaying tail ($\sim$ 10 ps). Then a 14° off-crest acceleration in the second module generates a correlated energy-position distribution in the tail of the bunch (see figure 7.2). The synchronous mode wake fields, which are mainly produced by the sharp front peak of the bunch, can then be observed via the imposed energy modulation in the long tail. There is some resemblance to the pump-and-probe technique in laser physics. Note that coherent synchrotron radiation in the bunch compressor, as well as wake fields caused by resistive walls and cross sectional changes, act mainly on the sharp front peak of the bunch but have little influence on the long tail.

The figure 7.1 shows only the tail of the bunches, the head is left of the border of the plot due to its lower energy. A clear difference of the profiles can be observed. When passing the smooth reference pipe the bunches show a wide and smooth energy spectrum. Superimposed is a slight structure which possibly can be assigned to wake field effects upstream of the experiment. This question will be discussed later in more detail.

The solid curve shows the energy distribution

pipe number	1	2	3	4	5	6	7
radius	8 mm	4 mm	5 mm	4 mm	3 mm	5 mm	4 mm
preparation	dummy	reference	sandbl.	sandbl.	sandbl.	grooves	grooves
δ rms	1.4 μm	1.4 μm	10 μm	10 um	10 um	(60 μm)	(60 μm)

Table 7.1: Parameters of the beam tubes. The parameter δ is the rms depth of the roughness. For the grooved pipes the depth of the grooves is printed instead of the rms height.
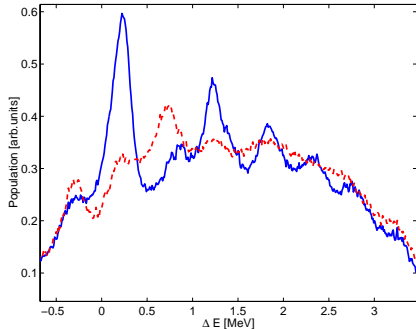

Figure 7.1: Difference measurement of smooth and rough beam pipes [20]. The dashed curve shows the energy profile after passing the reference pipe, whereas the solid curve shows the energy profile when passing a pipe of same geometry but sandblasted surface.
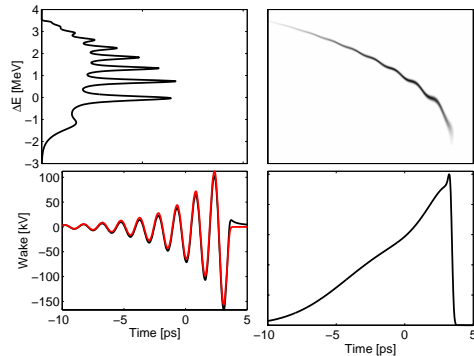

Figure 7.2: Simulation of a bunch in longitudinal phase space in the presence of a synchronous mode wake field. The upper left part shows the bunch in phase space, the lower left the projection onto the time axis, and the upper right the projection onto the energy axis. The lower right plot shows the harmonic wake field. The periodic energy shift together with the time-energy correlation generates the peaks in the energy distribution.

when the beam has passed the sandblasted beam pipe of the same radius $r = 4$ mm. In this case a regular peak structure is visible which can be assigned to a harmonic wake potential: each peak can be identified with a zero crossing of the wake potential with negative slope (see figure 7.2). It should be emphasized that the only difference between the two cases is the different surface roughness of the two pipes. Figure 7.4 demonstrates that the regular peak structure becomes much more pronounced when the rough pipe of 3 mm radius is inserted.

A precise determination of the time structure of the distribution is achieved by varying the rf phase of the second acceleration module. This has no impact on the longitudinal bunch profile nor on the wake fields. By measuring the resulting changes in the energy separation of the peaks it is possible to resolve their separation in time without making any assumptions about the initial energy distribution. The method works as follows. Consider two peaks in the energy profile which are separated in energy by E_{sep} and in time by τ. When the rf phase ϕ in module 2 is changed by $\Delta\phi$ the change in separation energy is

$$\Delta E_{sep} = \omega\tau E_{module} \left(\sin(\phi + \Delta\phi) - \sin(\phi)\right) \quad (7.1)$$

with E_{module} being the maximum energy gain in the module and ω the rf angular frequency. From the measured values $\Delta\phi$ and ΔE_{sep} the time sep-

aration τ of the two peaks can be derived with an accuracy of better than 120 fs. Then $f_w = 1/\tau$ is the frequency of the harmonic wake.

Using this method it was verified that the peaks seen behind the rough test pipes (figures 7.1 and 7.4) have indeed equidistant spacing in time, implying that they are caused by a harmonic modulation of the particle energies. The experimentally determined wake frequencies for the different rough test pipes are summarized in table 7.1 and plotted in figure 7.3 as a function of the pipe radius. Good agreement with the $1/\sqrt{r}$ behaviour of equation 2.36 is found. The fact that the time separation of the peaks changes with the pipe radius rules out the vague possibility that the observed regular peak might be due to an initial modulation of the bunch which is only enhanced by the rough pipes.

The observed harmonic wake frequencies agree with the dielectric layer model prediction for a dielectric constant $\varepsilon_{eff} \approx 1.55$ while the numerical calculations in ref. [52] prefer $\varepsilon_{eff} \approx 2$, corresponding to $\approx 20\%$ lower frequencies. In the surface roughness model of ref. [48] higher wake frequencies are predicted ($\varepsilon_{eff} \approx 1.27$) but it should be remarked that the small angle approximation for the irregularities, used in this paper, is not fully

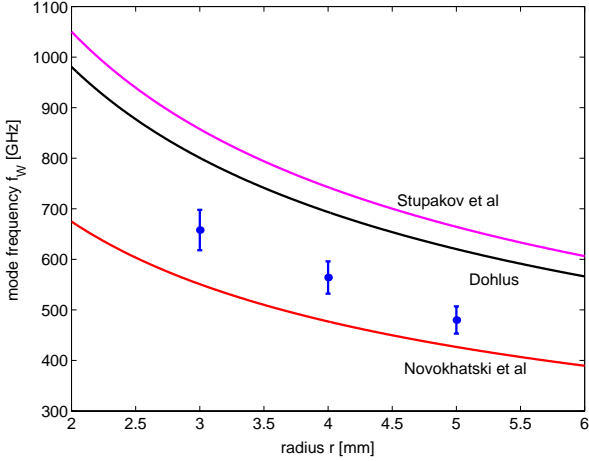justified for the sandblasted beam pipes of the experiment.

Figure 7.3: The frequency of the synchronous mode plotted versus the radius of the beam pipe.

It has been shown that the frequencies of the harmonic wakes can be determined in a model-independent way, applying the method described above. Their strengths can be derived with a longitudinal phase space tomography, which is an extension of this method. For an estimate of the wake field amplitude a numerical simulation of the whole experiment is carried out with the program described in chapter 5. The wake field effect in the rough test pipe is imposed as a damped harmonic wave using the frequency determined above. The simulation model yields the following values for the maximum energy shift which an electron in the tail of the bunch experiences during its passage through one of the 800 mm long roughened test pipes: 39 keV for $r = 5$ mm, 60 keV for $r = 4$ mm, and 105 keV for $r = 3$ mm. The amplitudes of the wake functions required to achieve these values agree well with the predictions $Z_0 c/(\pi b^2)$ from the wake field models. The damping constants are 4.8 ps for $r = 5$ mm, 4.0 ps for $r = 4$ mm, and 3.4 ps for $r = 3$ mm.

To account for possible surface-roughness wakes in the collimator and undulator section, which may be the origin of the peak structure observed behind the smooth reference test pipe, another dielectric-layer wake is used in the simulation whose frequency and amplitude is adjusted to yield a reasonable description of the energy profile measured with the reference pipe. Simulation parameters like the initial charge distribution and the rf phases in modules 1 and 2 are allowed to vary within the experimental uncertainty. The dashed curves in figure 7.4 are the predictions of the model simulation for an optimized parameter set. The main parameters are an accelerating voltage of 107 MV in both modules, an
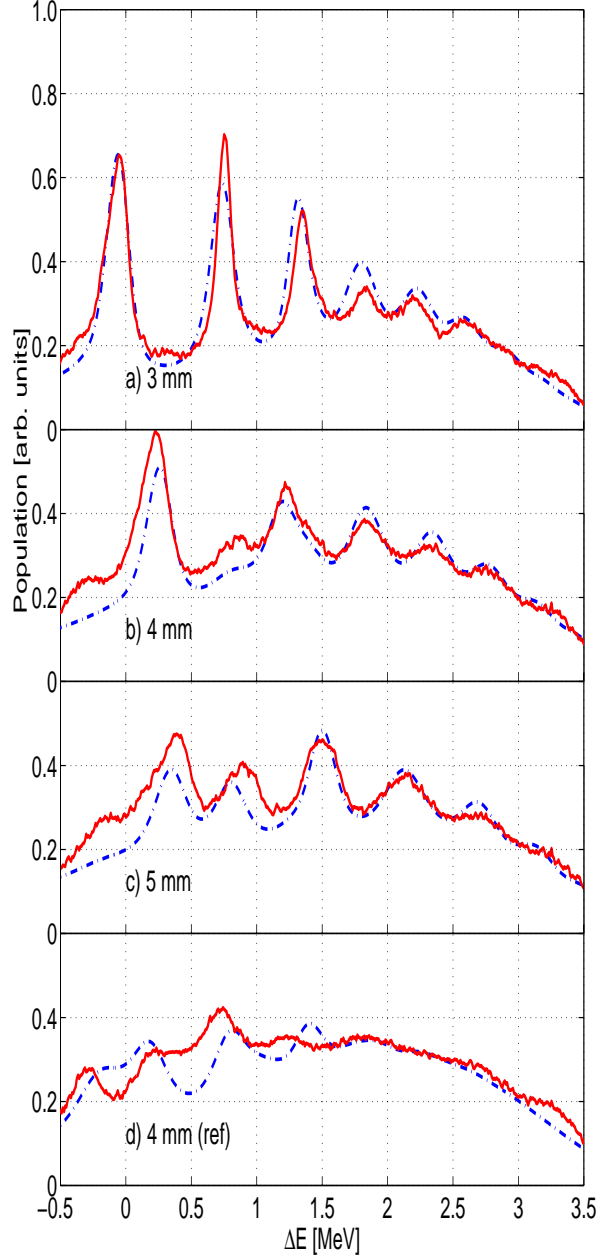

Figure 7.4: Energy profiles in the tail of the bunch measured behind different test tubes.a), b), c): sandblasted tubes of 3, 4, resp. 5 mm radius, d): smooth reference tube of 4 mm radius. The solid curves show the profiles measured with the spectrometer at the end of the linac. The dashed curves show the simulated distributions. The simulation includes the off-crest acceleration, bunch compression, and surface roughness wake fields generated in the test beam pipes and in the collimator upstream of the setup. The spectrometer resolution is also taken into account.

off-crest phase of $-6°$ in the first, and $-14°$ in the second module. With the latter the contrast in the energy profiles behind the 3 mm sandblasted test pipe was optimized. The agreement with the measured profiles is quite satisfactory indicating that the basic physics processes are well understood.

It should be noted that the determination of the wake frequency, the damping constants and the maximum energy shift is independent of any specific wake field model.

7.2 Tomography

For a more precise understanding of the wake field effects the longitudinal phase space of the bunches has been analyzed via tomography (see chapter 4). During the tomography measurements the setup was chosen slightly different from the one described in the previous section. Instead of setting the phase of the first acceleration module lower than required for maximum compression here it is set higher. Again the result is a moderately compressed bunch but the tail now lies at low energies. The peaks in the energy distribution correspond to the points where the wake potential crosses zero with positive gradient. Due to the limited angle of observation in the tomography they appear as peaks in the reconstructed phase space as well. By determining the distance of the peaks in time domain the frequencies of the wakes can be measured. The error of this time measurement is smaller than 120 fs. It is the same as for the energy profile measurement described in the last section. In figure 7.5 the reconstructed phase space is shown as it appears when the beam passes the 4 mm reference beam pipe. In figure 7.7 the phase space with 1 nC is shown again with the contours of a simulated bunch plotted on top. Obviously there is a regular structure on the bunch. In particular note the enhanced density at (0 ps, 2.4 MeV). At energie deviations below 0 MeV the dark spots correspond to zero crossings of the wake potential with positive slope. Above 2 MeV the dark spots are found where the wake potential crosses zero with negative slope. The frequency of the corresponding harmonic wake field is determined to be 830 ± 60 GHz. Having established the main features of surface roughness wake fields in the last section, it appears that the regular structure on the bunch most probably is caused by surface roughness wake fields. The reference pipe itself is ruled out as a source for this wake: The surface structure is too smooth and changing to a pipe of 8 mm radius does not change the structure on the energy profile.

Owing to their narrow aperture the undulator vacuum chamber or the collimator section might
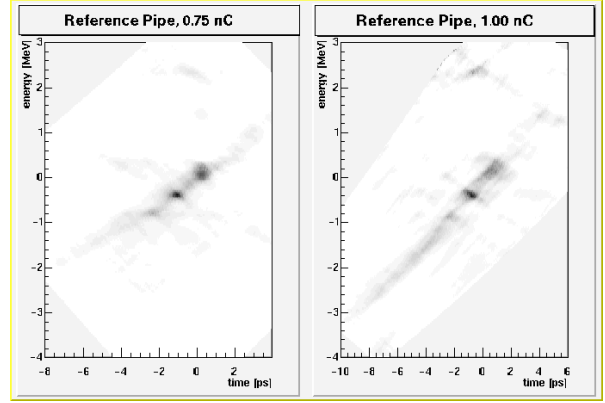

Figure 7.5: Reconstructed phase space behind the reference beam pipe. The left plot corresponds to a bunch charge of 0.75 nC, the right plot to a charge of 1.0 nC. At energie deviations below 0 MeV the dark spots correspond to zero crossings of the wake potential with positive slope. Above 2 MeV the dark spots are found where the wake potential crosses zero with negative slope. Between 0 and 2 MeV the distribution is not reconstructed correctly (see chapter 4). From the distance between the spots a wake frequency of 830 ± 60 GHz can be deduced. With increasing bunch charge the wake get stronger. This can be seen in the right by the stronger tilt of the dark spots.

have caused the wake in question. The surface roughness of the undulator chamber is $\lesssim 0.7 \mu m$ (rms) at a pipe radius of 4.5 mm yielding wake frequencies of 1.6-5 THz depending on the model. Should the undulator by some unknown reason excite wakes with a resonance frequency of 830 GHz, the wake field would have to be much stronger than observed because the effect would be integrated along the large length of 15 m. Therefore the undulator can be ruled out as a source of this structure.

In chapter 5 it has been shown that a harmonic wake at 830 GHz can be explained by surface roughness wakes produced in the collimator. Therefore the collimator is most likely the origin of the regular structures observed in the longitudinal phase space.

Figure 7.6 shows the reconstructed phases space of a bunch having passed a sandblasted beam pipe of 4 mm radius (equal to the reference pipe). In figure 7.8 it is shown again together with the contours of a simulated phase space distribution. The overall form of the distribution is that of a sickle as it is expected from simulations of the beam transport through the bunch compressor (see chapter 5). Superimposed is an energy modulation of the electrons. Within the limitations of the tomography it can be identified as being caused by a harmonic wave (see figure 4.7 for comparison). The amplitude of the modulation is much larger than in figure 7.5. The energy modulation is larger than the energy difference between the zero crossings, leading
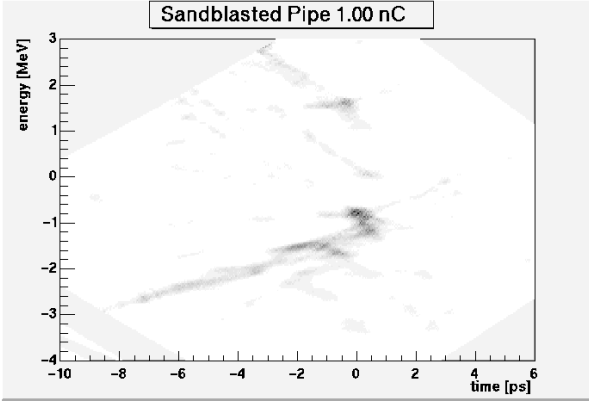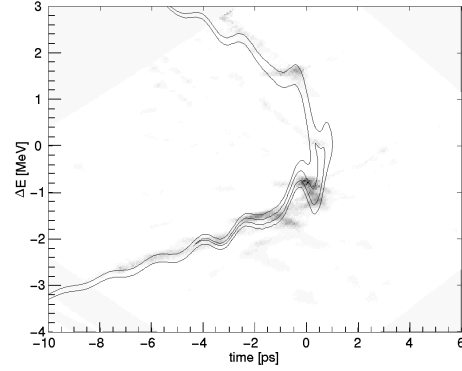
Figure 7.6: Reconstructed phase space having passed the sandblasted pipe with radius b=4 mm. At energie deviations below 0 MeV the dark spots correspond to zero crossings of the wake potential with positive slope. Above 2 MeV the dark spots are found where the wake potential crosses zero with negative slope. Between 0 and 2 MeV the distribution is not reconstructed correctly (see chapter 4). From the distance between the spots a wake frequency of 575 ± 30 GHz can be deduced.
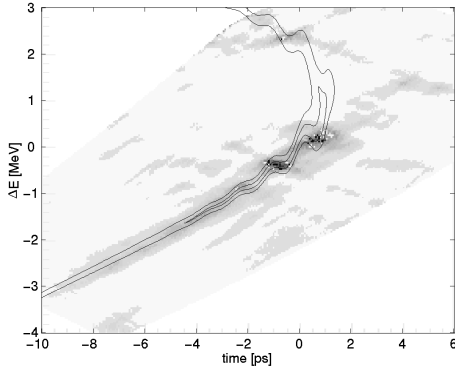

Figure 7.7: Tomographic reconstruction of the bunch having passed the reference pipe. The distribution from figure 7.5 has been plotted together with the contours of the simulated distribution from figure 5.9.

to a double peak structure where the peaks belong to the maximum respectively minimum of the sine function. The frequency of the modulating wave can be determined from the distance of the points of higher density in the reconstruction. It is found to be 575 ± 30 GHz in good agreement with other measurements described in the previous and following sections.

7.3 Microwave Measurements

Surface roughness wakes are special waveguide-modes propagating in the beam pipe. At the exit of the test pipes they are radiated into the larger vacuum chamber of the accelerator. At the TTF

Figure 7.8: Tomographic reconstruction of the bunch behind the 4 mm sandblasted pipe. The distribution from figure 7.6 has been plotted together with the contours of the simulated distribution from figure 5.9.

linac a diffraction radiation screen was used to deflect the radiated fields through a quartz window out of the vacuum. In a far infrared interferometer the wake fields then were analyzed. A detailed description of the interferometer can be found in [15]. The diffraction radiator screen was divided into two parts giving the opportunity to open a slit of 10 mm width. At the exit of the test beam pipes and at the screen also coherent diffraction radiation(CDR) respectively transition radiation (CTR) is produced yielding radiation in the same frequency range as the wakes. Therefore the analyzed spectrum contains a wide, continuous spectrum from the CDR resp. CTR and single spectral lines from the harmonic wakes.
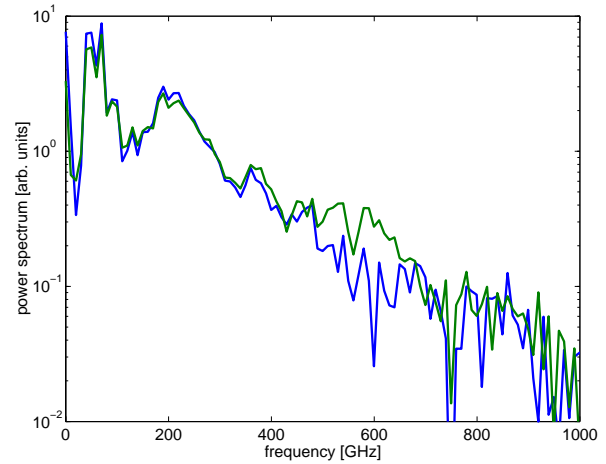
(b)

(a)

Figure 7.9: Far infrared spectrum with the 4 mm reference pipe (a) and the 4 mm sandblasted pipe (b). Around 560 GHz the two spectra clearly deviate. At 550 GHz and 750 GHz there are some absorption lines due to water vapour (see figure 7.10). The spectra were taken with the screen opened by 10 mm.

To separate the effects the spectra from the reference pipe and the roughened pipes can be compared. The figure 7.9 shows the comparison of two spectra obtained with pipes of equal radius of 4 mm. One spectrum corresponds to the reference pipe with smooth surface, the second to a sandblasted beam pipe with a rms roughness of 10μm. Around 550 GHz the power spectrum from the sandblasted pipe shows a clear enhancement. A problem is that at 560 GHz a narrow gap occurs caused by water vapour absorption. See the figure 7.10 for reference.
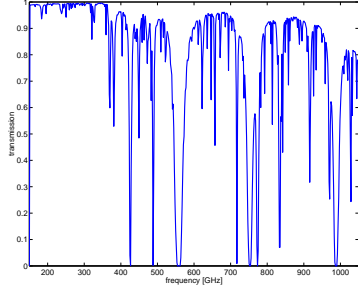

Figure 7.10: Atmospheric transmission at far infrared frequencies. The transmission has been simulated by the program `atm_cso` [28, 9]. It plots the zenith atmospheric transmission on the summit of Mount Mauna Kea in Hawaii. The amount of water vapour in the air can be given as input parameter by quoting the effective column height. For a column height of 185 μm the program delivers similar results to [35]. The plot shown here has been obtained for a column height of 30 μm which was estimated to be present at a relative humidity of 60%, a temperature of 22°C, normal pressure, and a path length of 2.5 m in the interferometer.
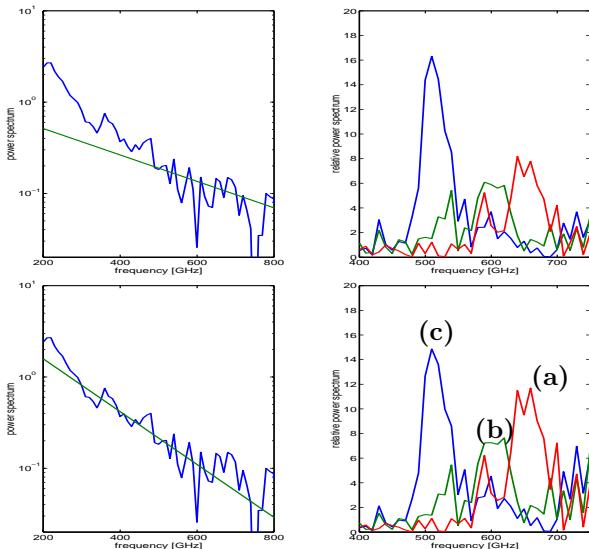

Figure 7.11: Radiated wake fields from three different sandblasted beam pipes. The radii of the pipes are (a) 3 mm, (b) 4 mm, and (c) 5 mm. The spectra were taken with the screen closed. Additionally there is a water absorption line at 560 GHz. For the reference spectrum two different exponential fits were used as can be seen in the left pictures.
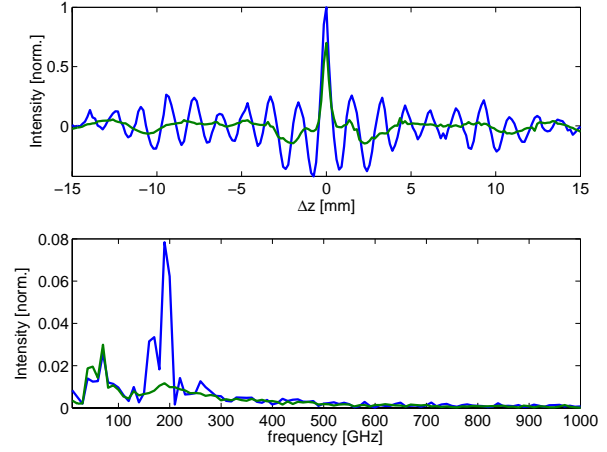

Figure 7.12: Autocorrelation function and corresponding spectrum with the $r = 4$ mm grooved beam pipe inserted. The corresponding functions from the reference pipe are shown in the same plots with the amplitude scaled such, that the spectra outside the resonance coincide.

In figure 7.11 the spectral lines of three different sandblasted pipes are shown. In this measurement a worse signal to noise ratio was obtained. This is because the measurements were done with the central slit of the screen opened to 10 mm. In this way the spectral lines of the wakes should be enhanced in comparison to the CDR spectrum. But due to the poor signal to noise ratio the reference spectrum delivers no reliable data at the relevant frequencies. Instead an exponential fit to the spectra from figure 7.9 served as a reference. Two different fits were used, one only based on the data close to 500 GHz, the other one based on the data from 200 GHz to 600 GHz. In figure 7.11 the fits are shown in the corresponding left graphs.

At first sight the relative strength of the spectral lines is opposite to what can be expected from calculation and from the measurements of the beam energy. Without losses the pulse energy W should drop with the beam pipe radius like $W \propto 1/b^2$ and increase with the frequency like $W \propto f^4$ whereas the spectral lines tend to be slightly weaker for higher frequencies. In the lossless case the pulse length τ would be decreasing with the radius $\tau \propto 1/b$ while from the Dohlus model and the measurements presented in table 7.2 a different behaviour is found: $\tau \propto b$. If this is taken into consideration the radius dependence is compensated, so the energy contained in the wake field pulse should be independent of b. Within the errors this is found in figure 7.11. The weakness of the middle line most probably is caused by the atmospheric absorption.

Much clearer signals have been observed from the grooved beam pipes. In figure 7.12 an autocorrelation function and the corresponding spectrum are shown for the 4 mm test pipe with grooves on the
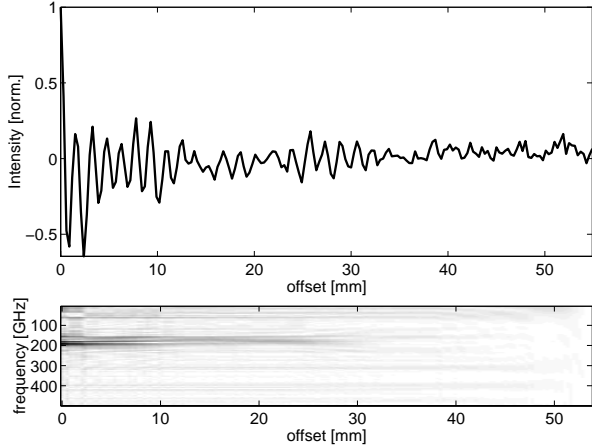
Figure 7.13: Autocorrelation function with the 4 mm grooved beam pipe inserted. In the lower plot the spectrum is plotted in columns taking into account the autocorrelation function between the corresponding point on the x-axis and the end.
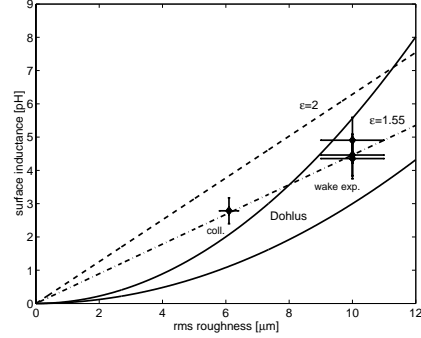

Figure 7.14: Inductance versus the height of the surface roughness. The experimental data from the wake field experiment and collimator are shown. The behaviour of the inductance derived from the linear boundary approximation (Dohlus) are shown for roughness spectra similar to (a) those in the collimator (b) those in the wake field experiment. The dielectric layer model with $\varepsilon = 2$ and $\varepsilon = 1.55$ (Novokhatski et al.) is shown.

surface. A strong harmonic modulation of the autocorrelation function is observed. The resonance frequencies are found at 200 ± 10 GHz for b=4 mm and 177 ± 10 GHz for b=5 mm. At the central peak the autocorrelation function with wake exceeds that without wake by 50 %. This means that the total energy in the wake field radiation pulse is approximately half as much as in the CTR pulse.

Given this ratio the autocorrelation is dominated by the front peak of the CTR[1] scanning the harmonic function of the wake field radiation. In figure 7.13 the autocorrelation function is plotted for positive offset in one interferometer arm over a large range. The corresponding spectra are plotted vertically taking into account only part of the autocorrelation function. Therefore the spectra were calculated between a starting offset z_1 and the maximum offset $z_{max} = 55$ mm.

$$S(k, z_1) = \frac{1}{z_{max} - z_1} \int_{z_1}^{z_{max}} A(z) \exp(ikz) dz, \quad (7.2)$$

with A the autocorrelation function. Moving from $z_{min} < z_1 < z_{max}$ the relevant part is further and further cut. At approximately $z_1 \approx 26$ mm the intensity of the 200 GHz harmonic wake starts to drop and vanishes at 30 mm. From the group velocity derived in chapter 2 a pulse length of $L \approx 23$ mm $\hat{=}77$ ps is expected, which is in good agreement with this observation.

7.4   Summary

The results of the wake field experiment are listed in table 7.2. The figure 7.14 shows the correspond-

ing surface inductances for the pipes with stochastic surface structure. The pipes with a regular and 60 μm deep structures are well described by the dielectric layer model with $\varepsilon = 2$. This supports the treatment in section 2.3.1 whereas [2] deviates by 20%. The harmonic wakes in the sandblasted pipes can be described with an $\varepsilon \approx 1.6$ yielding frequencies right in the middle between the predicted $\varepsilon = 2$ and the calculations according to Dohlus. For the smaller surface roughness in the collimator the Dohlus model fits within 15%.

The amplitudes of the wake functions have the same value $Z_0 c/(pib^2)$ in all wake models and are in good agreement with the observations. The time constants agree best with the predictions by a combination of the Dohlus model and the dielectric layer model (see figure 7.15). From the group velocity of the modes (described for dielectric layers) the radius dependence should be opposite to the observations. Among all models discussed in this thesis the Dohlus model [12] delivers the best description of surface roughness wakes in case of shallow surface structures. Very deep surface structures are best described by the dielectric layer models with $\varepsilon = 2$. Hence these two models can be regarded as the two limiting cases.

---

[1]excited by the front peak of the bunch

preparation	r/mm	δ rms	f_w/GHz	ε_{eff}	ampl./kV	τ/ps
reference	4	$1.4\,\mu m$	-	-	-	-
sandblasted	5	$10\,\mu m$	480 ± 27	1.64	39 ± 5	4.8
sandblasted	4	$10\,\mu m$	564 ± 32	1.55	60 ± 5	4.0
sandblasted	3	$10\,\mu m$	658 ± 40	1.53	105 ± 10	3.4
grooves	5	$60\,\mu m$	177 ± 10	1.94	-	-
grooves	4	$60\,\mu m$	200 ± 10	1.90	-	77
collimator	3	$5.7\,\mu m$	830 ± 60	1.55	-	-

Table 7.2: Summary of results for different beam tubes. The parameter δ is the rms depth of the roughness except for the eroded pipes where it is the depth of the grooves. The wake frequencies f_w have been determined from the energy distribution of the electron bunches and verified with the interferometer. The 6th column gives the amplitude of the wake potential and the last column the decay constant resp. pulse length.
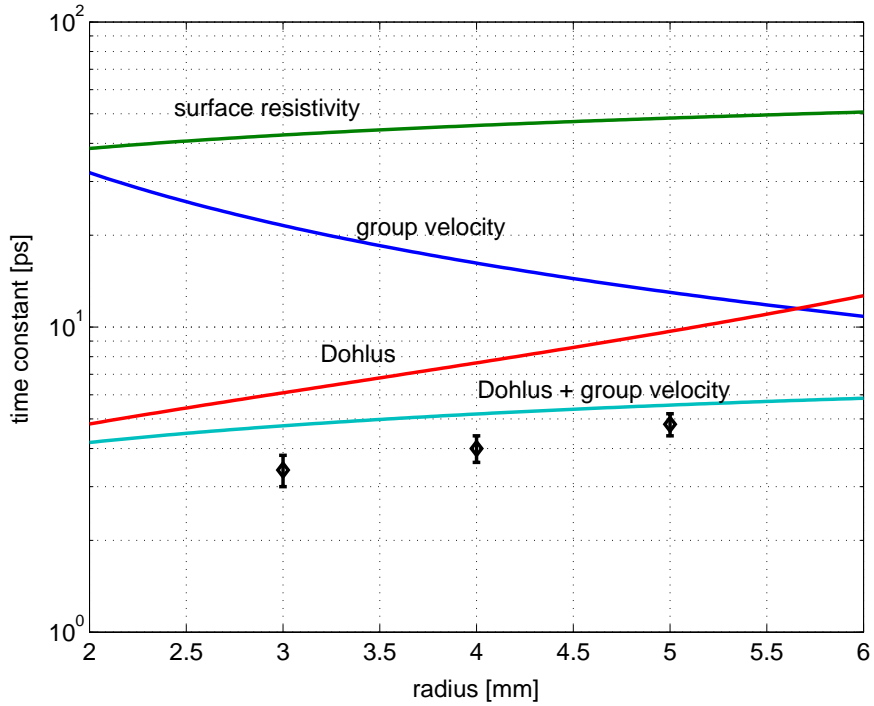

Figure 7.15: Time constants of the surface roughness wake. Predictions made by different models are plotted for comparison. Only the combination of the Dohlus model with a dielectric layer wake model yields reasonable agreement with the measurement.

Chapter 8

Conclusion and Outlook

Surface roughness wake fields are a significant concern for the performance of high gain free electron lasers. The worry is that already micrometer-size structures on the inner surface of the undulator beam pipes could severely degrade the energy distribution inside the bunches. The waveguide modes inside the beam pipe are slowed down by a rough surface and at a certain characteristic frequency energy can be transfered resonantly from the beam to a radiation field. A similar effect happens in beam pipes covered with a dielectric layer. Although the surface roughness wake fields have received a considerable theoretical attention, no convincing conclusion had been found since the energy losses predicted by the theories differed by orders of magnitude.

To clarify the situation an experiment has been conducted at the TESLA Test Facility to study the surface roughness wake fields. By introducing beam pipes with an enhanced roughness of the inner surface strong wake fields could be excited that allowed a detailed investigation. Two methods were employed to detect the wake fields: The wake field radiation was measured in a far infrared interferometer and the influence of the wakes on the beam was investigated by measuring the energy profiles of the bunches and applying the methods of tomography to it. In this way it was possible to measure the longitudinal phase space of the bunches. At the TESLA Test Facility no rotation of the longitudinal phase space was possible. To obtain reliable results a tomography algorithm based on the maximum entropy method was applied. It is a powerful tool to study processes in the longitudinal phase space like bunch compression, wake fields, and coherent synchrotron radiation. The suppression of artefacts achieved by the maximum entropy method makes the algorithm attractive also for the transverse phase space. There it can lead to a reduction of required quadrupole currents, a relaxation of constraints on rotation angles, and a reduction of the number of required images.

Harmonic wake fields were detected in accordance with a dielectric layer model. For stochastic surface structures which were produced by sand-blasting the observed frequencies can be explained assuming an effective dielectric constant in the order of 1.6. In numerical studies made for periodic and relatively large structures an ε of approximately 2 was predicted, yielding resonance frequencies 20% lower than measured, whereas with a linear approximation of the surface structures resonance frequencies are calculated which are 20% higher than the measured values. The two different calculation methods can be regarded as the asymptotic solutions for very large respectively very shallow surface structures. The surface structures in the wake field experiment with an rms height of 10 μm lie in between, the surface structures with an rms height of 6 μm in the collimator are already well described by the linear boundary approximation.

The observed time constants in the order of a few ps of the wakes are a strong hint that the linear boundary approximation according to Dohlus [12] is the correct description for surface roughnesses in the order of micrometers and below. For the undulator vacuum chamber with a measured surface roughness of approximately 600 nm this model predicts that the roughness wake is negligible in comparison with the resistive wall wakes. Therefore it can be concluded that for the surface roughness the preparation of the undulator vacuum chambers as it was described in [16] is sufficient for future FEL projects.

It should be remarked that the Dohlus model was derived for axially symmetric surface structures only. The transition to an isotropic surface roughness was done in analogy to the Stupakov model. Deriving this more rigorously may improve the agreement between calculations and measurements.

Instead of regarding the wake fields as a parasitic effect they may also be utilized in future FEL projects. They may be used as a radiation source of their own. Or – due to the variation of the wake field strength along the bunch – they may be used to shorten the photon pulse by impeding the FEL process in parts of the bunches.

46

Appendix A

Derivatives

Group velocity

$$k = \sqrt{\frac{2\varepsilon}{(\varepsilon-1)b\delta}\left(\frac{J_0(k_r b)}{J_2(k_r b)+J_0(k_r b)}-\frac{b\delta}{2\varepsilon}k_r^2\right)} \tag{A.1}$$

$$\frac{\mathrm{d}k}{\mathrm{d}k_r} = \frac{1}{2}\sqrt{\frac{2\varepsilon}{(\varepsilon-1)b\delta}}\frac{\frac{\mathrm{d}}{\mathrm{d}k_r}\left(\frac{J_0(k_r b)}{J_2(k_r b)+J_0(k_r b)}-\frac{b\delta}{2\varepsilon}k_r^2\right)}{\sqrt{\frac{J_0(k_r b)}{J_2(k_r b)+J_0(k_r b)}-\frac{b\delta}{2\varepsilon}k_r^2}} \tag{A.2}$$

$$= \frac{\varepsilon}{(\varepsilon-1)b\delta k}\cdots \tag{A.3}$$

Series expansion of k_m and k_z

According to equation 2.31 k_m is

$$k_m = \sqrt{\frac{2\varepsilon}{(\varepsilon-1)b\delta}\left(\frac{J_0(k_r b)}{J_2(k_r b)+J_0(k_r b)}-\frac{b\delta}{2\varepsilon}k_r^2\right)} \tag{A.4}$$

Inserting the series expansion of the Bessel functions

$$J_0(x) = 1 - \frac{x^2}{4} + \frac{x^4}{64} - \frac{x^6}{2304}\cdots \tag{A.5}$$

$$J_1(x) = \frac{x}{2} - \frac{x^3}{16} + \frac{x^5}{384} - \frac{x^7}{9216}\cdots \tag{A.6}$$

into A.4 taking into account that $\xi = b^2 k_r^2$

$$k_m = \sqrt{\frac{2\varepsilon}{(\varepsilon-1)b\delta}\left(\frac{1-\frac{b^2\xi}{4}+\frac{b^4\xi^2}{64}-\frac{b^6\xi^3}{2304}\cdots}{1-\frac{b^2\xi}{8}+\frac{b^4\xi^2}{192}-\frac{b^6\xi^3}{4608}\cdots}-\frac{\delta}{2b\varepsilon}\xi\right)} \tag{A.7}$$

Performing the polynomial division

$$= \sqrt{\frac{2\varepsilon}{(\varepsilon-1)b\delta}\left(1-\frac{b^2\xi}{8}-\frac{b^4\xi^2}{192}-\frac{b^4\xi^3}{4608}\cdots-\frac{b\delta}{2\varepsilon}\xi\right)} \tag{A.8}$$

With $k_{res}=\sqrt{\frac{2\varepsilon}{(\varepsilon-1)b\delta}}$

$$= k_{res}\sqrt{1-\frac{b^2\xi}{8}-\frac{b^4\xi^2}{192}-\frac{b^6\xi^3}{4608}\cdots-\frac{b\delta}{2\varepsilon}\xi}. \tag{A.9}$$

The terms with ξ^1 are grouped with the abbreviation $a_m = \frac{b^2}{8} + \frac{b\delta}{2\varepsilon}$

$$= k_{res}\sqrt{1 - a_m\xi - \frac{b^4\xi^2}{192} - \frac{b^6\xi^3}{4608}\dots} \tag{A.10}$$

Now inserting the expansion

$$\sqrt{1-x} = 1 - \frac{x}{2} - \frac{x^2}{8} - \frac{x^3}{16}\dots \tag{A.11}$$

One find the series for k_m

$$
\begin{aligned}
x &= a_m\xi + \frac{b^4}{192}\xi^2 + \frac{b^6}{4608}\xi^3\dots \\
x^2 &= a_m^2\xi^2 + \frac{a_m b^4}{96}\xi^3\dots \\
x^3 &= a_m^3\xi^3\dots \\
k_m &= k_{res}\left(1 - \frac{a_m}{2}\xi - \left(\frac{a_m^2}{8} + \frac{b^4}{384}\right)\xi^2 - \left(\frac{a_m^3}{16} + \frac{a_m b^4}{768} + \frac{b^6}{9216}\right)\xi^3\dots\right)
\end{aligned}
\tag{A.12}
$$

The series for k_z is found by solving $k_z = \sqrt{k_m^2 - k_r^2}$ with

$$k_m^2 = k_{res}^2\left(1 - a_m\xi - \frac{b^4\xi^2}{192} - \frac{b^6\xi^3}{4608}\dots\right) \tag{A.13}$$

$$\Leftrightarrow k_m^2 - k_r^2 = k_{res}^2\left(1 - \left(a_m + \frac{1}{k_{res}^2}\right)\xi - \frac{b^4\xi^2}{192} - \frac{b^6\xi^3}{4608}\dots\right) \tag{A.14}$$

$$\tag{A.15}$$

With the abbreviation

$$a_r = a_m + \frac{1}{k_{res}^2} = \frac{b^2}{8} + \frac{b\delta}{2} \tag{A.16}$$

the expansion of k_z is found in analogy to k_m

$$k_z = k_{res}\left(1 - \frac{a_r}{2}\xi - \left(\frac{a_r^2}{8} + \frac{b^4}{384}\right)\xi^2 - \left(\frac{a_r^3}{16} + \frac{a_r b^4}{768} + \frac{b^6}{9216}\right)\xi^3\dots\right) \tag{A.17}$$

Series expansion of k_m vs k_z

With the knowledge from the last section it is now possible to calculate the Taylor series expansion of $k_m(k_z)$. To do so one has to know the derivatives of the function $k_m(k_z)$

$$\frac{\mathrm{d}k_m}{\mathrm{d}k_z} = \frac{\mathrm{d}k_m}{\mathrm{d}\xi}\frac{\mathrm{d}\xi}{\mathrm{d}k_z} = \frac{\frac{\mathrm{d}k_m}{\mathrm{d}\xi}}{\frac{\mathrm{d}k_z}{\mathrm{d}\xi}} \tag{A.18}$$

$$\frac{\mathrm{d}^2 k_m}{\mathrm{d}k_z^2} = \frac{\mathrm{d}}{\mathrm{d}\xi}\frac{\mathrm{d}k_m}{\mathrm{d}\xi}\frac{\mathrm{d}\xi}{\mathrm{d}k_z} = \frac{\frac{\mathrm{d}^2 k_m}{\mathrm{d}\xi^2}\frac{\mathrm{d}k_z}{\mathrm{d}\xi} - \frac{\mathrm{d}k_m}{\mathrm{d}\xi}\frac{\mathrm{d}^2 k_z}{\mathrm{d}\xi^2}}{(\frac{\mathrm{d}k_z}{\mathrm{d}\xi})^3} \tag{A.19}$$

$$\frac{\mathrm{d}^3 k_m}{\mathrm{d}k_z^3} = \frac{\frac{\mathrm{d}^3 k_m}{\mathrm{d}\xi^3}(\frac{\mathrm{d}k_z}{\mathrm{d}\xi})^2 + 3\frac{\mathrm{d}k_m}{\mathrm{d}\xi}(\frac{\mathrm{d}^2 k_z}{\mathrm{d}\xi^2})^2 - 3\frac{\mathrm{d}^2 k_m}{\mathrm{d}\xi^2}\frac{\mathrm{d}k_z}{\mathrm{d}\xi}\frac{\mathrm{d}^2 k_z}{\mathrm{d}\xi^2} - \frac{\mathrm{d}k_m}{\mathrm{d}\xi}\frac{\mathrm{d}k_z}{\mathrm{d}\xi}\frac{\mathrm{d}^3 k_z}{\mathrm{d}\xi^3}}{(\frac{\mathrm{d}k_z}{\mathrm{d}\xi})^5} \tag{A.20}$$

Inserting the coefficients calculated above

$$\frac{\mathrm{d}k_m}{\mathrm{d}k_z} = \frac{a_m}{a_r} \tag{A.21}$$

$$\frac{\mathrm{d}^2 k_m}{\mathrm{d}k_z^2} = \frac{8}{a_r^3 k_{res}}\left(\frac{a_m^2 a_r}{8} + \frac{b^4 a_r}{384} - \frac{a_m a_r^2}{8} - \frac{b^4 a_m}{384}\right)$$

$$
= \frac{b^4 - 48a_m a_r}{48a_r^3 k_{res}^3} \tag{A.22}
$$

$$
\frac{\mathrm{d}^3 k_m}{\mathrm{d}k_z^3} = \frac{32}{a_r^5 k_{res}^2} \left[\frac{a_r^2}{4} \left(\frac{3a_m^3}{8} + \frac{a_m b^4}{128} + \frac{b^6}{1536} \right) \right.
$$
$$
+ 3\frac{a_m}{2} \left(\frac{a_r^4}{16} + \frac{a_r^2 b^4}{384} + \frac{b^8}{36864} \right)
$$
$$
- 3\frac{a_r}{2} \left(\frac{a_m^2 a_r^2}{16} + \frac{a_m^2 b^4}{768} + \frac{a_r^2 b^4}{768} + \frac{b^8}{36864} \right)
$$
$$
\left. - \frac{a_m a_r}{4} \left(\frac{3a_r^3}{8} + \frac{a_r b^4}{128} + \frac{b^6}{1536} \right) \right]
$$
$$
= \frac{a_m a_r b^4 - 48 a_m^2 a_r^2}{16 a_r^5 k_{res}^4} - \frac{48 a_r^2 b^4 - 4 a_r b^6 - b^8}{768 a_r^5 k_{res}^4}. \tag{A.23}
$$

The Taylor series then reads

$$
k_m = k_{res} + \frac{a_m}{a_r}(k_z - k_{res}) \tag{A.24}
$$
$$
+ \frac{b^4 - 48\, a_m a_r}{48\, a_r^3 k_{res}^2} \cdot \frac{(k_z - k_{res})^2}{2k_{res}}
$$
$$
+ \left(\frac{a_m a_r b^4 - 48 a_m^2 a_r^2}{16\, a_r^5 k_{res}^2} - \frac{48 a_r^2 b^4 - 4 a_r b^6 + b^8}{768\, a_r^5 k_{res}^2} \right) \frac{(k_z - k_{res})^3}{6k_{res}^2}
$$

Or in analogy (with a_r and a_m swapped)

$$
k_z = k_{res} + \frac{a_r}{a_m}(k - k_{res}) \tag{A.25}
$$
$$
- \frac{b^4 - 48\, a_m a_r}{48\, a_m^3 k_{res}^2} \cdot \frac{(k - k_{res})^2}{2k_{res}}
$$
$$
- \left(\frac{a_m a_r b^4 - 48 a_m^2 a_r^2}{16\, a_m^5 k_{res}^2} - \frac{48 a_m^2 b^4 - 4 a_m b^6 + b^8}{768\, a_m^5 k_{res}^2} \right) \frac{(k - k_{res})^3}{6k_{res}^2}
$$

Bibliography

[1] A. V. AGAFONOV, A. N. LEBEDEV, *Effects of Channel Roughness on Beam Energy Spread*, Physics of, and Science with, the X-Ray Free-Electron-Laser, AIP Proceedings, (2001). 13

[2] M. ANGELICI, F. FREZZA, A. MOSTACCI, L. PALUMBO, *Wake Fields Effects due to Surface Roughness in a Circular Pipe*, Physics of, and Science with, the X-Ray Free-Electron-Laser, AIP Proceedings, (2001). 13, 44

[3] V. AYVAZYAN ET AL., *Generation of GW Radiation Pulses from a VUV Free-Electron Laser Operating in the Femtosecond Regime*, Phys. Rev. Lett., 88 (2002). 21

[4] K. L. F. BANE, C. K. NG, A. W. CHAO, *Estimate of the Impedance due to Wall Surface Roughness*, Tech. Rep. SLAC-PUB-7514, SLAC, 1997. 13

[5] K. L. F. BANE, A. NOVOKHATSKI, *The Resonator Impedance Model of Surface Roughness Applied to LCLS Parameters*, Tech. Rep. SLAC-AP-117, SLAC, 2000. 13

[6] K. L. F. BANE, G. V. STUPAKOV, *Wake of a rough beam wall surface*, Tech. Rep. SLAC-PUB-8023, SLAC, 1998. 13

[7] K. L. F. BANE, G. V. STUPAKOV, *Impedance of a Beam Tube with small Corrugations*, Tech. Rep. SLAC-PUB-8599, SLAC, 2000. 13

[8] I. N. BRONSTEIN, K. A. SEMENDJAJEW, *Taschenbuch der Mathematik*, B. G. Teubner Verlagsgesellschaft, Stuttgart, Leipzig, 25 ed., 1991. 5, 19, 25

[9] J. CERNICHARO, *ATM: a program to compute atmospheric transmision between 0-1000 GHz*, tech. rep., Institut de Radioastronomie Millimétrique (IRAM), 1985. 43

[10] A. W. CHAO, *Physics of Collective Beam Instabilities in High Energy Accelerator*, New York, John Wiley & Sons,Inc., 1993. 38

[11] N. V. DENISOVA, *Maximum-entropy-based tomography for gas and plasma diagnostics*, Journal of Physics D, (1998). 24

[12] M. DOHLUS, *Impedance of Beam Pipes with Smooth shallow Corrugations*, Tech. Rep. DESY Print, TESLA 2001-26, DESY, 2001. 9, 10, 13, 44, 46

[13] M. DOHLUS, M. IVANYAN, V. TSAKANOV, *Surface Roughness Study for the TESLA-FEL*, DESY Print, (2000). 13

[14] B. R. FRIEDEN, *Restoring with maximum likelihood and maximum entropy*, J. Opt. Soc. Amer., (1972). 25

[15] M. GEITZ, *Investigation of the Transverse and Longitudinal Beam Parameters at the TESLA Test Facility Linac*, Tech. Rep. DESY-THESIS 1999-033, Deutsches Elektronen-Synchrotron, DESY, November 1999. 22, 35, 42

[16] U. HAHN, J. PFLUEGER, M. RUETER, P. D. HARTOG, M. ERDMANN, E. TRAKHTENBERG, G. WIEMERSLAGE, S. XU, *The Vacuum Chambers for the VUV SASE FEL at the TESLA Test Facility (TTF FEL) at DESY*, Proc. of PAC99, New York, (1999), pp. 1369–1371. 31, 46

[17] S. Hancock, M. Lindroos, *Longitudinal phase space tomography with space charge*, Phys. Rev. ST Accel. Beams, 3 (2000). 22

[18] K. Honkavaara, P. Piot, S. Schreiber, D. Sertore, *Bunch Length Measurements at the TESLA Test Facility using a Streak Camera*, Proc. of PAC2001, Chicago, (2001). 29

[19] M. Hüning, P. Piot, H. Schlarb, *Observation of Longitudinal Phase Space Fragmentation at the TESLA Test Facility Free-Electron Laser*, Nucl. Instr. Meth. A Vol. 475(1-3), pp 348-352, (2000). 36

[20] M. Hüning, P. Schmüser, H. Schlarb, M. Timm, *Measurements of Harmonic Wake Fields Excited by Rough Surfaces*, Phys. Rev. Lett. Vol 88 (2002), 074802, (2001). 39

[21] J. D. Jackson, *Classical Electrodynamics*, John Wiley & Sons, Inc., New York, 2 ed., 1975. 3

[22] E. T. Jaynes, *Prior Probabilities*, Trans. IEEE, SSC4, (1968). 25

[23] S. A. Kheifets, S. A. Heifets, *Radiation of a charge in a perfectly conducting cylindrical pipe with a jump in its cross section*, LINAC 86, Stanford, California, (1986). 13

[24] S. A. Kheifets, S. A. Heifets, *Radiation of a charge in a perfectly conducting cylindrical pipe with a jump in its cross section*, Tech. Rep. SLAC-PUB-3965, Stanford Linear Accelerator Center, 1986. 13

[25] K.-J. Kim, *Three-Dimensional Analysis of Coherent Amplification and Self-Amplified Spontaneous Emission in Free Electron Lasers*, Phys. Rev. Lett., 57 (1986). 16

[26] K.-J. Kim, Z. Huang, *Physics of High-Gain Free-Electron-Lasers*, US Particle Accelerator School, Stony Brook, (2000). 16, 17, 18, 19, 20

[27] E. D. Liberto, F. Frezza, L. Palumbo, *Effects of Statistical Roughness on the Propagation of Electromagnetic Fields in a Circular Waveguide*, Physics of, and Science with, the X-Ray Free-Electron-Laser, AIP Proceedings, (2001). 13

[28] D. Lis, *CSO Atmospheric Transmission Interactive Plotter*, Caltech Submillimeter Observatory (CSO), http://www.submm.caltech.edu/cso/weather/atplot.shtml, (2001). 43

[29] M. Hüning, H. Schlarb, M. Timm, *Experimental setup to measure the wake fields exited by a rough surface*, Nucl. Instr. Meth. A, 445 (2000), pp. 362–364. 38

[30] G. Minerbo, *MENT: A Maximum Entropy Algorithm for Reconstructing a Source from Projection Data*, Computer Graphics and Image Processing, (1979). 24

[31] F. Natterer, *Tomographie*, New York, John Wiley & Sons,Inc., 1993. 22

[32] A. Novokhatski, A. Mosnier, *Wakefields of Short Bunches in the Canal Covered with thin Dielectric Layer*, Proc. of PAC97 Vancover, Canada, (1997), pp. 1661–1663. 13

[33] A. Novokhatski, M. Timm, T. Weiland, *The Surface Roughness Wakefield Effect*, Tech. Rep. Proc. of ICAP 98 and DESY Print, TESLA 99-17, TU Darmstadt, September 1999. 9, 13

[34] A. Novokhatski, M. Timm, T. Weiland, H. Schlarb, *A Proposal for the Surface Roughness Wake Field Measurement at the Tesla Test Facility*, Proc. of PAC99, New York, (1999), pp. 2879–2881. 9, 13

[35] J. Pardo, E. Serabyn, J. Cernicharo, *Submillimeter atmospheric transmission measurements on Mauna Kea during extremely dry El Niño conditions: Implications for broadband opacity contributions*, Journal of Quantitative Spectroscopy & Radiative Transfer, 68 (2001), pp. 419–433. 43

[36] P. Piot. Private communication, DESY, 2002. 29

[37] P. Piot, S. Schreiber, D. Sertore, K. Floettmann, A. Cianchi, L. Catani, *Emittance Measurements at the TTF-Photoinjector*, Proc. of PAC2001, Chicago, (2001). 29

[38] S. Ratschow, T. Weiland, M. Timm, *On the Mechanism of Surface Roughness Wake Field Excitation*, Proc. of PAC2001, Chicago, (2001), pp. 167–169. 13

[39] S. Reiche, *Numerical Studies for a Single Pass High Gain Free-Electron Laser*, Tech. Rep. DESY thesis-00-012, Deutsches Electronen Synchrotron, 2000. 16, 17

[40] K. N. Ricci, T. I. Smith, *Longitudinal electron beam and free electron laser microbunch measurement using off-phase acceleration*, Phys. Rev. ST Accel. Beams, 3 (2000). 22

[41] E. Saldin, E. Schneidmiller, M. Yurkov, *The Physics of Free Electron Lasers*, Springer, New York, 1 ed., 1999. 16

[42] Y. Derbenev, J. Rossbach, E. Saldin, V. Shiltsev, *Microbunch Radiative Tail-Head Interaction*, Tech. Rep. TESLA-FEL 97-05, Deutsches Elektronen-Synchrotron, DESY, September 1995. 32

[43] H. Schlarb. Private communication, DESY, 2002. 30

[44] H. Schlarb, *Resistive Wall Wake Fields*, Tech. Rep. TESLA 97-22, Deutsches Elektronen-Synchrotron, DESY, November 1997. 21

[45] H. Schlarb, *Collimation System for the VUV Free-Electron Laser at the TESLA Test Facility*, Tech. Rep. DESY-THESIS-2001-055, Deutsches Elektronen-Synchrotron, DESY, November 2001. 29, 30, 31, 32, 37

[46] S. Schreiber, J.-P. Carneiro, K. Honkavaara, M. Hüning, J. Menzel, P. Piot, *Improved Parameters of the TTF Photoinjector for FEL Operation*, Proceedings of the EPAC 2002, Paris, (2002). 29, 32, 37

[47] G. V. Stupakov, *Impedance of small obstacles and rough surfaces*, Phys. Rev. ST Accel. Beams, 1 (1998). 13

[48] G. V. Stupakov, *Surface Impedance and Synchronous Modes*, Tech. Rep. SLAC-PUB-8208, SLAC, 1999. 10, 11, 13, 39

[49] G. V. Stupakov, *Surface Roughness Impedance*, Physics of, and Science with, the X-Ray Free-Electron-Laser, AIP Proceedings, (2001). 13

[50] G. V. Stupakov, R. E. Thomson, D. Walz, R. Carr, *Effects of Beam-Tube Roughness on X-Ray Free Electron Laser Performance*, Phys. Rev. ST Accel. Beams, 2(6) (1999). 13

[51] The TESLA Collaboration, *Technical Design Report*, Tech. Rep. TESLA 01-23, Deutsches Elektronen-Synchrotron, DESY, March 2001. 16, 21, 36

[52] M. B. Timm, *Wake Fields of Short Ultra-Relativistic Electron Bunches*, Der Andere Verlag, ISBN 3-935316-11-9, 2001. 9, 13, 39

[53] S. Turner, *CERN Accelerator School Synchrotron Radiation and Free Electron Lasers*, Tech. Rep. CERN 90-03, CERN, 1990. 16

[54] K. Wille, *Physik der Teilchenbeschleuniger und Synchrotronstrahlungsquellen*, Teubner, Stuttgart, 2 ed., 1996. 17

Acknowledgments